SEQUENTIALLY PLASMA ACTIVATED BONDING FOR WAFER SCALE NANO-INTEGRATION

SEQUENTIALLY PLASMA ACTIVATED BONDING FOR WAFER SCALE NANO-INTEGRATION

By

MD. GOLAM KIBRIA, B. Sc.

A Thesis

Submitted to the School of Graduate Studies

in Partial Fulfillment of the Requirements

for the Degree

Master of Applied Science

McMaster University

© Copyright by Md. Golam Kibria, August 2010

MASTER OF APPLIED SCIENCE (2010) McMaster University

(Electrical and Computer Engineering) Hamilton, Ontario

TITLE: Sequentially Plasma Activated Bonding for Wafer Scale Nano-Integration

AUTHOR: Md. Golam Kibria, B. Sc. (Electrical and Electronic Eng.)
(Khulna University of Eng. and Technology, Bangladesh)

SUPERVISOR: Professor Matiar Howlader

NUMBER OF PAGES: xiii, 121

ABSTRACT

Sequentially plasma activated bonding (SPAB) of silicon wafers has been investigated to facilitate chemical free, room temperature and spontaneous bonding required for integration of nanostructure on the wafer scale. The SPAB consists of surface activation using reactive ion etching (RIE) plasma followed by microwave (MW) radicals. The drop shape analysis and atomic force microscopy (AFM) results show that O_2 RIE plasma is the most efficient in removing surface contaminations while keeping smooth surfaces. On the other hand, MW N_2 radicals offer highly reactive, smooth and hydrophilic surfaces. These highly reactive, smooth and hydrophilic surfaces allow strong and spontaneous bonding of silicon/silicon at room temperature. Electrical characteristics show that the current transportation across the nano-bonded interface is dependent on plasma parameters. The infrared images show that plasma induced voids' nucleation at the bonded interface is dominated by O_2 RIE power over O_2 RIE activation time. The bonding strength achieved at room temperature in SPAB is about 30 times higher than that in hydrophilic bonding.

In order to explore the reliability of SPAB at high temperature, the bonded wafers are annealed from 200 to 900°C. The thermal induced voids' nucleation occurred preferentially at the plasma induced defect sites. The nucleation of void density is quantitatively determined and explained using high resolution transmission electron microscopy (HRTEM) observations. The electron energy loss spectroscopy results reveal the existence of silicon dioxide at the bonded interface. The reduction in bonding strength

after annealing at high temperature is correlated to the increase in void density. The plasma induced defect sites such as nanopores and craters are identified using an AFM. The porous surface allows easy removal of interfacial water and spontaneous covalent bonding at room temperature. The HRTEM results confirm nanometer scale bonding which is needed for the integration of nanostructures. Based on the results, a bonding mechanism of SPAB is presented.

In order to expand the applicability of SPAB for diverse materials, a novel hybrid plasma bonding (HPB) process is developed to achieve void-free and strong silicon/glass and germanium/glass bonding at low temperature. The HPB combines sequential plasma activation with anodic bonding process. Void-free interface with high bonding strength is observed both for silicon/glass and germanium/glass at 200°C. The bonding strength of the silicon/glass and germanium/glass in the HPB at 200°C is 30 MPa and 9.1 MPa, respectively. The improved characteristic behavior of the interface in the HPB is attributed to higher hydrophilicity and smooth surfaces of silicon, glass and germanium after sequential plasma activation and high electrostatic force associated with anodic bonding. Based on the results, a bonding mechanism of HPB is discussed.

The chemical free strong bonding of silicon/silicon in SPAB at room temperature and void-free strong bonding of silicon/glass and germanium/glass in HPB at low temperature can be applied in spontaneous integration of nanostructures on the wafer scale.

ACKNOWLEDGEMENTS

This thesis would not have been possible without the cooperation, encouragement and support of many people. First of all, I would like to express my sincere gratitude to my supervisor Prof. Matiar Howlader, who has introduced me to the field of Nanotechnology. His excellent supervision, utmost cooperation and incessant encouragement contributed greatly to this thesis.

I would like to extend my appreciation to Fangfang Zhang for her continuous assistance in the experiments and organizing the results. Without her help the experiments presented in this thesis would have been very difficult for me.

I am especially grateful to Wei Chen and Rogers of chemical engineering department for their assistance in drop shape analysis and tensile pulling test. I am indebted to Professor M. J. Kim, University of Texas, Dallas and his research group for their contribution to the high resolution transmission electron microscopy and electron energy loss spectroscopy at the early stage of this study. I would like to acknowledge Canadian Center for Electron Microscopy (CCEM) at McMaster University for high resolution transmission electron microscopy and energy dispersive X-Ray spectroscopy.

This research is supported by a discovery grant (#327947) from the Natural Science and Engineering Research Council (NSERC) of Canada and an infrastructure grant (#12128) from the Canada Foundation for Innovation (CFI).

At last but not the least, I would like to thank my parents and my siblings for their eternal love, patience, and continuous encouragements throughout my study in Canada.

TABLE OF CONTENTS

ABSTRACT iii

ACKNOWLEDGEMENTS v

TABLE OF CONTENTS vii

LIST OF FIGURES x

LIST OF TABLES xiv

CHAPTER 1. INTRODUCTION 1

1.1 Wafer Direct Bonding 1

1.1.1 Applications of Wafer Direct Bonding 2

1.1.2 Bonding Fundamentals 6

1.2 Wafer Direct Bonding Techniques 11

1.2.1 High Temperature Bonding 11

1.2.2 Moderate Temperature Bonding 13

1.2.3 Room Temperature Bonding: Sequentially Plasma Activated Bonding (SPAB) 15

1.3 Contributions 17

1.4 Objectives and Outline of the Thesis 17

CHAPTER 2. EXPERIMENTAL PROCEDURE 19

2.1 Introduction 19

2.2 Specimens 19

2.3 Bonding Equipment 20

2.4 Activation and Bonding Procedure 21

2.5 Surface Characterization Techniques 23

2.5.1 Drop Shape Analysis 23

2.5.2 Atomic Force Microscopy 25

2.6 Interface Characterization Techniques 27

2.6.1 Optical Transmission Method 27

2.6.2 Electrical Characterization 30
2.6.3 Tensile Pulling Test 31
2.6.4 High Resolution Transmission Electron Microscopy 32
2.6.5 Electron Energy Loss and Energy Dispersive X-Ray Spectroscopy 34

CHAPTER 3. SEQUENTIALLY PLASMA ACTIVATED BONDING OF SILICON/SILICON 36
3.1 Introduction 36
3.2 Surface Characterization of Silicon 37
3.2.1 Surface Hydrophilicity 37
3.2.2 Surface Roughness 46
3.3 Interface Characterization before Annealing 52
3.3.1 Interfacial Voids 52
3.3.2 Electrical Characterization 54
3.4 Interface Characterization after Annealing 58
3.4.1 Influence on Voids' Nucleation 58
3.4.2 Influence on Bonding Strength 65
3.4.3 Influence on Electrical Characteristics 67
3.4.4 Influence on Interface Morphology 69
3.5 SPAB Mechanism 73
3.6 Applications of SPAB for Nano-Integration 75
3.7 Conclusions 76

CHAPTER 4. SEQUENTIALLY PLASMA ACTIVATED BONDING OF SILICON/GLASS AND GERMANIUM/GLASS 78
4.1 Introduction 78
4.2 Hybrid Plasma Bonding (HPB) of Silicon/Glass 80
4.2.1 Surface Hydrophilicity 82
4.2.2 Surface Roughness 83

4.2.3 Role of Anodic Bonding Temperature on Interfacial Voids 85
4.2.4 Role of Plasma Activation on Interfacial Voids 87
4.2.5 Role of Plasma Activation on Bonding Strength 88
4.2.6 Nanointerface Observation 92
4.3 HPB of Germanium/Glass 93
4.3.1 Surface Hydrophilicity 93
4.3.2 Surface Roughness 94
4.3.3 Interfacial Voids and Bonding Strength 96
4.3.4 Nanointerface Observation 98
4.4 HPB Mechanism 100
4.6 Conclusions 103

CHAPTER 5. CONCLUSIONS AND FUTURE WORKS 105
5.1 Conclusions 105
5.2 Future Works 106

REFERENCES 108

LIST OF FIGURES

Figure 1.1: Schematic of a particle of height $2h$ leads to a void of radius R [13]............. 6

Figure 1.2: Schematic of gaps between wafers for the case of (a) $R > 2t_w$, (b) $R < 2t_w$, and (c) the regions of gap closing or not closing for two silicon wafers with various values of thickness t_w [1].. 9

Figure 1.3: Schematic of surface activation process (a) real surface, (b) surface activation, and (c) smooth and clean surface after activation.. 11

Figure 2.1: Schematic of sequentially plasma activated bonding (SPAB) equipment....20

Figure 2.2: Schematic of anodic bonding process. 22

Figure 2.3: Schematic of water droplet on Si wafer surface and the contact angle β......24

Figure 2.4: Schematic of tapping mode atomic force microscopy [43]......................... 25

Figure 2.5: Schematic of experimental setup for detecting interfacial voids in Si/Si bonded interface using optical transmission method.. 28

Figure 2.6: Schematic of experimental setup for current-voltage (*I-V*) measurements... 30

Figure 2.7: Schematic of tensile pulling test... 31

Figure 2.8: Schematic of TEM specimen preparation steps for Si/Si bonded wafers. The dimensions shown are in millimeters... 33

Figure 3.1: Contact angles of a droplet of DI water on Si wafer surface activated using different gases in RIE and MW condition..40

Figure 3.2: Contact angles of a droplet of DI water on Si wafer surface activated using different plasma conditions.. 43

Figure 3.3: AFM images of Si wafer surface after activation with (a) O_2 RIE, (b) N_2 RIE, and (c) Ar RIE plasma. 47

Figure 3.4: AFM images of Si wafer surface after activation with (a) MW O_2, and (b) MW N_2 radicals.. 47

Figure 3.5: Surface roughness of Si as a function of O_2 RIE plasma time and power in the SPAB.. 50

Figure 3.6: AFM images of Si surface (a) before, (b) after O_2 RIE activation with 300 W for 30 s (specimen C), (c) after O_2 RIE activation with 200 W for 30 s followed by MW N_2 radicals activation with 2500 W for 15 s (specimen B1), and (d) after O_2 RIE activation with 400 W for 30 s followed by MW N_2 radicals activation with 2500 W for 15 s (specimen B3).. 51

Figure 3.7: IR transmission images of Si/Si SPAB interfaces showing the influence of the O_2 RIE time (a) 15 s, (b) 30 s, (c) 60 s, and power (d) 200 W, (e) 300 W, and (f) 400 W on void formation.. 53

Figure 3.8: (a) Current-voltage characteristics, and (b) barrier height of the bonded *p*-Si/*p*-Si interface as a function of O_2 RIE plasma activation time.................................. 55

Figure 3.9: Schematic energy band diagram of a *p*-Si/*p*-Si bonded structure at (a) zero bias, and (b) with applied bias 56

Figure 3.10: IR transmission images of nonactivated reference Si/Si interfaces (a) before (at room temperature), and after sequential annealing at (b) 200, (c) 400, (d) 600, (e) 800, and (f) 900°C in nitrogen ambient for 4 hours in each step... 59

Figure 3.11: IR transmission images of O_2 RIE treated Si/Si interfacial voids for the specimen C (a) before (at room temperature), and after sequential annealing at (b) 200, (c) 400, (d) 600, (e) 800, and (f) 900°C in nitrogen ambient for 4 hours in each step........... 59

Figure 3.12: IR transmission images of SPAB treated Si/Si interfacial voids for the specimen B2 (a) before, and after sequential annealing at (b) 200, (c) 400, (d) 600, (e) 800, and (f) 900°C in nitrogen ambient for 4 hours in each step.................................... 60

Figure 3.13: IR transmission images of all the specimens in groups A and B for transitions of voids nucleation of the SPAB interfaces at (a) 15 s, (b) 30 s, and (c) 60 s in air, and (d) 200 W, (e) 300 W, and (f) 400 W (800°C) in nitrogen ambient for 4 hours at 600°C. 63

Figure 3.14: Void density in (a) SPAB specimen (B2) compared with that of in only RIE bonded specimen (C) annealed in nitrogen gas, (b) O_2 RIE time dependent specimens (A1, A2, A3) annealed in air, and (c) O_2 RIE power dependent specimens (B1, B2, B3) annealed in nitrogen gas for 4 hours at each annealing step... 64

Figure 3.15: Bonding strength as a function of annealing temperature for SPAB and hydrophilic bonding........66

Figure 3.16: (a) Current-voltage characteristics, and (b) barrier height of sequentially plasma activated *p*-Si/*p*-Si bonded interface at RT and after annealing at 200, 400, and 600°C for 4 hours in air. 68

Figure 3.17: High resolution TEM images of the bonded Si/Si interfaces (a) before annealing, and after annealing at (b) 200°C, (c) 400°C, and (d) 600°C. 71

Figure 3.18: (a) Scanning TEM image of the bonded Si/Si interface of specimen shown in Fig. 3.17 d, and (b) compositional distribution along the red line shown in (a) by the EELS analysis. 72

Figure 3.19: Schematic of SPAB mechanism. 74

Figure 4.1: Contact angle on Si and glass before and after plasma activation........84

Figure 4.2: AFM images of Si (a) before plasma activation, (b) after RIE activation (c) after sequential plasma activation, and of glass (d) before plasma activation, (e) after RIE activation, and (f) after sequential plasma activation. 85

Figure 4.3: Optical images of Si/glass wafers anodically bonded at temperature of (a) 100, (b) 150, and (c) 200°C. 87

Figure 4.4: Optical images of Si/glass wafers bonded through (a) (i) RIE plasma activated bonding, (ii) RIE plasma activated anodic bonding at 200°C, and (b) (i) SPAB, (ii) HPB at 200°C........ 89

Figure 4.5: Bonding strength as a function of different bonding conditions 90

Figure 4.6: Fracture images of Si/glass bonded using (a) the RIE plasma activated anodic bonding at 200°C, and (b) the HPB at 200°C.. 91

Figure 4.7: HRTEM images with (a) low, and (b) high magnifications. A ~353 nm thick bright depletion layer in the glass and an indistinct dark edge of Si near the interface are observed. 93

Figure 4.8: AFM images of Ge (a) before plasma activation, (b) after RIE plasma activation, and (c) after sequential plasma activation 96

Figure 4.9: (a) Optical image of hybrid plasma bonded Ge/glass, and (b) fracture image of bonded Ge/glass after tensile pulling test. 98
Figure 4.10: High resolution TEM image of hybrid plasma bonded Ge/glass interface. 99
Figure 4.11: EDX spectra of (a) Ge, (b) O, (c) Si, and (d) Na at and around the interface of hybrid plasma bonded Ge/glass. 100

LIST OF TABLES

Table 3.1: The average contact angles of a drop of DI water on Si wafer surface with different gases in RIE plasma condition. 38

Table 3.2: The average contact angles of a drop of DI water on Si wafer surface with different gases in MW plasma condition. 38

Table 3.3: The average contact angles of a drop of DI water on Si wafer surface with different surface treatment conditions. 42

Table 3.4: The average contact angles of a drop of DI water on Si wafer surface with different parameters of MW N_2 radicals 45

Table 3.5: The RMS surface roughness of Si wafer after activation with RIE plasma produced from different gases. 46

Table 3.6: The RMS surface roughness of Si wafer after activation with MW radicals produced from different gases.. 48

Table 3.7: The plasma parameters used for Si surface activation. 49

Table 4.1: The RMS surface roughnesses of Si and glass wafers 85

Table 4. 2: The contact angle of a drop of DI water on Ge wafer 95

Table 4. 3: The RMS surface roughness of Ge wafer 96

CHAPTER 1. INTRODUCTION

1.1 Wafer Direct Bonding

Wafer direct bonding refers to the process of joining clean and mirror-polished smooth surfaces without any adhesives or intermediate layers. The adhesion between the wafers is due to the short-range intermolecular and interatomic attractive forces, such as van der Waals forces and forces associated with hydrogen bonds [1]. Since, these bonds are not strong; often the bonded pair requires annealing at elevated temperature as high as fusion temperature of silicon wafer [2]. Therefore, wafer direct bonding is also known as "wafer bonding" or "wafer fusion bonding". In principle, all materials, regardless of their physical, structural or chemical properties, should be bonded once contacted as long as they satisfy surface requirements, i.e., surface roughness, flatness, and cleanliness. The typical range of the bonding energy is 10-100 mJ/m^2. Such low bonding energy transforms into strong bonding (typical bonding energy ~1000 mJ/m^2) depending on the surface and interface properties of mating wafer pair [2].

The wafer bonding phenomenon was first hypothetically explained by G. Galilei in17th century in the investigation of adhesion of solids with plane surfaces [3]. He explained that strong adherence would appear only between smooth surfaces due to vacuum across the interface, which would appear if one tries to separate them. In 1936, L. Rayleigh first demonstrated the adherence between glass slides through systematic investigation [4]. In 1969, Wallis and Pomerantz reported anodic bonding process for bonding metals or semiconductors with glass or other insulators which are conductive

(due to mobile ions i.e., Na^{+}) at temperatures used for bonding [5-6]. Since, the mobile ions are not compatible with microelectronic devices; the widespread application of anodic bonding process was restricted. The wafer bonding phenomenon has drawn little interest until mid-eighties when wafer bonding was first implemented as the substitute process for thick epitaxial layer growth of single crystalline silicon on silicon [7], and was applied for III-V compound semiconductors [8-9]. In 1986, IBM presented direct bonding of silicon wafers for the fabrication of silicon-on-insulator (SOI) substrate [10]. Since then, wafer bonding has found tremendous applications in the fabrication of SOI substrates for very large scale integration (VLSI), micro/nano-electro-mechanical systems (M/NEMS) [11] and III-V compound semiconductor based photonic and optoelectronic devices [12]. The applications of wafer bonding are briefly described in the following sections.

1.1.1 Applications of Wafer Direct Bonding

Wafer direct bonding offers the flexibility to bond diverse materials regardless of crystallinity, crystal orientation, lattice parameters, doping profile, doping type and wafer thickness [13]. This flexibility of wafer bonding has opened up opportunities for advanced micro/nano-electronics, low cost and high throughput packaging of M/NEMS and in photonics and optoelectronics as discussed in the following sections.

Wafer Direct Bonding in Advanced Micro/Nano-Electronics

The mainstream application of wafer direct bonding is in the fabrication of SOI substrate for advanced, high performance complementary metal oxide semiconductor (CMOS) based electronic devices [14]. The SOI substrate consists of a thin (>10 nm) silicon device layer on top of a dielectric silicon dioxide (SiO_2) layer (50 nm-1μm). The SiO_2 layer separates the active silicon device layer from the bulk mechanical support wafer which is typically silicon. The advantage of SOI substrate is that, transistors fabricated on SOI substrate have smaller parasitic capacitance and smaller source/drain leakage than transistors fabricated on bulk substrate [2]. Thus SOI substrate offers the fabrication of low-voltage, low-power and high-speed VLSI devices. Further, in case of SOI substrate, the buried SiO_2 layer isolates the top silicon device layer from the radiation damage in the bulk substrates (caused by high energy α-particles generated from radioactive packaging materials). Hence, advanced radiation-hard CMOS devices can be fabricated using SOI structures [15].

The speed, density and functionality of the CMOS devices can further be improved by bonding silicon device layer in a three dimensional (3D) fashion and connecting those using through-silicon-vias (TSVs) [16]. This 3D integration of silicon devices significantly reduces metal interconnection length and hence alleviates resistive-capacitive (RC) delay problem and excessive power consumption problem in the metal interconnects. Therefore, wafer bonding allows fabrication of high performance (i.e., high speed, low power consumption, small form factor) 3D integrated circuits (IC) for future semiconductor industry.

Wafer Direct Bonding in M/NEMS Packaging

Packaging refers to the process of device encapsulation and electrical interconnection. Packaging cost of M/NEMS contributes up to 90% of the total device cost [17]. Wafer direct bonding offers a cost-effective solution for M/NEMS packaging, which is indispensable for practical device fabrication. The M/NEMS often contain delicate structures, moving parts, sensitive surfaces (in case of sensors), which need to be protected from outside world. Often M/NEMS devices require vacuum sealed cavities for proper operation. Further, typical packaging and assembly tools such as dicing, soldering etc. are not usually compatible with delicate micro/nano-structures [17]. To protect M/NEMS, a lid wafer is directly bonded with the wafer that contains M/NEMS [18]. This process which involves packaging wafers before dicing is called wafer level packaging (WLP) [17-18]. The WLP avoids packaging costs of defective devices and protects delicate structures. Thus WLP using wafer bonding allows fabrication of complex micro/nano-systems, such as smart sensors and actuators. Vacuum sealed micro/nano-cavities and 3D complex structures can easily be realized by wafer bonding [19].

Various bonding methods have been proposed for WLP, such as glass frit sealing, anodic bonding, eutectic bonding and thermo-compression bonding [18]. However, these bonding techniques require high temperature and external pressure to achieve reliable bonding. This high temperature bonding process is not desirable for temperature sensitive materials and delicate M/NEMS structures [17]. Therefore, a low temperature bonding technique is needed for practical applications.

Wafer Direct Bonding in Photonics and Optoelectronics

Wafer direct bonding has also found significant interest in photonics and optoelectronics because of its potential to bond dissimilar materials [20]. The III-V compound semiconductors are the dominant materials for photo-emission, photo-detection, optical amplification, and other photonic applications. The integration of III-V compound semiconductor with silicon brings the functionality of photonic and optoelectronic integrated circuits together. Usually, the III-V semiconductors are integrated with silicon through hetero-epitaxial growth [21]. However, hetero-epitaxial growth leads to large number of misfit and threading dislocations in the deposited film caused by lattice mismatch between film and substrate. Also high temperature (~700-900°C) epitaxial growth is not compatible with microelectronics. To circumvent these issues, low temperature wafer direct bonding is highly desirable [22]. Successful bonding of GaAs/Si, InP/Si, InP/GaP for lasers, detectors and waveguides have been reported [2-13]. Low-threshold, long wavelength GaAs vertical cavity surface emitting laser structure has been integrated on silicon using wafer bonding process [23].

Further, the SOI substrate has gained interest for photonic applications because of large difference in refractive index of silicon (n=3.45) and SiO_2 (n=1.46) layer. This large refractive index difference allows fabrication of waveguide for light wave confinement and transmission using pattered SOI structure [24]. Thus SOI waveguide can be used as optical interconnects between electronic devices. The optical interconnects can address the challenges of metal interconnects, such as RC delay, high power consumption and cross-talk due to interference between close metal lines.

1.1.2 Bonding Fundamentals

The wafer surface properties control the quality of the direct bonded interface. The pre-requisites for wafer direct bonding are the surface cleanliness, flatness and smoothness, and surface activation. The following sections discuss in detail on these surface pre-requisites for wafer direct bonding.

Cleanliness

The direct bonding of wafers poses stringent requirements on the surface cleanliness. For spontaneous direct bonding, the wafer surfaces have to be free from contaminations, such as particles, organic and ionic residues. The presence of particle on the wafer surface results in unbonded regions or voids across the interface. Figure 1.1 schematically shows a particle of radius h at the bonded interface results in an unbonded area of radius (R). Assuming the particle as uncompressible, the radius of the unbonded area can be determined from the theory of small elastic deflections of a thin plate as [13]:

$$R = [\frac{2}{3} \cdot \frac{E' t_w^3}{\gamma}]^{1/4} h^{1/2} \tag{1.1}$$

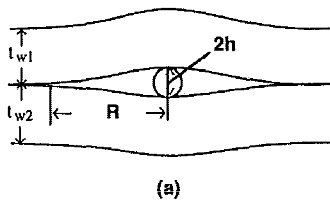

Figure 1.1: Schematic of a particle of height $2h$ leads to a void of radius R [13].

1.1.2 Bonding Fundamentals

The wafer surface properties control the quality of the direct bonded interface. The pre-requisites for wafer direct bonding are the surface cleanliness, flatness and smoothness, and surface activation. The following sections discuss in detail on these surface pre-requisites for wafer direct bonding.

Cleanliness

The direct bonding of wafers poses stringent requirements on the surface cleanliness. For spontaneous direct bonding, the wafer surfaces have to be free from contaminations, such as particles, organic and ionic residues. The presence of particle on the wafer surface results in unbonded regions or voids across the interface. Figure 1.1 schematically shows a particle of radius h at the bonded interface results in an unbonded area of radius (R). Assuming the particle as uncompressible, the radius of the unbonded area can be determined from the theory of small elastic deflections of a thin plate as [13]:

$$R = [\frac{2}{3} \cdot \frac{E' t_w^3}{\gamma}]^{1/4} h^{1/2} \qquad \text{.................................(1.1)}$$

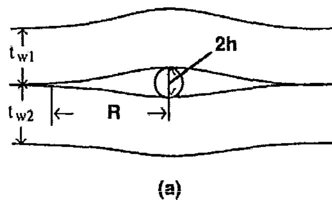

Figure 1.1: Schematic of a particle of height $2h$ leads to a void of radius R [13].

where, γ is the surface energy of each wafer, $E' = E/(1-\upsilon^2)$, E and ν are the Young's modulus and the Poisson ratio of the wafers, respectively. For (100) oriented silicon, ν=0.29, the equation 1.1 can be rewritten as,

$$R = \left[0.73E' \frac{t_w^3}{\gamma} \right]^{1/4} h^{1/2} \tag{1.2}$$

Equation 1.2 implies that a particle of about 1 μm diameter leads to an unbonded area with a diameter of 0.5 cm (5,000 times bigger than the particle diameter) for typical 4-in diameter 525 μm thick silicon wafers. Note that, the unbonded area is a strong function of wafer thickness. To alleviate this unbonded area caused by particulates, wafer bonding has to be performed in a clean room ambient.

Organic contamination results in weak bonding strength and nucleation of interfacial voids. Usually, particulates and organic contaminations can be removed by RCA (Radio Corporation of America) wet chemical cleaning process [13]. First, the wafers are rinsed in RCA1 solution (NH_4OH:H_2O_2:H_2O=1:1:5) followed by a deionized (DI) water rinse. Then the wafers are rinsed in RCA2 solution (HCL:H_2O_2:H_2O=1:1:5) followed by a DI water rinse. Finally, the wafers are blown dry with nitrogen gas. This cleaning process leads to the termination of the surface with silanol groups (Si-OH). This surface is easy to wet with water and hence termed as hydrophilic surface [13].

The metallic contaminations (e.g., metal ions from tweezers or containers) typically do not prevent initial wafer bonding or interfacial void formation. Hence, they do not play important role in many applications. However, metal ions can change the electronic properties of semiconductor devices [2].

Flatness and Smoothness

The flatness of a wafer is defined as the deviation of the surface from a flat reference plane [1]. It is usually expressed in terms of total thickness variation (TTV). The TTV can be determined by the difference between the highest and lowest point on the wafer surface. On the other hand, smoothness refers to the local microscopic topological variation. This is frequently expressed in terms of root mean square (RMS) roughness of the surface. Two sufficiently smooth wafer surfaces bond spontaneously at room temperature despite of a small flatness variation across the wafer. During bonding at room temperature, the wafers elastically deform to achieve conformity [1]. However, if the flatness variation is very high, the wafers do not bond.

The condition, under which a gap closes or remains open during wafer bonding, has been theoretically investigated in [13]. The condition depends on the ratio of lateral extension (R) to the wafer thickness t_w. In the mathematical description, two gap conditions have been considered with respect to the wafer thickness, as schematically shown in figure 1.2.

Case 1: $R > 2t_w$, the gap will close if

$$h < \frac{R^2}{\sqrt{\frac{2}{3} \cdot \frac{E' t_w^3}{\gamma}}}$$, which depends on wafer thickness

Case 2: $R < 2t_w$, the gap will close if

$$h < 3.5\left(\frac{R\gamma}{E'}\right)^{1/2}$$, which is independent on wafer thickness

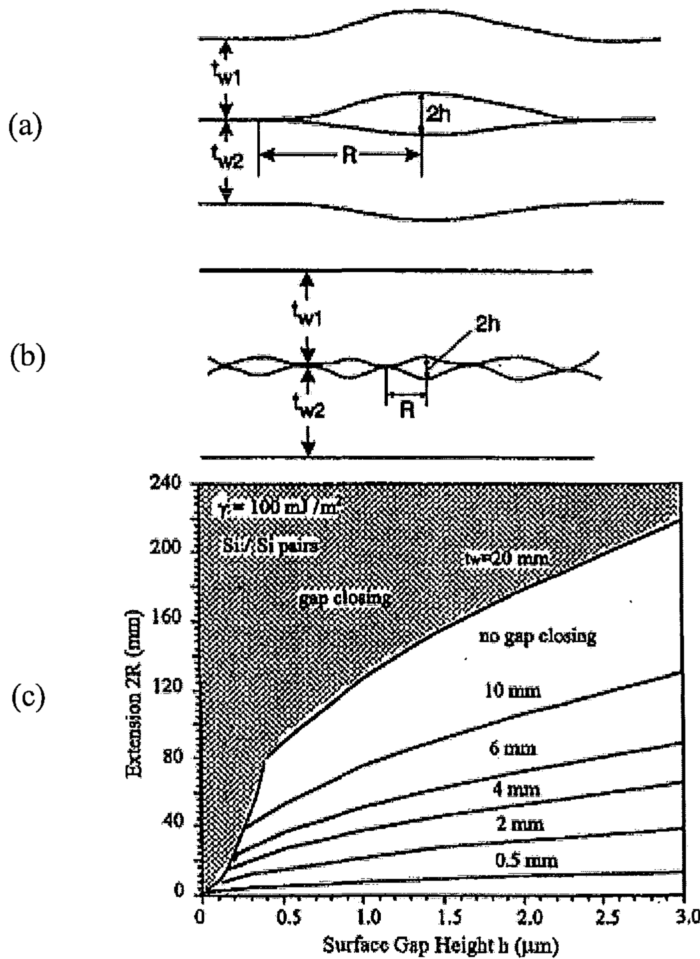

Figure 1.2: Schematic of gaps between wafers for the case of (a) $R > 2t_w$, (b) $R < 2t_w$, and (c) the regions of gap closing or not closing for two silicon wafers with various values of thickness t_w [1].

Figure 1.2 (c) shows the regions of gap closing or not closing for two silicon wafers of various thickness t_w. In practice, the commercially available 4-in silicon wafer has a flatness variation of 1-3 μm. Flatness variation in this order can be easily accommodated by mutual elastic deformation of the wafers [13]. In addition, wafer bow and warpage up to about 25 μm do not pose obstacles to wafer bonding (for 4 inch

wafers). On the other hand, experimental results show that two silicon surfaces with RMS roughness less than 0.5 nm can easily be bonded at room temperature via hydrogen bonds [13].

Surface Activation

One of the innovative techniques to improve the surface adhesion through cleaning the surface while maintaining its flatness and smoothness is the surface activation. Surface activation refers to a chemical and/or plasma cleaning process of the wafer surfaces to remove native oxides and contaminations. This process allows achieving maximum bonding energy [2]. The surfaces covered with native oxides are usually cleaned with HNO_3/HF solutions prior to bonding. The wafer surfaces can also be cleaned with plasma bombardment process. The wafers to be bonded are usually placed in a low vacuum plasma activation chamber. The plasma consists of charged and neutral particles. The charged particles are typically ionized atoms or molecules and electrons. The wafers are generally placed on a cathode so that the charged particles can bombard on the wafer surface resulting in sputtering. This physical sputtering process removes surface contaminations, native oxides and breaks Si-O and Si-H bonds (in case of silicon) on the surface. This results in a large number of dangling bonds (free bonds) on the plasma treated wafer surface. This increase in dangling bond results in an increase in surface energy and hence increase adhesion and bonding strength [25]. Figure 1.3 shows the schematic of (a) real surface, (b) surface activation process and (c) activated surface.

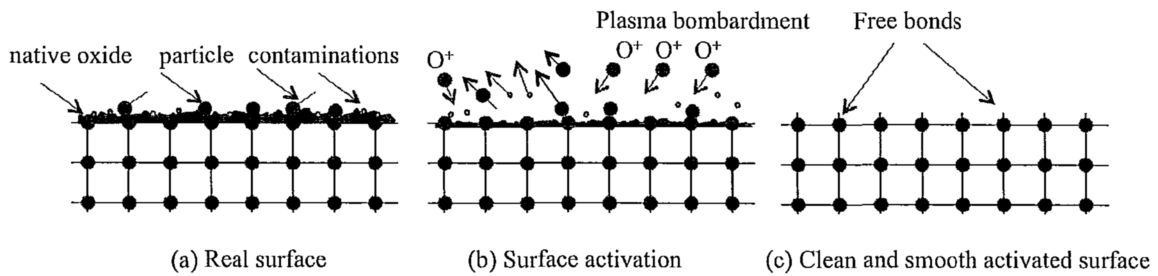

Figure 1.3: Schematic of surface activation process (a) real surface, (b) surface activation and (c) smooth and clean surface after activation.

Ensuring the aforementioned surface pre-requisites offers low bonding strength (~100 mJ/m^2) at room temperature. In order to ensure strong covalent bonding (~2-2.5 J/m^2) between the wafers, high temperature annealing is required in most of the prevalent bonding techniques. The common wafer direct bonding techniques are described in the following sections.

1.2 Wafer Direct Bonding Techniques

1.2.1 High Temperature Bonding

Hydrophilic Wafer Bonding

Currently, hydrophilic wafer bonding is the most common wafer direct bonding technique. The commercially available wafers are often covered with organic (i.e., carbon) and inorganic (alkali and heavy metal) contaminations and ~1-2 nm native oxide [13]. The organic and inorganic contaminations can be removed by rinsing wafers in RCA1 and RCA2 solutions, respectively. This leads to the formation of chemical oxide on the native oxide covered wafer surface. The chemically induced oxide consists of

covalently bond hydrogen and hence reacts instantaneously with water to form silanol groups (Si-OH). This surface is easy to wet with water and hence called hydrophilic. In clean room ambient, this hydrophilic surface is covered with a few monolayers of wafer through hydrogen bonds. When two hydrophilic surfaces are brought into contact, they adhere each other through hydrogen bonds. The bonding energy at this point is very weak (~100 mJ/m^2). Subsequent high temperature (>1000°C) annealing steps result in strong Si-O-Si bonding as a result of reactions between silanol groups (Si-OH) across the interface as follows [14],

$$\text{Si-OH+HO-Si} \rightarrow \text{Si-O-Si+}H_2O \quad (1.3)$$

The water molecules react with silicon, forming hydrogen gas across the interface [14].

$$Si + 2H_2O \rightarrow SiO_2 + 2H_2 \quad (1.4)$$

It can be inferred from the above equation that in case of hydrophilic bonding a thin oxide layer (SiO_2 in case of silicon) as well as hydrogen molecules are present at the bonded interface. The reaction byproduct H_2 is mainly responsible for the nucleation of voids at the bonded interface. One of the main challenges in hydrophilic bonding is to reduce the post-bonding annealing temperature and to alleviate the interfacial voids. Since SiO_2 absorbs H_2, the interface voids can be alleviated if a thick SiO_2 layer is present at the interface [2].

Hydrophobic Wafer Bonding

The interfacial oxide layer present in hydrophilic bonding is not desirable for some electronic applications. The oxide layer can be removed by cleaning the surface

with hydrofluoric acid or ammonium fluoride. This type of chemical cleaning terminates the surface by covalently bonded hydrogen. This surface cannot be wetted with water and hence called hydrophobic. When two hydrogen terminated surfaces are brought into contact, they adhere through van der Waals force between the weak polar Si-H bonds. At this point, the bonding energy is only ~20-30 mJ/m^2. Subsequent high temperature (>700°C) annealing step results in covalent Si-Si bonds [2]. However, the post-bonding annealing results in nucleation of voids at the bonded interface because of hydrogen desorption. Due to the absence of interfacial oxide layer, it is quite challenging to alleviate the interfacial voids in the hydrophobic bonding.

In order to avoid the post-bonding annealing issues in the hydrophilic and hydrophobic bonding, plasma activated wafer bonding process has been reported, as discussed in the following sections.

1.2.2 Moderate Temperature Bonding

Plasma Activated Wafer Bonding

In plasma activated wafer bonding (PAWB), the wafers surfaces are activated by a short duration plasma prior to contacting. The PAWB has found tremendous interest in the last decade due to its potential in direct bonding at moderate temperature (~400°C) [25]. Although different chemical cleaning procedures have been proposed for moderate temperature bonding, their effectiveness is not as good as plasma activation. The PAWB offers high bonding strength at temperatures in the range of 400~500°C. The most common plasma gases used for surface activation are oxygen, nitrogen or argon [26].

Among these, oxygen plasma is known to be most effective in increasing the surface energy [27]. During the short plasma treatment, a number of physical and chemical processes take place simultaneously. It has been proposed that the physical sputtering process of the plasma results in nanoscopic surface porosity in the silicon oxide (in case of silicon wafer) [28]. This allows absorbing reaction byproducts (mainly H_2 and H_2O) more easily compared to processes which do not involve plasma activation. Further, plasma activation has been found to create highly hydrophilic surface, and the hydrophilicity has been found to last for several days [29]. Furthermore, the influence of plasma on surface roughness has been reported by many research groups. The results are controversial since some reports showed smoothening [30-31] and some reports demonstrated roughening [25] of the surface after plasma activation. Farrens *et al* [29] have reported that plasma activation induces 1-1.5 nm oxide layer on the silicon wafer. They believed that the oxide layer contains free radicals, which enhances the bonding strength at moderate temperature.

The moderate annealing temperature required for PAWB is not desirable for temperature sensitive and delicate devices. Amirfeiz *et al* [28, 32] have reported room temperature direct bonding of silicon/silicon and silicon/quartz by oxygen plasma activation followed by dip in water. However, the water dip resulted in interfacial voids after storage for one month. Further, the residual waters on the wafer surface can affect the operation of surface sensitive micro sensors and actuators. Hence, a room temperature and wet chemical/water free bonding process is highly desirable to address the issues caused by annealing.

1.2.3 Room Temperature Bonding: Sequentially Plasma Activated Bonding

Most of the current wafer bonding techniques require high temperature annealing (~1000°C for Si/Si bonding, and ~600°C for III-V compound semiconductor bonding) to ensure the formation of strong bonding between wafers. This high temperature annealing is not compatible for many applications. Especially for dissimilar material bonding, the mismatch in thermal expansion coefficient of the mating wafers imposes severe restrictions on the post-bonding annealing temperature [13]. The mismatch in thermal expansion coefficient induces high thermal stress and causes crack at the bonded interface. The high temperature annealing steps after bonding can induce material degradation, modify doping profile, generate large threading, and misfit dislocations in heterogeneously bonded delicate structures that have different thermal expansion coefficients and a large lattice mismatch [33]. Further, high temperature annealing is not preferable especially for pre-processed wafers which contain temperature-sensitive materials (i.e., copper or aluminum interconnect layers). Annealing over 450°C can cause severe damage to aluminum patterns. Further, high temperature annealing usually leads to the nucleation of voids at the bonded interface [2]. In order to address all of the above issues, a room temperature bonding process, called sequential plasma activated wafer bonding (SPAB) has been developed recently [34].

The SPAB has attracted much attention due to its ability to achieve strong bonding at room temperature [34]. The SPAB consists of two steps: (1) surface activation

by reactive ion etching (RIE) plasma, followed by (2) surface activation by microwave (MW) neutral radicals and then contacted the activated wafers in air [35]. The surface activation in the first step removes contaminants, native oxides (i.e., SiO_2 in case of Si), and particles from the surfaces through physical sputtering process. The second step of surface activation can change the reactivity of the surface. The plasma activation makes the surface highly hydrophilic and results in spontaneous bonding at room temperature. The SPAB method does not require any wet chemicals, intermediate adhesives, external forces, UHV and post-bonding annealing steps to achieve high bonding strength even for the integration of dissimilar materials with large lattice mismatch [36]. The bonding strength achieved through SPAB without post-bonding annealing is equivalent to the bulk fracture strength of the mating wafers [37]. Silicon/silicon and glass/glass wafers have been successfully bonded at room temperature without annealing using SPAB for microfluidics packaging [36-37]. Despite of the potential for room temperature bonding, a little effort has been made to understand the SPAB process. To understand the SPAB process, it is indispensable to comprehend the influence of plasma parameters such as gas, power, time and pressure on the surface and bonded interface properties; which has not been investigated yet. Further, in some applications, the bonded wafer pair undergoes high temperature annealing steps. The high temperature annealing results in nucleation of voids at the bonded interface. Therefore, the influence of annealing on the nucleation of voids, bonding strength, electrical conductivity and interface morphology has to be investigated to understand the reliability of SPAB process for real applications. Since silicon is the most frequently used material in microelectronics and in M/NEMS industry;

understanding the bonding mechanism in SPAB for silicon wafers allows expanding the applicability of SPAB for other materials. Earlier [38], the SPAB was used for bonding of glass/glass wafers. However, the bonding strength was very low and required further investigation. Hence, the motivation of this thesis is to understand the SPAB process for silicon wafers and expand its applicability for diverse materials.

1.3 Contributions

From this study, I have contributed to four peer-reviewed journal articles. The first one was [48] on exploring the properties of Si/Si bonded interface in SPAB. The second one [49] was on the nucleation of voids at Si/Si bonded interface in SPAB. Third one [96] was on hybrid plasma bonding of void-free and strong Si/glass interface at 200°C. And the last one [97] was on hybrid plasma bonding of void-free and strong Ge/glass interface at 200°C. For all of these articles, I am primarily responsible for literature search and writing the manuscript. Specifically, I have primarily involved in the process development for spontaneous and hybrid bonding and surface characterization, along with partial contribution to the interface analysis.

1.4 Objectives and Outline of the Thesis

The objectives of this thesis are to comprehensively investigate the SPAB process of silicon wafers for nano-integration, and to modify the SPAB process for other materials (e.g., glass and germanium) for lab-on-a-chip and photodetector applications.

The surface of silicon and the interface of room temperature bonded silicon/silicon have been investigated to understand the role of plasma and post-bonding annealing steps. To expand the applicability of SPAB for glass wafers, a novel hybrid plasma bonding (HPB) technique has been developed, through combining the SPAB with anodic bonding process. The HPB technique has been successfully implemented for void-free strong bonding of silicon/glass and germanium/glass wafers at low temperature (200°C).

This thesis consists of five chapters. Chapter 1 presents the historical background, fundamentals, types and advance applications of wafer direct bonding. Chapter 1 concludes with the motivation and objectives of this study. Chapter 2 focuses on the basic principles and relevant experimental aspects of the surface and interface characterization techniques. Chapter 3 discusses the influence of plasma parameters on the surface properties of silicon in order to clarify the spontaneous bonding in the SPAB. Chapter 3 also discusses the influence of post-bonding annealing on the room temperature bonded silicon/silicon interface and the bonding mechanism in SPAB. Chapter 4 presents void-free strong bonding of silicon/glass and germanium/glass interfaces at low temperature using the modified SPAB (i.e., HPB) technique. Finally, in Chapter 5, conclusions have been drawn and future works have been proposed.

CHAPTER 2. EXPERIMENTAL PROCEDURE

2.1 Introduction

This chapter focuses on the basic principles and experimental aspects of the surface and interface characterization techniques. The wafer surface and bonded interface have been investigated using different characterization techniques. The surface characterization techniques include drop shape analysis and atomic force microscopy. The interface characterization techniques include optical transmission method, electrical characterization, tensile pulling test, high resolution transmission electron microscopy, electron energy loss spectroscopy and energy dispersive X-ray spectroscopy.

2.2 Specimens

In this study, silicon, germanium and glass wafers were used for bonding experiments. The silicon wafers were commercially available Czochralski (CZ) grown one-side polished 4-inch, 525±25 μm thick, *p*-type (B doped, 20-30 ohm~cm) and (100) oriented. The germanium wafers were commercially available CZ-grown one-side polished 2-inch 225±25 μm thick, *n*-type (Sb doped, 0.001~1 ohm-cm) and (100) oriented. The glass wafers were double side polished Pyrex 7740 borosilicate 4-inch and 500±25 μm thick. The major elements in the Pyrex glass were SiO_2 (80.93%) including B_2O_3 (12.7%), Na_2O (4.00%), Al_2O_3 (2.30%), K_2O (0.04%) and Fe_2O_3 (0.03%).

2.3 Bonding Equipment

The surface activation and wafer bonding was accomplished using a wafer level plasma activated bonding equipment as shown schematically in figure 2.1. The bonding equipment accommodates up to 200 mm diameter wafer. It consists of sequential plasma activation and anodic bonding chambers. The sequential plasma activation chamber consists of bottom and top compartments to generate reactive ion etching (RIE) and microwave (MW) plasma, respectively. The RIE plasma was generated from oxygen (O_2) or nitrogen (N_2) or argon (Ar) gases at 13.56 MHz. The MW plasma was generated from O_2 or N_2 gasses at 2.45 GHz. The bottom and top compartments are separated by an ion trapping metallic plate, which is grounded.

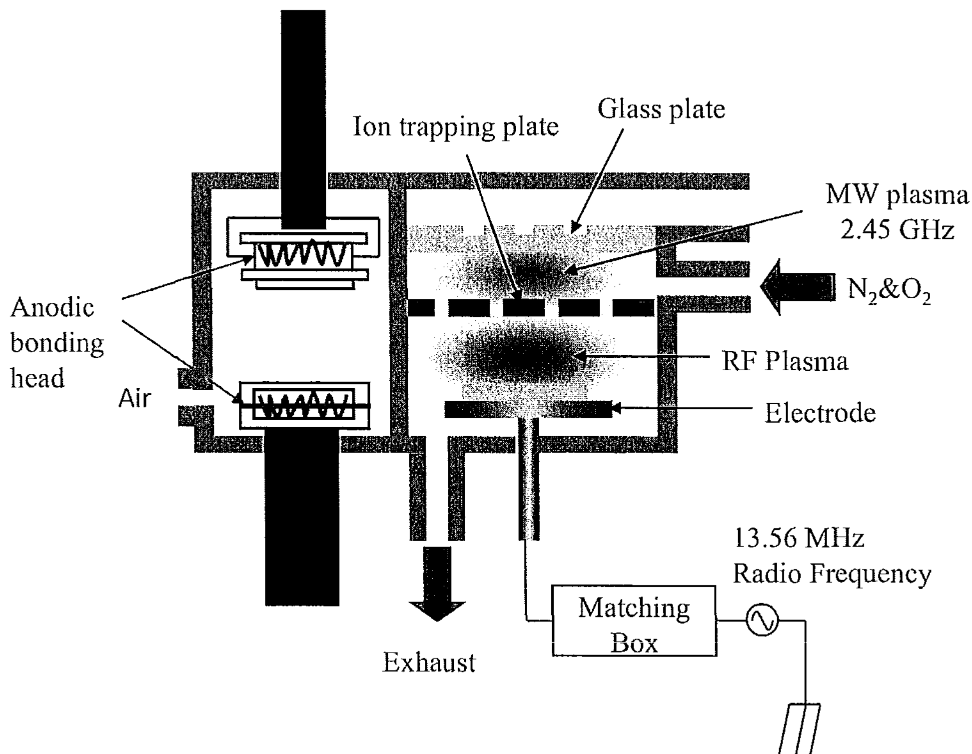

Figure 2.1: Schematic of sequentially plasma activated bonding (SPAB) equipment.

The wafers to be activated were placed on the radio frequency (RF) driven electrode. The RIE plasma was generated by the discharge between the RF electrode and the ion trapping metallic plate. The MW plasma was guided by a metal rectangular waveguide and coupled with a dielectric circular glass (quartz). The MW plasma was thus radiated inside the top compartment resulting in electrical discharges of N_2 or O_2 gas [39]. The ion trapping metallic plate has holes of diameter 1 mm, which traps charged ions and thus helps producing neutral radicals at the bottom compartment. The positive ions in the RIE plasma are accelerated by direct current (DC) self-bias voltage and thus remove contaminations, native oxides from the surface by physical sputtering mechanism, whereas the MW neutral radicals create chemically reactive wafer surfaces.

The anodic bonding chamber is equipped with high voltage electrodes, and heaters in bonding heads to anodically bond the wafers at temperatures up to 200°C. The DC applied voltage and time in the anodic bonding were kept constant at 1 KV and 10 min, respectively regardless of the temperature. The details of anodic bonding process are discussed in chapter 4.

2.4 Activation and Bonding Procedure

The wafers were first placed in sequential plasma activation chamber. As mentioned previously, the sequential plasma activation consists of surface activation using RIE plasma followed by activation using MW radicals. The activation time, power and chamber pressure for RIE plasma

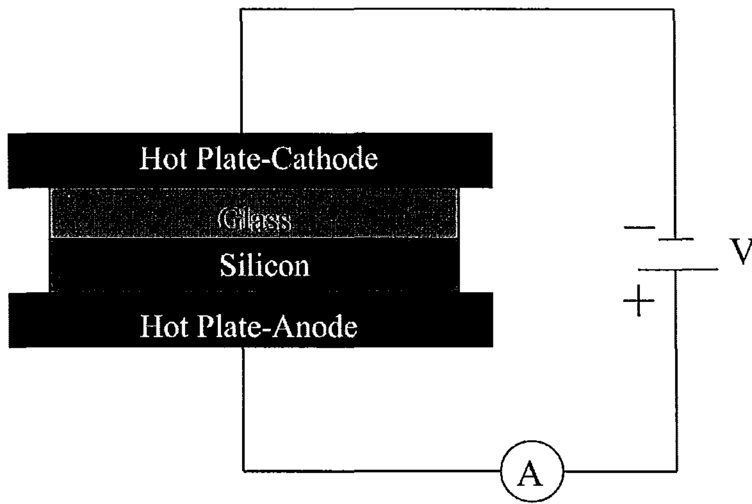

Figure 2.2: Schematic of anodic bonding process.

were varied from 5-300 s, 50-400 W and 40-120 Pa, respectively. The activation time, power and chamber pressure for MW radicals were varied from 15-120 s, 1500-2500 W and 50-150 Pa, respectively. The plasma parameters were chosen based on the previous study [40]. With these plasma parameters, the self-bias voltage at the substrate electrode varied between -35 V and -185 V. After sequential plasma activation, the wafers were taken out of the chamber and bonded in clean room (10,000 class) ambient using hand applied pressure. Finally, the wafers were cold-rolled with 0.2 MPa load to remove the trapped air from the interface.

For anodic bonding of silicon/glass, the wafers were contacted in clean room ambient and then placed in the anodic bonding chamber. The silicon wafer was placed on the anode hot plate (bottom plate) and the glass wafer was placed on the cathode hot plate (top plate). Two heaters are embedded in the anodic bonding head as shown in figure 2.1.

Figure 2.2 shows a schematic of anodic bonding process. The wafer pair was first heated by the heater attached in the bonding head at temperatures 100-200°C for 10 min under an external force of 0.07 MPa using the upper bonding head. Then the heater was turned off and a 1 KV bias was applied in the anode and cathode. The applied bias was kept constant until the anodic current flow ceased.

2.5 Surface Characterization Techniques

The surface characteristics of the wafers (e.g., hydrophilicity and surface roughness) determine the bonding quality (e.g., bonding strength, interfacial voids) of the wafers. The following sections describe the wafer surface characterization techniques that have been performed in this study.

2.5.1 Drop Shape Analysis

As discussed in chapter one, the wafer surface has to be hydrophilic to achieve strong bonding at low bonding temperature. Hence, the study of wafer surface hydrophilicity prior to bonding allows finding the optimum plasma parameters required for strong bonding.

A straightforward way to study surface hydrophilicity is to measure the contact angle of a drop of water on the surface. This can be done by a drop shape analyzer. The lower the contact angle, the higher the degree of hydrophilicity resulting in better wettability of the surface [41]. This is critical for this study since the higher the surface hydrophilicity, the easier it is to bond between the surfaces [42]. Figure 2.3 shows the

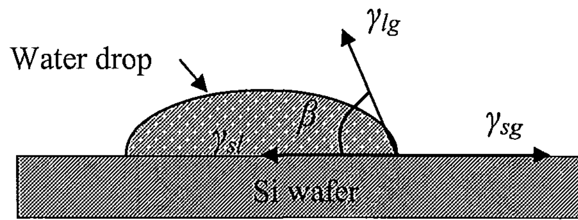

Figure 2.3: Schematic of water droplet on Si wafer surface and the contact angle β.

contact angle (β) of a drop of DI water on silicon wafer surface. Contact angle is related to the surface energy of the solid and the surface tension of the liquid by Young equation [42], as follows,

$$\gamma_{sg} - \gamma_{sl} - \gamma_{lg} \cos \beta = 0 \tag{2.1}$$

The liquid-gas interface energy γ_{lg} (i.e. surface tension) and the solid-liquid interface energy γ_{sl} depend on the liquid being used. The solid-gas interface energy γ_{sg}, also called solid surface energy, increases with a decrease in contact angle. For hydrophilic surfaces, the contact angle usually remains much less than 45°, and it is usually higher than 45° for hydrophobic surfaces [14]. Hence, a hydrophilic surface is easier to bond than a hydrophobic surface.

The contact angle was measured using the sessile drop method with a DI water droplet. Drop Shape Analysis system (DSA100) from Kruss was used to measure the contact angle. A contact angle below 2° cannot be detected using the equipment.

2.5.2 Atomic Force Microscopy

Atomic force microscopy (AFM) is the most versatile technique to determine the surface morphology in sub-nanometer scale resolution. Hence, this is very useful in determining the surface roughness. Also, AFM allows locating the plasma induced surface defect. For surface roughness measurement, an AFM from Veeco (ICON) was used. Silicon tip in tapping mode was utilized over a scanning area of 2×2 μm^2or 5×5 μm^2 or 10×10 μm^2.

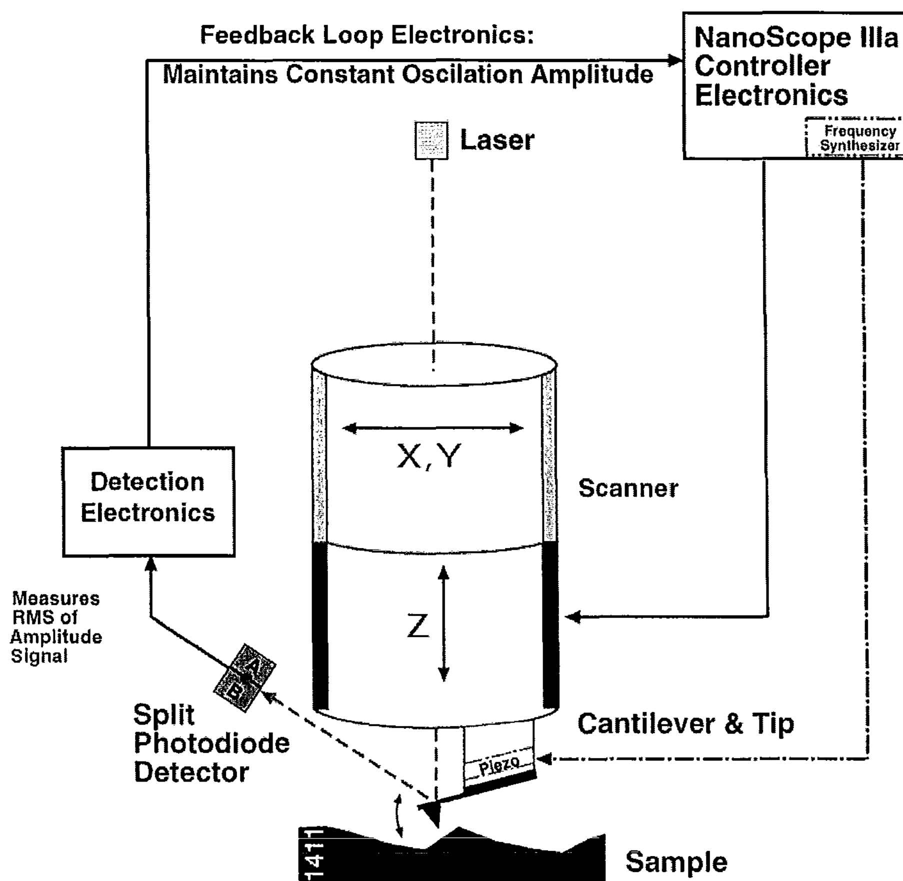

Figure 2.4: Schematic of tapping mode atomic force microscopy [43].

The AFM operates by raster scanning a sharp tip attached to the end of a cantilever across the specimen. The two commonly used operating modes of AFM are contact mode and tapping mode. In contact mode AFM, the tip touches and raster scans across the specimen surface. Although contact mode AFM offers high scan speeds (throughput), the lateral forces (shear) and high normal forces (due to capillary forces from the adsorbed fluid layer on the specimen surface) can destroy surface features due to scraping between the tip and specimen [43]. In order to avoid the surface damage from the lateral forces, tapping mode AFM was adopted in this study. Figure 2.4 shows a schematic of tapping mode AFM. The cantilever is derived to oscillate at or slightly lower than its resonant frequency. The tip attached to the end of the cantilever taps on the specimen surface during raster scanning with amplitude ranging typically from 20 nm to 100 nm [43]. The laser light is reflected from the back surface of the cantilever and is detected by the split photodiode detector. The feedback loop maintains a constant tip-sample interaction by maintaining constant oscillation amplitude. To maintain a constant amplitude, the vertical position of the scanner at each (x, y) data point changes and is stored by the computer to form the topographic image of the specimen surface. The scanner is made of piezoelectric material, which expands or contracts proportionally to an applied voltage. The scanner is capable of sub-angstrom resolution in x-, y- and z-directions and thus provides a three dimensional image of the surface topography of the specimen.

2.6 Interface Characterization Techniques

The interface characterization allows understanding the bonded interface properties such as interfacial voids, electrical conductivity, bonding strength, interfacial layers and composition. The following sections describe the interface characterization techniques that have been performed in this study.

2.6.1 Optical Transmission Method

Observation of Interfacial Voids

If one of the bonded wafers is transparent to visible light, such as glass, quartz, lithium niobate ($LiNbO_3$), gallium nitride (GaN) etc., the interfacial voids can be observed with naked eye. However, if both of the bonded wafers are not transparent to the visible light, then appropriate light source and detector is required to detect the interfacial voids. The most commonly used technique to detect interface voids is optical transmission method. This method is inexpensive, real time, convenient and nondestructive. If the energy (hv) of the incident photon is equal or higher than the band gap energy (E_g) of the material under irradiation, the incident photon breaks the covalent bonds in the lattice. This process generates electron-hole pairs and thus absorbs the incident light [13]. Hence, in order to pass light through the material, the incident photon energy has to be less than the band gap energy [13],

$$h\nu < E_g \tag{2.2}$$

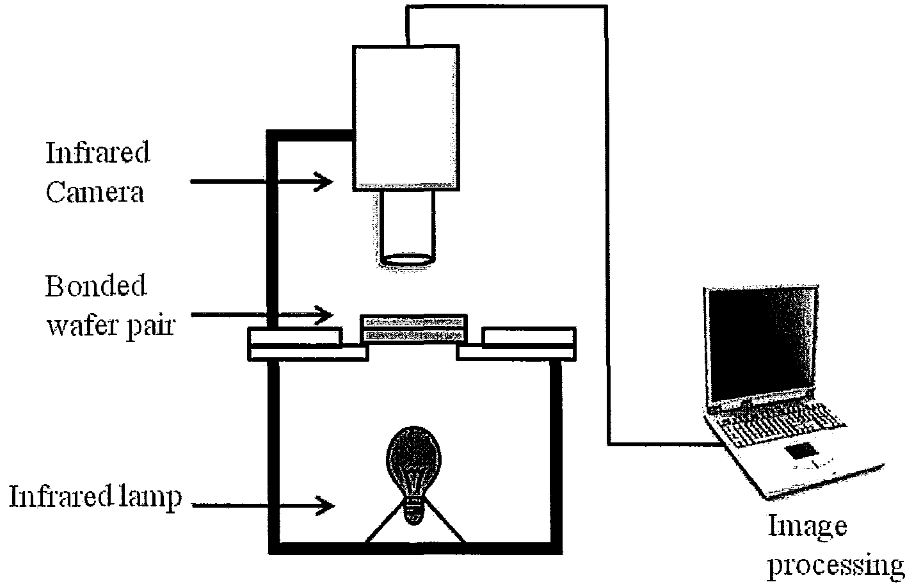

Figure 2.5: Schematic of experimental setup for detecting interfacial voids in Si/Si bonded interface using optical transmission method.

$$\text{i.e., } h\frac{c}{\lambda} < E_g \text{, where } c = \lambda\nu$$

$$\text{or, } \lambda > \frac{hc}{E_g} \tag{2.3}$$

here, c is the speed of light (2.998×10^{8} m/s in vacuum) and h is the Planck constant (6.62617×10^{-34} J-s and ν is the frequency of light). Silicon has band gap energy of 1.12 eV at room temperature. Therefore, from equation 2.3, the minimum wavelength of light that can pass through silicon is 1.10 μm. This wavelength falls in infrared (IR) region of the electromagnetic spectrum. Hence, an IR light source and IR sensitive camera are required for detecting interfacial voids in bonded silicon/silicon pairs. Figure 2.5 shows the experimental setup for detecting interfacial voids. When different materials are

bonded, the smaller band gap among the two bonding material must be used to calculate the minimum wavelength from equation 2.3.

Further, the absorption of light in the material can be described by the following equation [13]

$$I(x) = I_0 \exp(-\alpha x) \quad (2.4)$$

where, I_0 is the incident light intensity, x is the distance travelled by light in the material perpendicular to the surface, and α is the absorption coefficient. The absorption co-efficient is a function of free carrier concentration (n) and the wavelength of light according to the following equation [13]:

$$\alpha \propto n\lambda^2 \quad (2.5)$$

Therefore, if one of the bonded silicon wafers is heavily doped, strong free carrier absorption occurs even for $\lambda > \lambda_{min}$. Hence, the optical transmission method does not work for heavily doped semiconductors and for metals.

At the unbonded region (voids), due to partial transmission and reflection of light from the air-silicon interface, distinct Newton rings (interference fringes) result. Assuming the content in the void as air with refractive index 1.0, the height H of the voids can be estimated by counting the number of fringes N, as follows [13],

$$H = N\frac{\lambda}{2} \quad (2.6)$$

The optical transmission method allows detecting voids down to half of a fringe. Hence, the minimum detectable void height is □4. The minimum detectable lateral size

of the voids depends on the resolution of the IR camera. Usually, voids with diameter greater than 1 mm can be detected through this method.

2.6.2 Electrical Characterization

The electrical characteristics of the bonded interface was investigated using current-voltage (*I-V*) measurements. The *I-V* characteristic explores the presence of barrier layers, plasma induced charges, defects and state densities at the bonded interface. Hence, the *I-V* characteristics as a function of plasma parameters can be used to identify

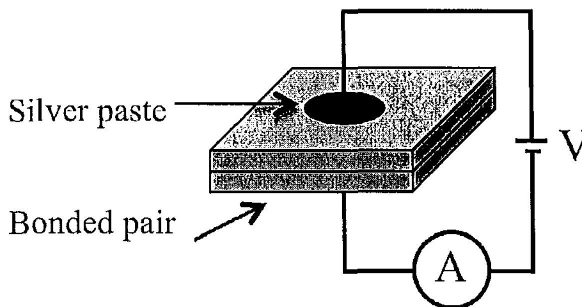

Figure 2.6: Schematic of experimental setup for current-voltage (*I-V*) measurement.

the desired current transport properties of the bonded interface. The *I-V* characteristic of the bonded pair was investigated after dicing the bonded wafer pair into 10×10 mm^2 pieces. Highly conductive silver paste (typical resistivity ~ 3×10^{-5} ohm-cm) was used to make contact electrodes with the wafer surface as shown in figure 2.6. Metal electrodes were not chosen because of the possibility of sintering the electrode metal and silicon at high temperature metal deposition and annealing steps [44]. The HP-4145B semiconductor parameter analyzer was used for *I-V* characterization.

2.6.3 Tensile Pulling Test

There are different ways to characterize the mechanical properties of the interface of the bonded wafers. Tensile pulling test is one of the most common techniques to determine the tensile strength of the bonded interface. In this study, tensile pulling test was performed using a tensile pulling tester from Instron, to determine the bonding strength of the interface. For tensile pulling test, the bonded specimens were diced into 10×10 mm^2 and glued using high strength

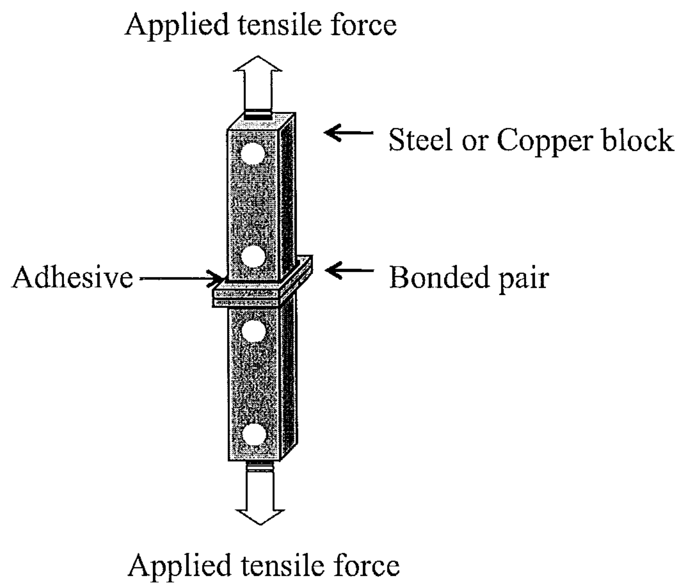

Figure 2.7: Schematic of tensile pulling test.

adhesives with steel or copper blocks as shown in figure 2.7. The size of the specimen was larger than the steel or copper blocks to prevent the adhesive from spreading to the side faces on the bonded pair. The steel or copper block (attached to the tensile pulling tester) pulls the bonded pair apart from two opposite directions perpendicular to the bonded surfaces to separate the wafers. The bonding strength is given by the force at

separation divided by the area of the specimen. The maximum bonding strength that can be measured by this technique is limited by the tensile strength of the adhesive. To avoid this issue, high strength adhesive (tensile strength of adhesive was higher than that of the bonded interface) was used in this study.

2.6.4 High Resolution Transmission Electron Microscopy

While AFM can resolve sub-nanometer scale surface morphology, high resolution transmission electron microscopy (HRTEM) is capable to image nanometer scale bonded interface morphology. Since the activation sources, i.e., RIE and MW, have physical sputtering and chemical reactivity with the surfaces, the interface characterization using HRTEM allows revealing the influence of the activation sources. The deviation of the crystallinity of wafers indicates amorphous interfacial layers. In this study, HRTEM was performed to investigate on the thickness and morphology of interfacial layers, the presence of interface defects and voids.

The transmission electron microscopy uses electrons and a series of electromagnetic lenses to magnify the specimen. For HRTEM characterization, the specimen has to be thin enough (thickness between ~10-50 nm) to be electron transparent. The transmitted and forward scattered electrons form a diffraction pattern in the back focal plane and a magnified image of the specimen on the image plane, respectively [45].

For HRTEM, the preparation of very thin specimen is quite challenging and involves a number of steps. Figure 2.8 shows the steps followed to make the HRTEM specimens. First, a 3×1 mm^2 bar was diced from a 4 inch bonded wafer pair and was

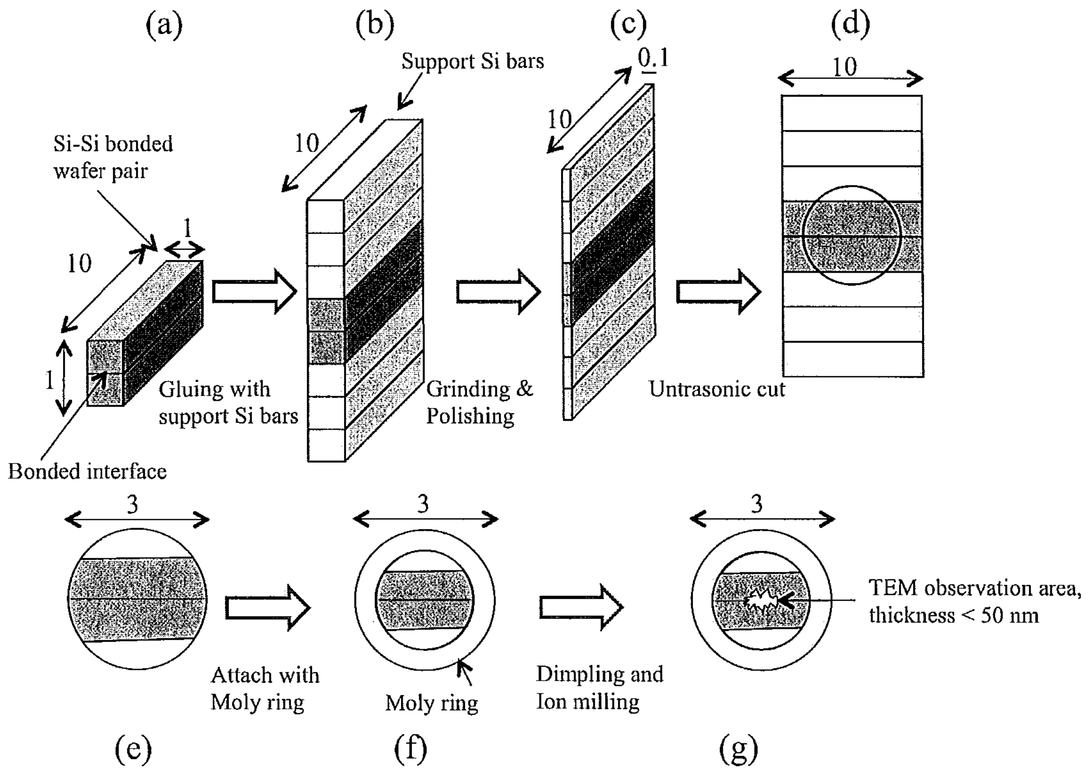

Figure 2.8: Schematic of TEM specimen preparation steps for Si/Si bonded wafers. The dimensions shown are in millimeters.

placed between six supporting silicon bars on two sides (Fig. 2.8 b). All these eight specimens were bonded together using Epo Tek H20S silver epoxy to make a single structure. Second, the structure was first grinded and then polished to thin down to ~100 μm (Fig. 2.8 c). Third, a 3 mm disc was cut from the structure using ultrasonic cutter (Fig. 2.8 d) and then placed on a Moly ring (Fig. 2.8 f). Forth, the centre of the disc was further thinned down to ~ 15 μm using a dimple machine. Fifth, the disc was further thinned by ion sputtering in an ion mill until holes appeared (2.8 g). Finally, the high resolution

images were taken using JEOL 2100F, C_s=0.50 mm transmission electron microscope. In case of silicon/glass bonded pair, the specimen for HRTEM was prepared using focused ion beam (FIB) to avoid the charging induced artifacts on the specimen [46].

2.6.5 Electron Energy Loss and Energy Dispersive X-Ray Spectroscopy

Electron energy loss spectroscopy (EELS) and energy dispersive X-ray spectroscopy (EDX) were performed in this study to understand the elemental composition at and around the bonded interface. These techniques are useful to find if there is any diffusion of elements from one wafer to the other. The compositional analysis allows understanding the bonding mechanism of the wafers. A good understanding in the bonding mechanism is required to address the bonding challenges and further improve the bonding quality. While EDX is particularly sensitive to heavier elements, EELS works better for elements with relatively low atomic number [47]. Hence both EDX and EELS were performed in this study to explore the presence of possible elements at and around the interface.

To investigate the elemental composition at the bonded interface, high angle annular dark-field (HAADF)-scanning TEM (STEM), EELS and EDX were performed with the specimen prepared for HRTEM. The EELS and EDX experiment was performed using a field-emission TEM (JEOL 2100F, C_s=0.50 mm) in conjunction with a Gatan Enfina 1000 spectrometer, operating at 200 kV. The energy resolution was about 1.0 eV. Typical probe conditions for EELS used in this work consisted of 1.0 nm diameter probe in TEM condition and a ~ 0.3 nm diameter probe with a convergence semi-angle of 14

mrad in STEM condition. Core-loss EELS spectra of N-K, Si-$L_{2,3}$, and O-K were recorded.

CHAPTER 3. SEQUENTIALLY PLASMA ACTIVATED BONDING OF SILICON/SILICON

3.1 Introduction

The sequentially plasma activated bonding (SPAB) requires improved surface properties of the mating wafers, such as hydrophilicity and roughness. These determine the quality of the bonded interface, such as bonding strength, electrical characteristics and nucleation of voids. The improved surface properties and hence the bonded interface properties can be obtained through proper choice of plasma parameters (gas, plasma discharge mode, plasma power, chamber pressure, activation time). Therefore, it is indispensable to understand the role of plasma parameters on the surface and bonded interface properties.

Further, the SPAB bonded interface properties may change during fabrication process flow at high annealing temperatures in some applications. Due to the presence of OH^-groups, the high temperature annealing may nucleate voids at the interface and change the interfacial morphology. The interface morphology controls the bonding strength and current transport properties of the bonded interface. Hence, study on the influence of annealing on void nucleation, interface morphology, bonding strength and electrical characteristic is indispensable to understand the applicability of SPAB for micro/nano-scale devices.

This chapter discusses an in-depth analysis of hydrophilicity and surface roughness of silicon (Si) wafers with different plasma parameters to figure out how

sequential plasma activates surfaces for spontaneous bonding at nanometer-scale. Further, the influence of plasma parameters on voids' nucleation and electrical conductivity of Si/Si bonded interface has been investigated. Furthermore, the influence of annealing on voids' nucleation, bonding strength, electrical characteristics, morphology and composition of the Si/Si nano-bonded interface has been explored.

Note that most of the results presented in this chapter are published in two peer-reviewed journal articles [48-49]. Some unpublished results are also included. The sequence of the write-up in the thesis is different from the published articles because of extensive motivations of the thesis. For the article in Ref [48], I was primarily responsible for literature search, for writing the manuscript and for the experiments. For Ref. [49], I was primarily responsible for literature search, for writing the manuscript and partially for the experiments.

3.2 Surface Characterization of Silicon

3.2.1 Surface Hydrophilicity

Role of Gas

In order to choose appropriate gas for plasma activation, the contact angle measurements of Si before and after surface activation in the RIE and MW plasma using O_2, N_2 and Ar gas were performed. As mentioned in chapter 2, contact angle measurements allow understanding the hydrophilicity of the wafer surface. The lower the contact angle, the higher the hydrophilicity and the easier the spontaneous bonding at

room temperature. In this study, the surface hydrophilicity was investigated through contact angle measurements after three minutes of plasma activation in order to understand the applicability of SPAB, especially in bonding and packaging environments where a few minutes may be required for handling and aligning after surface activation.

Table 3.1: The average contact angles of a drop of DI water on Si wafer surface with different gases in RIE plasma condition.

RIE Plasma	Gas	Power (W)	Time (s)	Pressure (Pa)	Contact Angle (°)
1	O_2	200	30	60	29.10
2	N_2	200	30	60	43.76
3	Ar	200	30	60	51.76

Table 3.1 shows the contact angles of a drop of DI water on Si wafer surface after plasma activation using different gases in RIE plasma condition. The contact angles were 29.1, 43.76 and 51.76 degrees for O_2, N_2 and Ar gases, respectively. The O_2 RIE plasma activation offered lowest contact angle, in other words, highest hydrophilic surfaces compared to the N_2 and Ar RIE plasma activated Si surfaces. The change in contact angle with gas is presumably due to the different etching behavior and chemical reactivity of gases. The physical sputtering process in RIE plasma changes the surface roughness.

Table 3.2: The average contact angles of a drop of DI water on Si wafer surface with different gases in MW plasma condition.

MW Plasma	Gas	Power (W)	Time (s)	Pressure (Pa)	Contact Angle (°)
1	O_2	2000	30	60	27.36
2	N_2	2000	30	60	16.14

This change in surface roughness is presumably responsible for change in contact angle with different gases. Table 3.2 shows the contact angles on Si surfaces activated using MW O_2 and MW N_2 radicals. The results imply that MW N_2 radicals offer higher hydrophilic surfaces (i.e., lower contact angle) compared to MW O_2 radicals, under identical plasma conditions (i.e., power, time and pressure). This behavior of the MW N_2 radicals can be explained as follows. The MW N_2 radicals are highly reactive resulting in Si oxynitride (SiO_xN_y) and Si-N bonds while reacting with O_2 and Si [50]. These bonds control the water contact angles. The water contact angle largely depends on two factors, dispersion γ_d and polar γ_p components of the surface energy. The higher the polar contribution (γ_p) to the surface energy, the better the hydrophilicity of a polar liquid, such as, water [51]. While the presence of Si-N bonds on the MW N_2 radicals treated surface leads to higher polar contribution, the presence of Si-O bond on the MW O_2 radicals treated surface results in lower polar contribution to the surface energy [52]. Hence, the MW N_2 radicals activated surface is much more hydrophilic than the MW O_2 radicals activated surface.

Immediately after plasma activation, Si wafer surfaces are terminated by large numbers of dangling bonds, and they can react with surrounding atmosphere, such as water, impurity components, or with other dangling bonds. To clarify the ageing process of the plasma activated surfaces, a droplet of DI water was placed on a Si wafer surface and the contact angles were measured every three seconds. Figure 3.1 shows the contact angles versus exposure time in air after plasma activation with different gases. The rate of change of contact angle with time refers to surface reactivity. Therefore, it can be inferred

from figure 3.1 that the reactivity of O_2 RIE plasma is lower than that of N_2 and Ar RIE plasma. The reactivity of N_2 RIE and Ar RIE is nearly similar. On the other hand, the reactivity of MW N_2 radicals is higher than MW O_2 radicals.

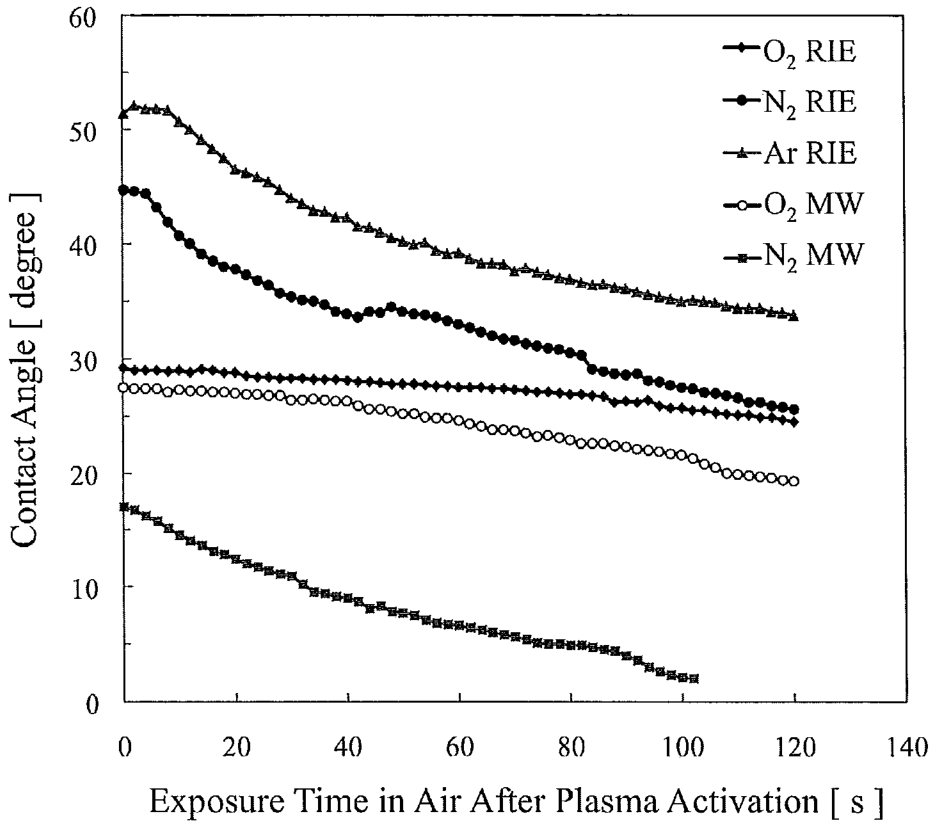

Figure 3.1: Contact angles of a droplet of DI water on Si wafer surface activated using different gases in RIE and MW plasma conditions.

In terms of surface hydrophilicity, the O_2 RIE plasma and MW N_2 radicals offered the highest hydrophilicity and hence is the best combination for spontaneous bonding at room temperature.

Role of RIE Plasma Parameters

In order to understand the influence of O_2 RIE plasma parameters (i.e., plasma power, chamber pressure, activation time) associated with sequential activation, on the degree of hydrophilicity, the contact angle measurements were carried out with different O_2 RIE plasma parameters. The average measured contact angles at different plasma processing conditions are enlisted in Table 3.3. It also includes the average contact angles of non-activated surface, and hydrophobic surfaces cleaned with diluted (5%) hydrofluoric (HF) acid for comparison. The contact angles of the sequentially activated surface show an increasing trend as O_2 RIE plasma activation time, power and pressure increases. This result can be correlated with the surface roughness, as discussed in section 3.2.2. Furthermore, the physical bombardment process of O_2 RIE plasma removes surface species such as contaminations, carbons, hydrogen, hydroxyl (OH^-) groups, and it creates large numbers of free bonds (dangling bonds) on the surface. It is well known that the more OH^- groups present on the surface, the smaller the contact angle. Increasing the plasma power, pressure, and time enhances the physical bombardment process of O_2 RIE and removes surface OH^- groups more efficiently; thus, this increases the contact angle. It is important to note that the O_2 RIE treatment not only removes surface contaminations, but also produces a plasma induced oxide layer. However, the thickness of this oxide layer does not make significant difference in contact angle and hence surface energy as reported in [41]. When we manipulated with the O_2 RIE plasma power, the lowest contact angle we could achieve was at 75 W. The plasma power at 50 W was not sufficient enough to activate the wafer surfaces, which resulted in a contact angle near to that of a

non-activated surface. It can be concluded from the above results that lowest contact angles can be achieved by choosing the lowest possible O_2 RIE plasma parameters. However, the plasma parameters have to be high enough to sufficiently remove surface contaminations and activate the surface. Our experimental results show that the lowest possible O_2 RIE parameters that can sufficiently activate the surface are 5 s, 75 W, and 40 Pa.

Table 3.3: The average contact angles of a drop of DI water on Si wafer surface with different surface treatment conditions.

<table>
<tr><th colspan="3">O_2 RIE Plasma</th><th colspan="3">MW N_2 radicals</th><th rowspan="2">Contact Angle (°)</th></tr>
<tr><th>Pressure (Pa)</th><th>Power (W)</th><th>Time (s)</th><th>Pressure (Pa)</th><th>Power (W)</th><th>Time (s)</th></tr>
<tr><td rowspan="12">100</td><td rowspan="6">300</td><td>5</td><td rowspan="17">100</td><td rowspan="17">2000</td><td rowspan="17">30</td><td>31.4 ± 1.1</td></tr>
<tr><td>15</td><td>36.8 ± 0.5</td></tr>
<tr><td>30</td><td>38.1 ± 0.5</td></tr>
<tr><td>60</td><td>39.5 ± 0.3</td></tr>
<tr><td>120</td><td>37.7 ± 0.5</td></tr>
<tr><td>300</td><td>40.6 ± 0.3</td></tr>
<tr><td>50</td><td rowspan="11">60</td><td>34.5 ± 0.7</td></tr>
<tr><td>75</td><td>31.5 ± 0.3</td></tr>
<tr><td>100</td><td>38.8 ± 0.6</td></tr>
<tr><td>200</td><td>39.5 ± 0.3</td></tr>
<tr><td>300</td><td>39.5 ± 0.3</td></tr>
<tr><td>400</td><td>43.1 ± 0.5</td></tr>
<tr><td>40</td><td rowspan="5">300</td><td>38.5 ± 0.5</td></tr>
<tr><td>60</td><td>41.0 ± 1.3</td></tr>
<tr><td>80</td><td>39.4 ± 0.2</td></tr>
<tr><td>100</td><td>39.5 ± 0.3</td></tr>
<tr><td>120</td><td>40.1 ± 1.0</td></tr>
<tr><td colspan="6"></td><td></td></tr>
<tr><td colspan="6">Without Activation</td><td>33.4 ± 0.2</td></tr>
<tr><td colspan="6">HF Cleaning [5%]</td><td>65.2 ± 0.4</td></tr>
<tr><td colspan="6">RCA Cleaning [H_2O:H_2O_2:NH_4OH=5:1:1]</td><td>9.9 ± 0.4</td></tr>
<tr><td colspan="6">Only O_2 RIE Activation [100 Pa, 300 W, 30 s]</td><td>43.0 ± 0.4</td></tr>
<tr><td colspan="6">Only MW N_2 Activation [100 Pa, 2000 W, 30 s]</td><td>26.1 ± 2.3</td></tr>
</table>

Figure 3.2 depicts the contact angles as a function of exposure time in air after sequential activation compared with O_2 RIE plasma activation, MW N_2 radicals' activation, diluted (5%) HF cleaning and the contact angles of non-activated surface. For sequential activation O_2 RIE parameters were 300 W, 100 Pa and 15 sec and MW N_2

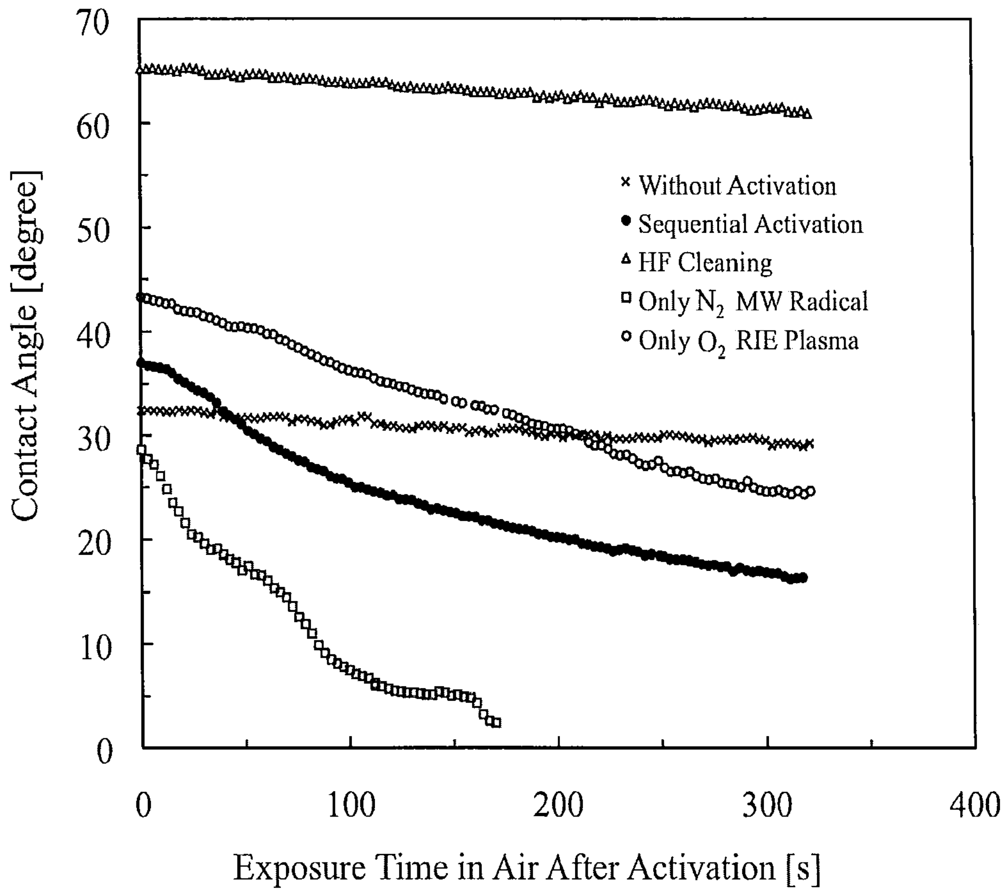

Figure 3.2: Contact angles of a droplet of DI water on Si wafer surface activated using different plasma conditions.

parameters were 2000 W, 100 Pa and 30 sec. The plasma parameters for only O_2 RIE and only MW N_2 activation are given in Table 3.3. The measurement errors associated with this experiment were ±10 %. While the contact angle of HF cleaned and without

activated wafer surface slowly decreased over time, the contact angle of plasma activated surfaces decreased rapidly over time. The contact angle for the MW N_2 treated surface went below the detection limit (within 176 seconds). As mentioned previously, the rate of change of the contact angle refers to surface reactivity. This indicates that MW N_2 radicals' treated surface is highly reactive. The highly reactive nature of MW N_2 radicals turns the sequentially activated surfaces into high reactive surfaces, as opposed to HF treated surface and non-activated surface. On the other hand, the contact angles of O_2 RIE treated surfaces were higher than that of MW N_2 treated surfaces and sequentially activated surfaces. The contact angles of sequentially plasma activated surfaces were less than that of O_2 RIE plasma treated surfaces but greater than that of MW N_2 radicals' activated surfaces throughout the elapsed time. In fact, O_2 RIE is required to remove surface contaminations and MW N_2 is required to create a highly reactive surface. Hence, both plasmas are essential to activate the surface for bonding. The decrease of the contact angle (i.e., increase in surface energy) over storage time may be correlated with the increase of bonding strength over storage time. It has been reported that the bonding energy of sequentially plasma activated Si/Si interface significantly increases from ~ 0.05 J/m^2 to 2.3 J/m^2 after storage at room temperature (RT) for 24 hours [53]. Increasing the elapsed time generates stronger bonds between the sequentially treated surfaces as a result of SiO_xN_y or Si-N. A similar mechanism in the reduction of contact angle of the sequentially activated surface left in the air also explains the increase in surface energy due to SiO_xN_y or Si-N structures.

Role of MW plasma Parameters

In order to understand the influence of MW plasma parameters on surface hydrophilicity, the contact angle measurements were performed after activating the Si surface with different MW power, time and pressure. Table 3.4 shows the average contact angles (estimated from three drops) with different MW plasma parameters. No significant change in contact angle was observed with MW power, time and pressure. In fact, the MW radicals are not accelerated by the DC self-bias voltage. Therefore, the MW radicals do not physically bombard the wafer surface. Hence, the physical sputtering process does not occur in case of MW plasma activation.

Table 3.4: The average contact angles of a drop of DI water on Si wafer surface with different parameters of MW N_2 radicals.

<table>
<tr><th colspan="3">O_2 RIE Plasma</th><th colspan="3">MW N_2 Radicals</th><th rowspan="2">Contact Angle (°)</th></tr>
<tr><th>Power (W)</th><th>Time (s)</th><th>Pressure (Pa)</th><th>Power (W)</th><th>Time (s)</th><th>Pressure (Pa)</th></tr>
<tr><td rowspan="9">300</td><td rowspan="9">60</td><td rowspan="9">100</td><td>1500</td><td rowspan="3">60</td><td rowspan="6">100</td><td>36.26</td></tr>
<tr><td>2000</td><td>36.64</td></tr>
<tr><td>2500</td><td>40.28</td></tr>
<tr><td rowspan="6">2000</td><td>30</td><td>40.72</td></tr>
<tr><td>60</td><td>36.64</td></tr>
<tr><td>120</td><td>41.88</td></tr>
<tr><td rowspan="3">60</td><td>50</td><td>41.18</td></tr>
<tr><td>100</td><td>36.64</td></tr>
<tr><td>150</td><td>39.14</td></tr>
</table>

Presumably, due to the absence of physical bombardment process, the surface roughness did not change significantly. Hence, the contact angle did not change remarkably. To find insights into the contact angle results, surface roughness of Si was

measured after plasma activation with different gases and plasma parameters. The following section discusses the influence of gas on surface roughness.

3.2.2 Surface Roughness

Role of Gas

To investigate the influence of gas on surface roughness, Si surfaces were activated with different gas, and the surface roughness was measured using atomic force microscopy (AFM). Figure 3.3 shows the AFM images of Si wafer surface after activation with (a) O_2 RIE, (b) N_2 RIE and (c) Ar RIE plasma. Table 3.5 shows the RMS roughness of Si surface for different gas. The results indicate that O_2 RIE plasma offers

Table 3.5: The RMS surface roughness of Si wafer after activation with RIE plasma produced from different gases.

RIE Plasma	Gas	Power (W)	Time (s)	Pressure (Pa)	RMS Roughness (nm)
1	O_2	200	30	60	0.13
2	N_2	200	30	60	0.18
3	Ar	200	30	60	16.2

the lowest surface roughness of Si among O_2, N_2 and Ar RIE plasma activation. Anomalous Si surface morphology was observed after Ar plasma activation, as shown in figure 3.3 (c). Further research is required to understand insights into these results, which is beyond the scope of this study. The surface roughness results can be correlated to the contact angle results in Table 3.1. One can infer from these results that the higher the surface roughness (Table: 3.5), the higher the contact angle (Table: 3.1). In case of rough

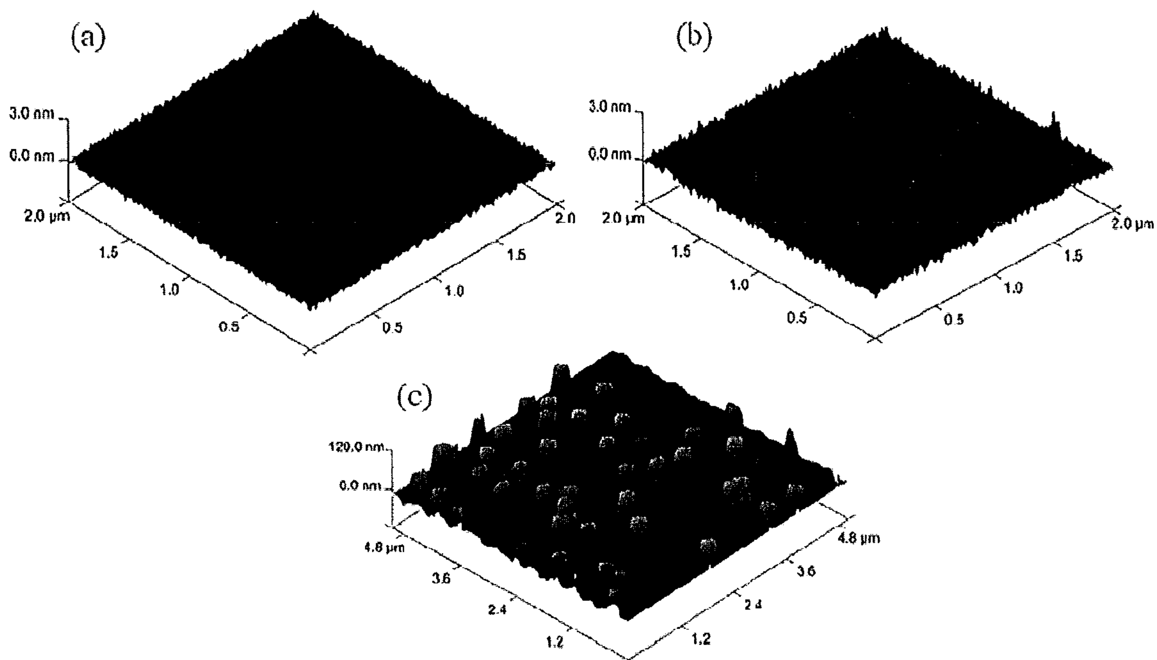

Figure 3.3: AFM images of Si wafer surface after activation with (a) O_2 RIE, (b) N_2 RIE, and (c) Ar RIE plasma.

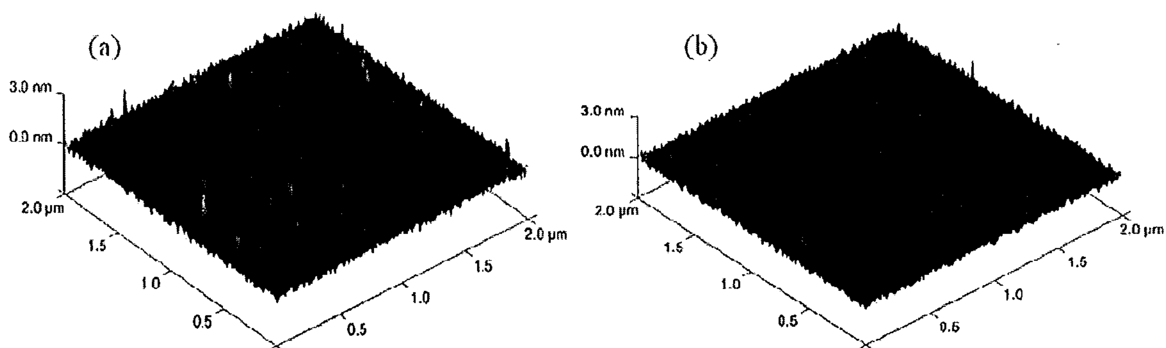

Figure 3.4: AFM images of Si wafer surface after activation with (a) MW O_2, and (b) MW N_2 radicals.

surface, air traps between the water droplet and the wafer surface and hinders spreading the water droplet. This results in higher contact angle. Figure 3.4 shows the AFM images of Si surface after activation with MW O_2 and MW N_2 radicals. Table 3.6 shows the RMS surface roughness of Si after activation with MW O_2 and MW N_2 radicals. The MW N_2 radicals offered much smoother surface than MW O_2 radicals. This result is consistent with contact angle results in Table 3.2, where MW N_2 radicals offered lower contact angle than MW O_2 radicals.

Based on the contact angle and surface roughness results, in order to achieve lowest contact angle (highest hydrophilicity) and lowest surface roughness, O_2 gas was chosen for RIE plasma activation and N_2 gas was chosen for MW radicals' activation.

Table 3.6: The RMS surface roughness of Si wafer after activation with MW radicals produced from different gases.

MW Radicals	Gas	Power (W)	Time (s)	Pressure (Pa)	RMS Roughness (nm)
1	O_2	2000	30	60	0.20
2	N_2	2000	30	60	0.18

Role of RIE Plasma Parameters

The physical sputtering process of RIE plasma treatment cleans and activates (i.e. forms new bonding sites) surfaces to achieve strong bonding strength at room temperature [54-55]. However, the accelerated oxygen ions in the O_2 RIE plasma process damage the surface and increase the surface roughness resulting in the formation of voids [56]. To understand the influence of RIE plasma parameters on the surface roughness,

seven Si wafers (A1, A2, A3, B1, B2, B3 and C) were activated using the plasma parameters as shown in Table 3.7. After activation, the surface roughness was investigated using AFM.

Table 3.7. The plasma parameters used for Si surface activation.

Specimen No.	O_2 RIE Plasma			MW N_2 Radicals		
	Power (W)	Time (s)	Pressure (Pa)	Power (W)	Time (s)	Pressure (Pa)
A1	200	15	60	2500	30	60
A2		30				
A3		60				
B1	200	30	60	2500	15	60
B2	300					
B3	400					
C	300	30	60	—	—	—

Figure 3.5 shows the dependence of surface roughness of Si on the O_2 RIE time and power in the sequential activation. The measurements were repeated three times and the average roughness is shown in figure 3.5. Before activation, the RMS surface roughness was 0.17 nm. After 15 s O_2 RIE activation, the RMS roughness decreased to 0.14 nm. Further increase in activation time to 60 s resulted in an increase in roughness, but still lower than that of before activation. As seen from figure 3.5, the surface roughness also increased with the increase in O_2 RIE power. However, the rate of increase in the surface roughness with the increase in the O_2 RIE power is higher compared to the O_2 RIE time. The slopes for the surface roughness curves differ, indicating different etching behaviors of O_2 RIE time and power. While a smooth surface (roughness 0.12 nm) was observed at 200 W, it was rough (roughness 0.23 nm) at 400 W.

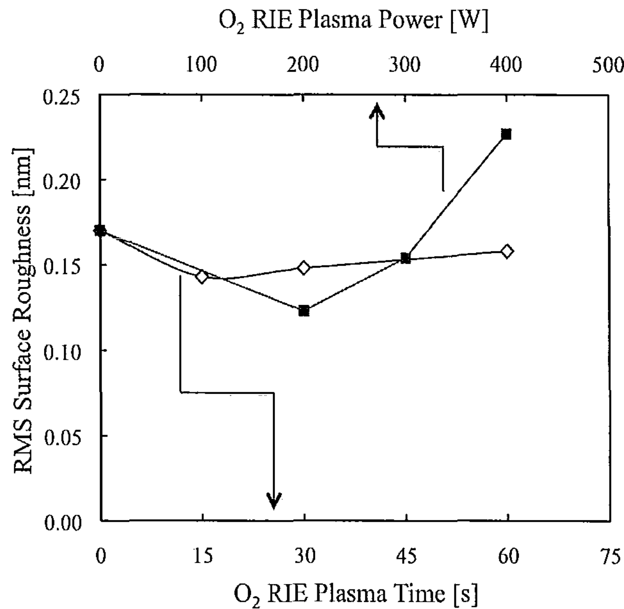

Figure 3.5: Surface roughness of Si as a function of O_2 RIE plasma time and power in the SPAB.

This result is in agreement with previous studies [57], where bonding energy was correlated with surface roughness. A comparative view on the surface roughness is given in figure 3.6. It includes the AFM images of Si surface (a) before activation, and after activation at processing conditions for the specimens (b) C, (c) B1, and (B3). The AFM images show that the Si surface becomes smooth after activation (compare 3.6 a and c). As increasing the activation power from 200 W (figure 3.6 c) to 300 W (figure 3.6 b), the surface roughness increased. This trend is continued. In fact, the increase in plasma power fortifies the physical bombardment process of ionized particles. Once the surface is free from native oxides, particles and contaminations, the energetic ionized particles start digging the surface and create nano-defects such as nano-pores and craters on the surface. In particular, there were a significant number of such defects present on the

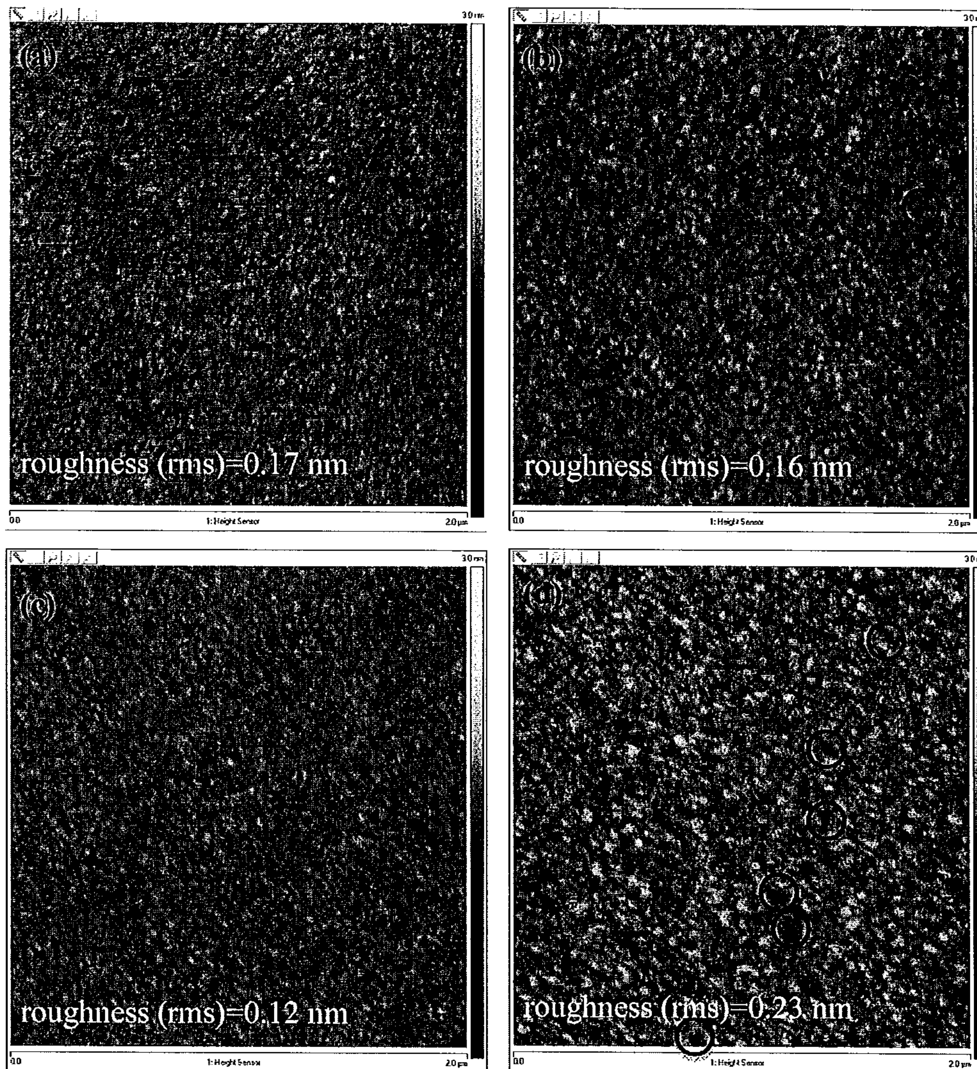

Figure 3.6: AFM images of Si surface (a) before, (b) after O_2 RIE activation with 300 W for 30 s (specimen C), (c) after O_2 RIE activation with 200 W for 30 s followed by MW N_2 radicals activation with 2500 W for 15 s (specimen B1), and (d) after O_2 RIE activation with 400 W for 30 s followed by MW N_2 radicals activation with 2500 W for 15 s (specimen B3).

whole surface of the specimen treated with 400 W O_2 RIE. Red circles on the images indicate some nano-pores. The estimated depth of the nano-pores was as deep as 2.2 nm. This finding confirmed porosity on the activated surfaces of Si, which was assumed in

[58]. The nano-pores and craters act as trapping sites for the gas at the bonded interface and results in interfacial voids. The nucleation of voids is discussed in section 3.3.1.

Role of MW Plasma Parameters

The influence of MW plasma parameters on the surface roughness were investigated through AFM. The MW power, time and pressure were varied from 1500 - 2500 MW, 30-120 s and 50-150 Pa, respectively. No significant change in surface roughness was observed with MW power and time. The RMS surface roughness was varied between 0.2 to 0.23 nm with different MW power and time. However, remarkable influence of chamber pressure was observed on Si surface roughness. While 50 Pa pressure resulted in RMS surface roughness of 0.19 nm, 150 Pa chamber pressure resulted 0.48 nm RMS roughness. This result is consistent with previous studies [40]. The increase in surface roughness with chamber pressure is attributed to the increase in chemical reactivity and total gas fluence on the wafer surface.

3.3 Interface Characterization before Annealing

3.3.1 Interfacial Voids

In general, voids form due to surface roughness, surface particles, and residual particles on surface due to plasma bombardment. Smooth surface (RMS roughness < 0.5 nm) is required in order to avoid air-trapping induced voids across the interface. While the voids due to surface particles can be controlled by the proper cleaning of surface and

use of particle free bonding environment (e.g., clean room), the sequential plasma processing parameters such as O_2 RIE plasma time, power and gas pressure induced

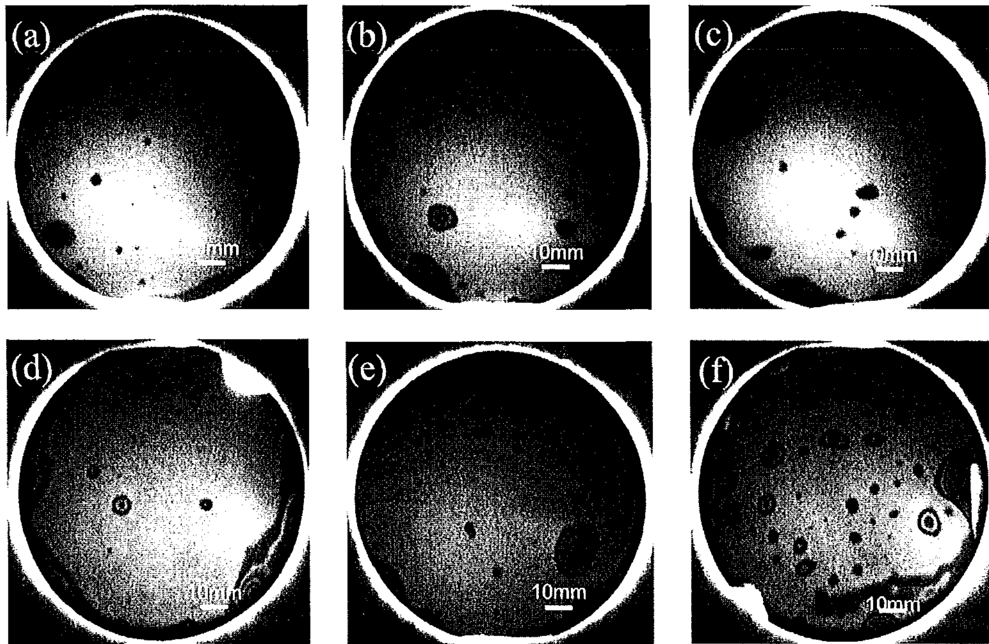

Figure 3.7: IR transmission images of Si/Si SPAB interfaces showing the influence of the O_2 RIE time (a) 15 s, (b) 30 s, (c) 60 s, and power (d) 200 W, (e) 300 W, and (f) 400 W on void formation.

voids can be detrimental to the quality of the bonded interface [41, 56]. In order to understand the role of plasma induced nucleation of voids, infrared (IR) transmission images for the SPAB Si/Si interfaces as a function of plasma processing parameters such as O_2 RIE plasma time and power were taken for the bonded specimens as shown in Table 3.7. As shown in figure 3.7 (a), (b) and (c), no significant relationship between the O_2 RIE plasma time and the void formation in the SPAB process was observed. On the other hand, the number of voids were increased rapidly with increasing O_2 RIE plasma power especially at 400W, as shown in figure 3.7 (f). A comparison between the

influence of O_2 RIE time and power indicates that the O_2 RIE plasma power has dominant role on the formation of voids compared to O_2 RIE time. This result can be correlated to the increase in surface roughness with RIE power as shown in figure 3.5. The increased surface roughness at 400 W is responsible for the increased void nucleation (figure 3.7 f).

3.3.2 Electrical Characterization

The influence of the plasma processing parameters on the electrical characteristics of the bonded interface was investigated using *I-V* measurements. Figure 3.8 shows the *I-V* curves of the *p*-Si/*p*-Si bonded interface with different O_2 RIE plasma exposure times measured at RT. It has been reported [59] that sequential plasma activated wafers form covalent bond across the bonded interface 24 hours after bonding. Hence, the *I-V* measurements were done 24 hours after bonding. After 24 hours, no significant change in *I-V* characteristics with storage time was found. From figure 3.8 it is evident that the electrical resistance increased as the O_2 RIE plasma activation time increased. The slow turn on of the forward and reverse bias current indicates that a thin barrier layer is present at the bonded interface [60]. The experimental measurement of the oxide thickness on the O_2 RIE plasma activated Si surfaces showed that the initial high oxide growth rate saturated at around 60 Å after approximately 100 s plasma activation [61]. This result can be directly correlated with the electrical behavior shown in figure 3.8. It is seen that the positive bias current saturates after approximately 100 s of plasma activation time.

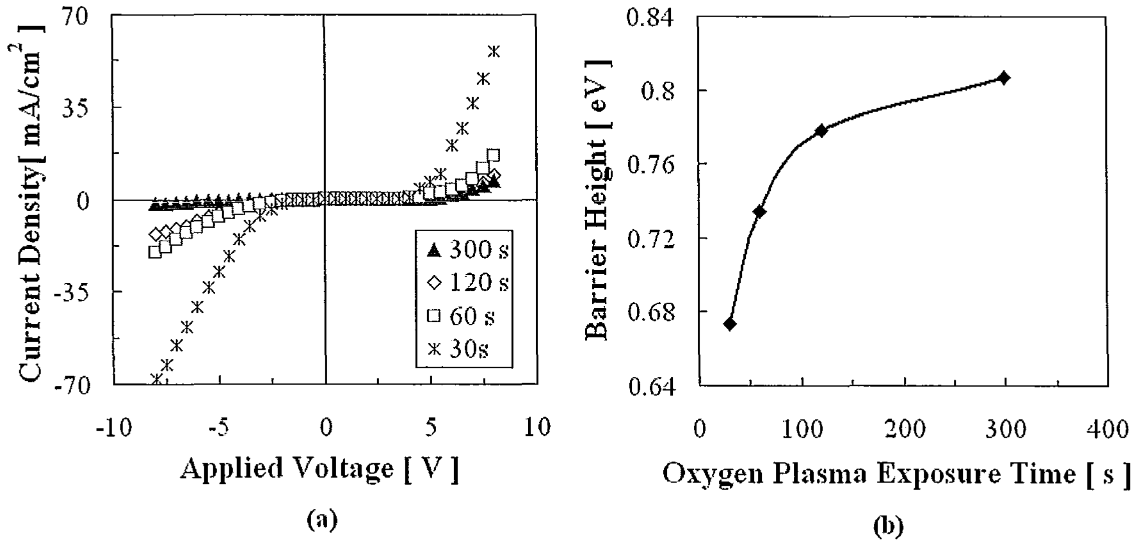

Figure 3.8: (a) Current-voltage characteristics, and (b) barrier height of the bonded *p*-Si/*p*-Si interface as a function of O_2 RIE plasma activation time.

Electrical resistance at an arbitrarily chosen voltage of 4 volt for 30 s of plasma activation time was calculated to be 778.4 KΩ. This high resistance is attributed to the presence of plasma induced charges and extra energy states at the bonded interface and at the band gap of the semiconductor, respectively. This was confirmed with the nonlinear *I-V* characteristics in figure 3.8. The presence of charges at the Si/Si bonded interface was also confirmed by a transient current response to a step voltage [62]. It has been reported that the O_2 RIE plasma activation can increase the fixed oxide charge by 2.9×10^{10} cm^{-2} and interface trap density to 7.2×10^{10} cm^{-2}eV^{-1} [63]. These oxide charges form depletion region surrounding the bonded interface. The fixed oxide charges and interface traps generate extra energy states at the forbidden energy gap; which increase the barrier height at the bonded interface. This energy barrier hinders the flow of the majority carriers at the conduction band of the semiconductor; and thus results in high electrical resistance. Since

the barrier height follows the same trend as the oxide thickness across the bonded interface [61], the oxide thickness has dominant role in increasing the interface resistance.

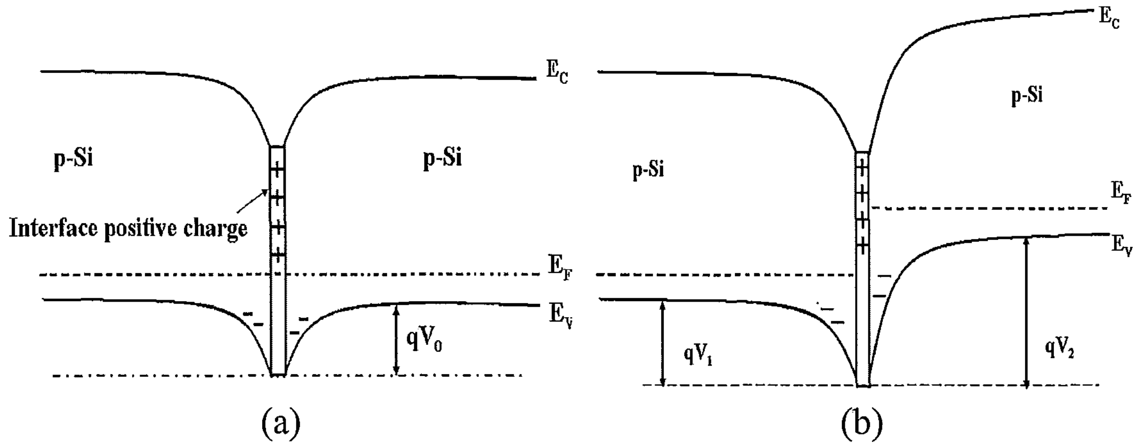

Figure 3.9: Schematic energy band diagram of a p-Si/p-Si bonded structure at (a) zero bias, and (b) with applied bias.

For p-type Si, positive charges form at the bonded interface that is balanced by negatively charged ionized acceptor atoms at the depletion region. A schematic energy band diagram of a p-Si/p-Si is shown in figure 3.9. For lower doping ($\leq 10^{17}$cm^{-3}) concentration, the current transport is dominated by the thermionic-emission current. Using the thermionic emission model, the current density can be expressed as [64-65],

$$J = A^* T^2 \exp(-\frac{qV_b}{kT})\left[\exp(\frac{qV_2}{nkT}) - \exp(-\frac{qV_1}{nkT})\right] \tag{3.1}$$

and $V = V_1 + V_2$, where A^* is the effective Richardson constant, T the temperature, q the electronic charge, k the Boltzmann's constant, V_b the barrier height and n the ideality factor. V is the total applied bias, which is distributed over the interface with V_1 and V_2

components as shown in figure 3.9. The barrier height can be determined from the *I-V* characteristics in the forward direction with,

$$V_b = \frac{kT}{q} \ln(\frac{AT^2}{J_0}) \tag{3.2}$$

where, J_0 is the extrapolated value of current density at zero voltage. Assuming A*=114 A/cm^2/K^2 and T=300 K, the barrier height was determined and plotted in figure 3.8 (b). The barrier height increased with the increase of O_2 RIE plasma time. The slope of the barrier height from 30 s to 120 s is higher than it is from 120 s to 300 s. The barrier height at 300 s almost looks saturated. The increase of barrier height with the increase of O_2 RIE plasma time can be attributed to the increase of oxide thickness at the bonded interface [61]. The calculated barrier height of the bonded interface is higher than that of the chemically activated hydrophilic bonded interface [67]. This is attributed to the contact resistance between silver paste and Si, and the plasma induced crystalline defects and interface fixed charges [66]. In fact, this additional contribution to the barrier height can be neglected for this comparative study. From the above results, it can be concluded that the current transport across the bonded interface can be controlled by a proper choice of the O_2 RIE plasma activation time.

3.4 Interface Characterization after Annealing

Wafer bonding is one of the key process steps in a real device fabrication process flow. For some device fabrication, wafer bonding is carried out at the very beginning of the fabrication process. Thus the bonded wafer can undergo several process steps where it

can be exposed to high temperature. For example, in smart-cut process to fabricate silicon-on-insulator (SOI) substrate, ion implanted and bonded specimens go through high temperature annealing step which is required for layer transfer [68]. These high temperature processes can change the interface morphology, and nucleate interfacial voids. Nucleation of voids can reduce the bonding strength and hence the sealing behavior of the device. Furthermore, morphological change of the interface is presumably correlated to the current transport properties of the device. Thus study of the influence of annealing on the bonded interface is indispensable to understand the insights. The following section discusses the influence of annealing on the nucleation of voids at the bonded interface.

3.4.1 Influence on Voids' Nucleation

In order to investigate the influence of annealing on the nucleation behavior of voids, all the specimens shown in Table 3.7 were sequentially annealed up to 900°C in air or nitrogen environments. Before annealing, the IR images were taken for all the specimens. Then, all the specimens were annealed at 200, 400, 600, 800 and 900°C. The interfaces were observed after each annealing steps using IR transmission camera. At all five temperatures the specimens were annealed for 4 hours with a ramping rate of 200°C per hour. As a reference, the IR transmission images of non-activated Si/Si bonded interfaces are shown in figure 3.10. Since the surfaces were not treated with plasma, plasma induced voids was not observed (Fig 3.10 a). A few particle induced voids were remained at the interface which did not remove after annealing. A significant number of

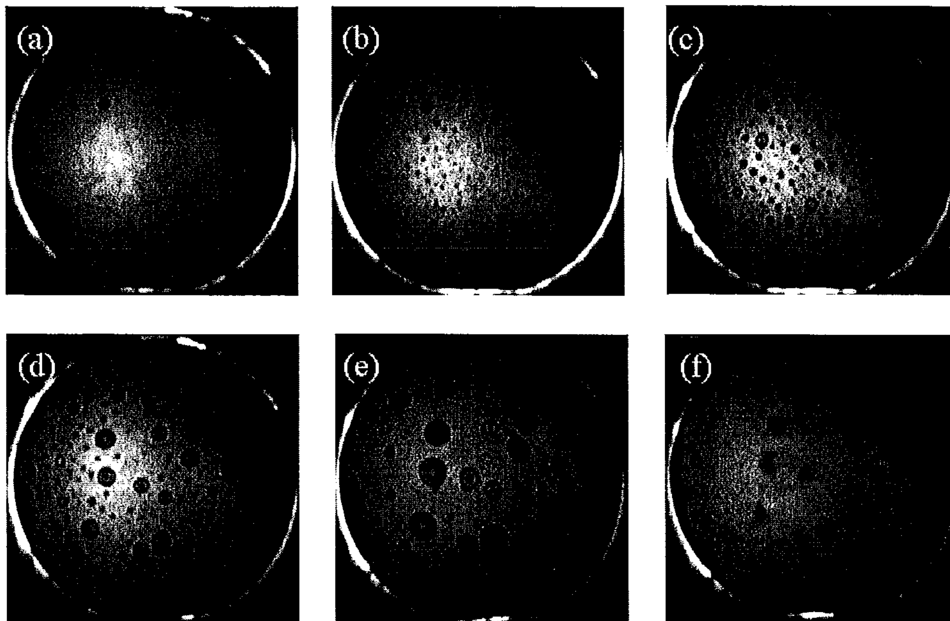

Figure 3.10: IR transmission images of nonactivated reference Si/Si interfaces (a) before (at room temperature), and after sequential annealing at (b) 200, (c) 400, (d) 600, (e) 800, and (f) 900°C in nitrogen ambient for 4 hours in each step.

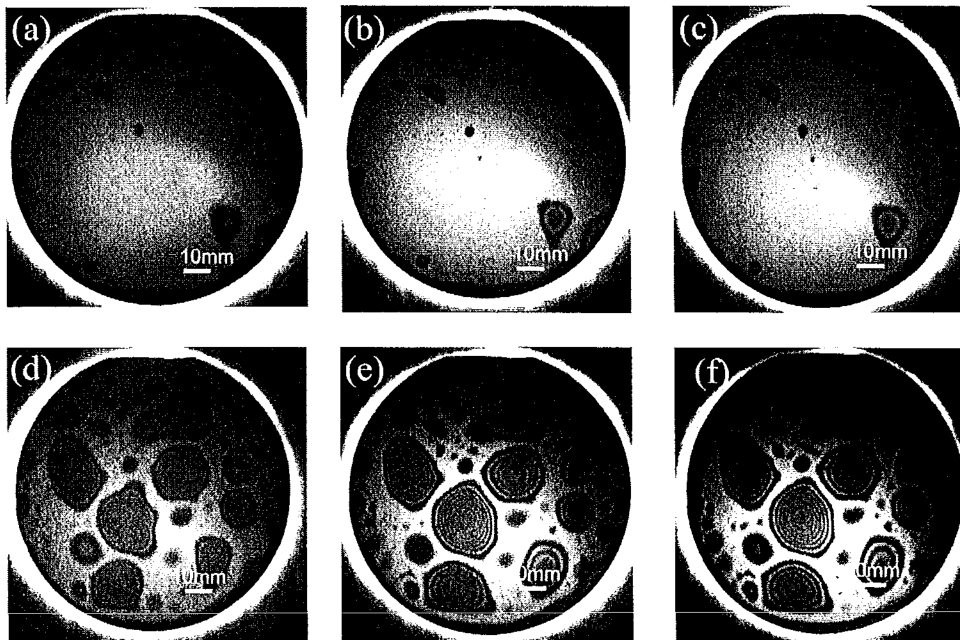

Figure 3.11: IR transmission images of O_2 RIE treated Si/Si interfacial voids for the specimen C (a) before (at room temperature), and after sequential annealing at (b) 200, (c) 400, (d) 600, (e) 800, and (f) 900°C in nitrogen ambient for 4 hours in each step.

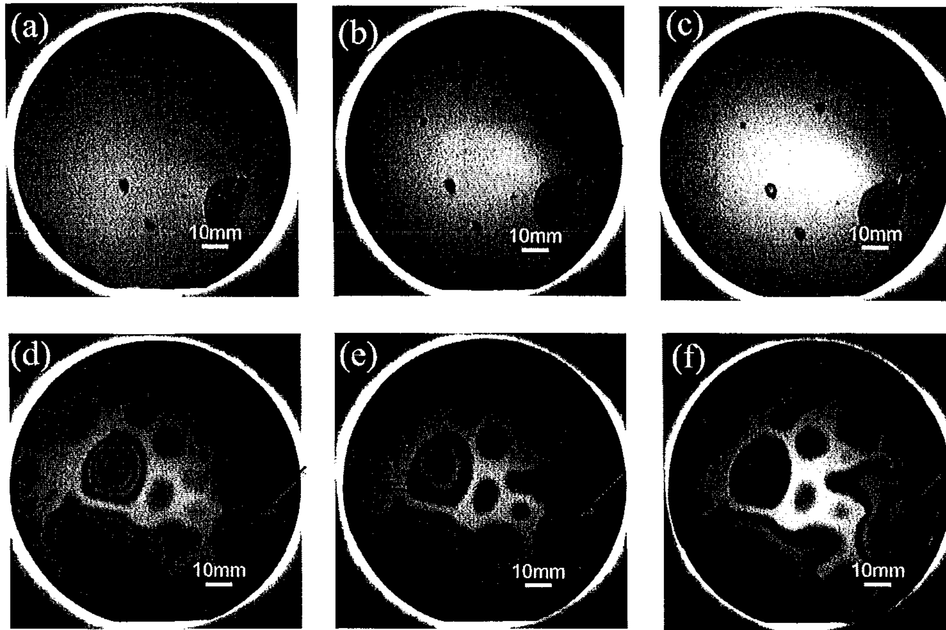

Figure 3.12: IR transmission images of SPAB treated Si/Si interfacial voids for the specimen B2 (a) before, and after sequential annealing at (b) 200, (c) 400, (d) 600, (e) 800, and (f) 900°C in nitrogen ambient for 4 hours in each step.

voids were observed after annealing. The size of the voids increased with annealing temperature up to 800°C, but their density decreased. After 900°C annealing, the thermal induced voids were nearly disappeared. Figure 3.11 and 3.12 shows the annealing dependent voids nucleation for only O_2 RIE treated specimens (C) and SPAB specimen (B2), respectively.

The specimens were annealed up to 900°C in nitrogen gas with a flow rate of 90 standard cubic centimeters per minute (sccm). The voids were not significantly changed up to 400°C both in the O_2 RIE and SPAB. From 600°C, new voids appear due to thermal annealing (now on termed as thermal voids) with the presence of the original voids due to plasma processing (termed as plasma voids). The size and shape of the voids at the SPAB

interface (Fig 3.12) was higher than that of the only O_2 RIE processed interface (Fig 3.11). In both cases, the size and shape of a few plasma voids were changed with a few Newton rings. The Newton rings result from the partial transmission and reflection of light from the air-Si interface at the unbonded regions [69].

The sizes of thermal voids were much bigger compared to that of the plasma voids. The nucleation of thermal voids is attributed to the generation of hydrogen gas from the oxidation reaction of Si by the adsorbed water [70]. From 600°C, perfectly bonded regions surrounded the thermal voids. No significant change of void evolutions was observed after 600°C. Therefore, further annealing at higher temperatures neither generated voids nor changed the size and shape of the thermal voids. If one takes a look on the plasma induced void (as indicated by arrows in Fig 3.12) and its evolutions after annealing, one can detect a thermal void which is preferentially grown at the plasma induced defect site. A comparison of the IR images at 600 (Fig. 3.12 d), 800 (Fig. 3.12 e) and 900°C (Fig. 3.12 f) indicates that once the size and shape of the voids are defined at 600°C, they cannot be changed by thermal viscous flow because of high bonding strength at the surrounding area of the voids already formed at 600°C. The larger size of the bubbles in the SPAB compared to that of the O_2 RIE processed interface is attributed to the presence of N_2 radicals in the SPAB. The N_2 radicals produce highly reactive surfaces. The high chemical reactivity of the sequential plasma treated surfaces may adsorb higher amount of water molecules before bonding than the O_2 RIE plasma activated surfaces, resulting in more H_2 at the interface from Si oxidation and hence larger voids.

As previously seen, the thermal voids were grown preferentially at plasma induced defect sites on the activated surfaces. Therefore, the investigation of the voids nucleation associated with their transitions (i.e., abrupt changes) offers insight into the size and shape of the nucleated voids. Figure 3.13 shows the transitions of thermally nucleated voids at the SPAB interfaces as a function O_2 RIE time and power at 600°C. Due to the dominant role of O_2 RIE power in the void formation (as seen in Fig 3.7 f) in the SPAB, the dependence of the voids formation on the O_2 RIE power was investigated after annealing the specimens in the inert media using nitrogen gas. On the other hand, the O_2 RIE time treated specimens were annealed in air to see the environmental influence on the bonded interface. The transitions of the voids nucleation for all the specimens regardless of RIE time and power occurred at 600°C except for the specimen treated with 400 W O_2 RIE. For the specimen treated with 400 W O_2 RIE, the transition of the voids nucleation was occurred at 800°C. The results indicate that viscous flow of oxides is required for the transition of voids. Viscous flow of oxides occurs only when there is excess gas, which cannot be accommodated (i.e., trapped) at the defect sites. Therefore, the transition of voids for the specimen treated with 400 W O_2 RIE did not happen at 600°C due to existence of enough open space to accommodate the gas at the interface. The temperature dependent void evolution showed that the size of the thermal voids increased with the increase in O_2 RIE power and time.

Figure 3.14 shows the quantitative analysis of the voids density of (a) SPAB specimen (B2) compared with the only RIE bonded specimen (C) annealed in nitrogen

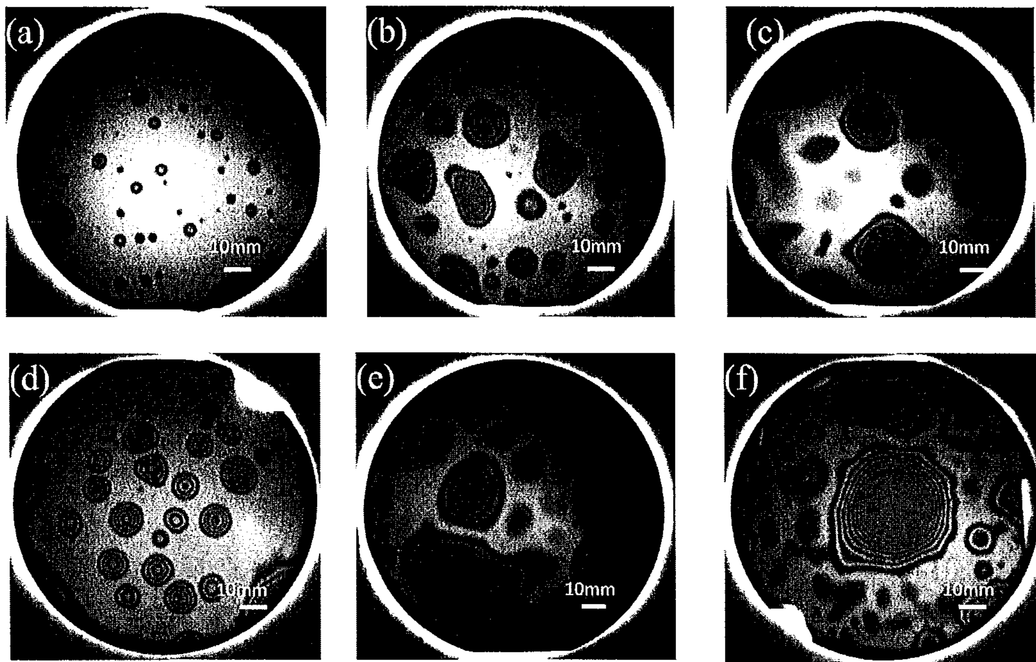

Figure 3.13: IR transmission images of all the specimens in groups A and B for transitions of voids nucleation of the SPAB interfaces at (a) 15 s, (b) 30 s, (c) 60 s in air for 4 hours at 600°C and (d) 200 W, (e) 300 W, (f) 400 W (800°C) in nitrogen ambient for 4 hours at 600°C.

gas, (b) O_2 RIE time dependent specimens (A1, A2, A3) annealed in air, and (c) O_2 RIE power dependent specimens (B1, B2, B3) annealed in nitrogen gas as a function of annealing temperatures. The void density was estimated from the IR images printed on scaled paper. A few percents of discrepancy may exist in the estimation of the void density due to human errors. From figure 3.14 (a), no significant change in the void density was observed between the O_2 RIE bonded and SPAB interfaces. On the other hand, the O_2 RIE time (Fig 3.14 b) and power (Fig. 3.14 c) dependent behavior of the void density in the SPAB interfaces showed that the plasma void density remained

constant up to 400°C, and the thermal void density suddenly increased for all the specimens at 600°C except for the specimen (B3) treated with an O_2 RIE power of 400 W

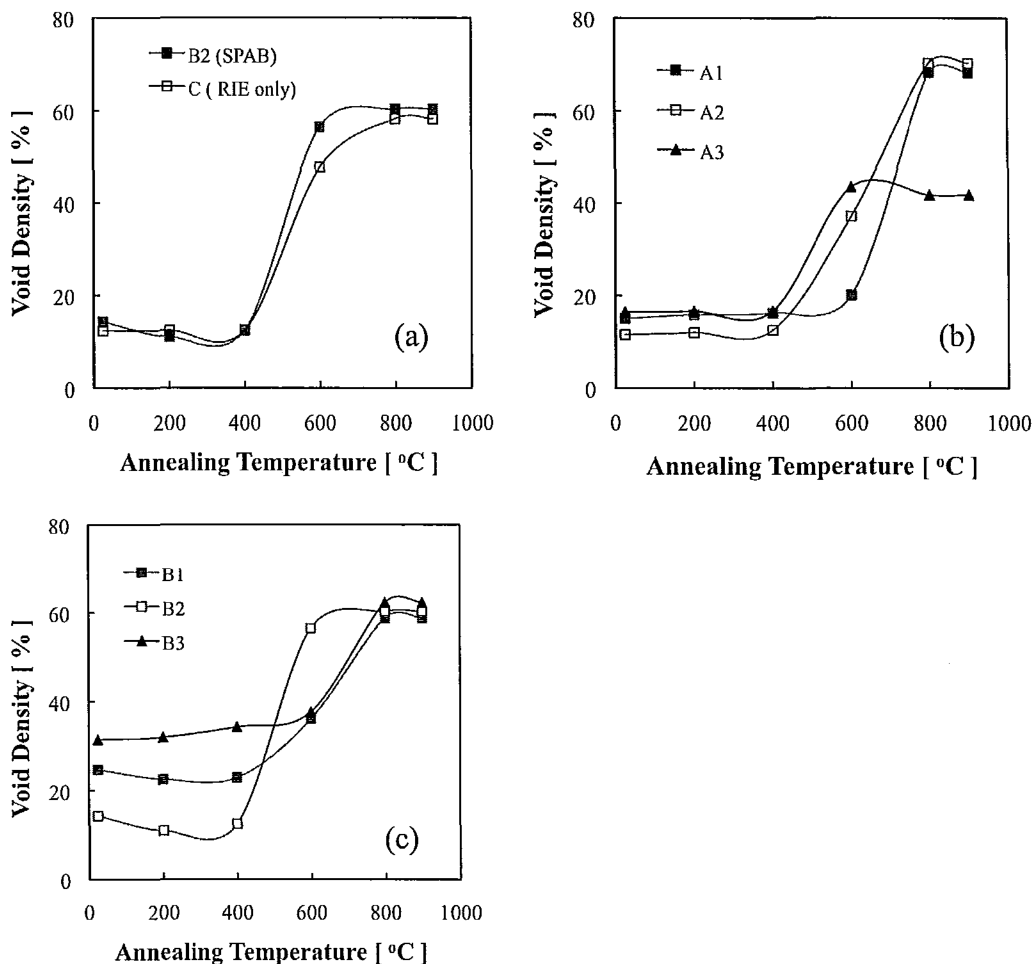

Figure 3.14: Void density in (a) SPAB specimen (B2) compared with that of in only RIE bonded specimen (C) annealed in nitrogen gas, (b) O_2 RIE time dependent specimens (A1, A2, A3) annealed in air, and (c) O_2 RIE power dependent specimens (B1, B2, B3) annealed in nitrogen gas for 4 h at each annealing step.

in nitrogen. For specimen B3, thermal void nucleation started at 800°C. Below 400°C, the void density for the specimens (Fig. 3.14 c) annealed in N_2 gas was higher than that

of the specimens (Fig. 3.14 b) annealed in air. Further researches are needed to clarify the role of annealing environment on the nucleation of voids. Above 600°C, the amount of thermal voids density for the specimen A2 was higher compared with that of the B1 specimen. This higher amount of void density was caused by higher activation time of N_2 radicals (30 s) for the specimen A2. The O_2 RIE plasma activation time for A1 and A2 were 15 and 30 s, respectively that were not sufficient to remove native oxides and surface particles from Si surface. This remaining native oxides and surface particles worked as precursor for the enlargement of the voids. On the other hand, the specimen A3 treated for 60 s had lower saturated void density at and above 600°C. This is attributed to the better removal of native oxides and surface particles due to the prolonged surface activation. In addition, it has been reported that plasma activation not only removes native oxides but also deposits an oxide layer on the treated surface [51]. This plasma induced oxide layer (which grows with activation time) helps absorb reaction byproduct at the interface and thus reduces void density [71].

3.4.2 Influence on Bonding Strength

Bonding strength is one of the important parameters for actual device fabrication process. For example, in smart-cut and back end thinning process, high bonding strength is required to withstand the chemical mechanical polishing (CMP). Figure 3.15 shows the bonding strength in SPAB as a function of annealing temperature. The bonding strength was measured 2-3 times for each specimen and the average values are shown with

appropriate error bars. For comparison, the bonding strength in hydrophilic bonding [7] is also shown in figure 3.15. The bonding strength in SPAB was as high as 15 MPa before annealing in contrast to 0.5 MPa in hydrophilic bonding (about 30 times higher in

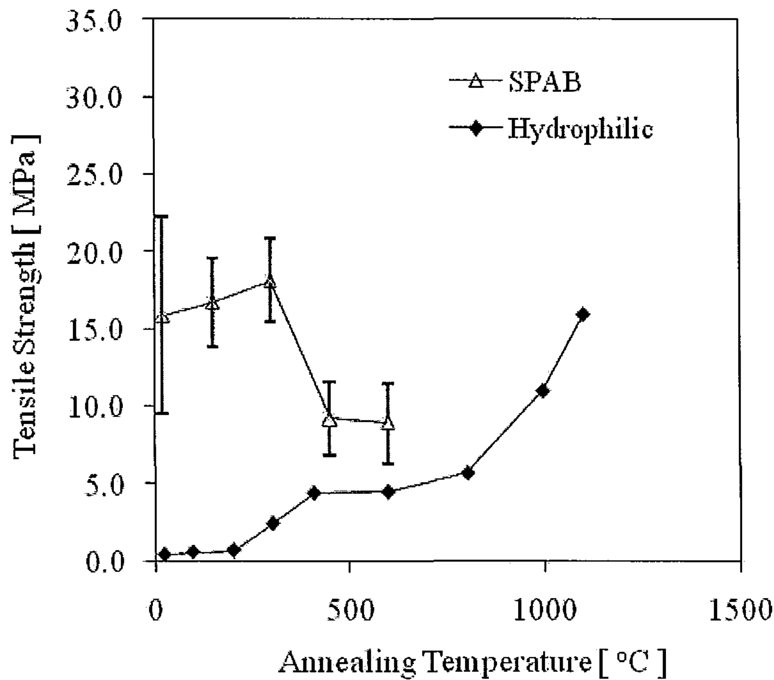

Figure 3.15: Bonding strength as a function of annealing temperature for SPAB and hydrophilic bonding.

SPAB). The bonding strength in hydrophilic bonding after annealing at 1100°C was equivalent to that in SPAB without annealing. The bonding strength in hydrophilic bonding increased at different slop after annealing. In contrast, the bonding strength in SPAB remarkably decreased after annealing over 300°C. In hydrophilic bonding, the bonding strength was increased with annealing temperature due to the shrinkage of chains of OH^- molecules [7]. The decrease in bonding strength in SPAB over 300°C can be attributed to .the generation of thermal induced voids at the interface. This high bonding

strength in SPAB without annealing (room temperature) is attributed to the covalent bonding between the atoms of the clean, smooth, hydrophilic and reactive surfaces.

3.4.3 Influence on Electrical Characteristics

The analysis of the electrical characteristics of the bonded interface upon post-bonding annealing allows us to further understand the defects and interface states and charges. It has been reported that the density of the interface states changes with the lateral positions of the bonded pair [67]. To avoid this issue, a single bonded pair with 10 × 10 mm^2 dimension was used for the *I-V* measurement at different temperatures instead of four different bonded pairs. The *I-V* characteristics of the bonded pair were measured at room temperature without annealing followed by annealed measurements at 200, 400, and 600°C, respectively. At each temperature step, the electrodes were removed before annealing. Each time an annealing process was completed, the specimen was cooled and the *I-V* curves were measured accordingly. The ramping rate was kept constant at 200°C per h, and the bonded pair was annealed for 4 hours in air at all three temperature steps. For the sequential activation, the wafer surfaces were processed by a 200 W O_2 RIE plasma for 60 s at 100 Pa, and then they were subsequently processed by 2000 W MW N_2 radicals for 30 s at 100 Pa. Figure 3.16 (a) shows the *I-V* characteristics of the sequentially plasma activated *p*-Si/*p*-Si bonded interface before and after annealing at 200, 400, and 600°C for 4 hours in air. The *I-V* measurements were repeated three times and the average values are given in figure 3.16 (a). The measurement errors

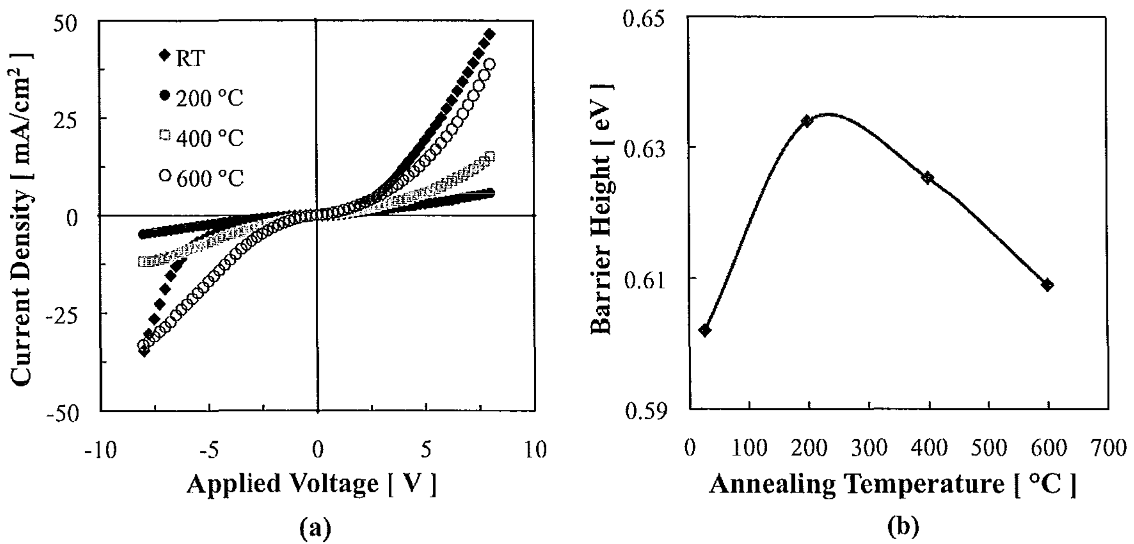

Figure 3.16: (a) Current-voltage characteristics, and (b) barrier height of sequentially plasma activated *p*-Si/*p*-Si bonded interface at RT and after annealing at 200, 400, and 600°C for 4 hours in air.

associated with this experiment were ± 10%. The barrier height shown in figure 3.16 (b) at the bonded interface was estimated using equation 3.2. The *I-V* characteristics show that the current density remarkably reduces after annealing at 200°C. The subsequent annealing steps at 400 and 600°C enhance the current density. The interfacial behavior can be explained with the discrepant behavior of charges and trap densities at different temperatures. As previously mentioned, the plasma induced charges as well as the OH^-groups and the incomplete nitridation reactions between nitrogen plasma and Si, can be attributed to the highest current density without annealing. This incomplete nitridation acts as trapping centers.

Annealing at 200°C, we observed that some of the OH^-groups diffuse from the interface, expand into the bulk Si, and increase traps at the interface. The increased traps

reduce the interface current density, resulting in increased barrier height at 200°C. Further annealing at 400°C and 600°C, the OH^- desorbed from the bulk Si, which decreased the barrier height [72]. The barrier height estimation in figure 3.16 (b) is somewhat higher than the actual value due to the contact resistance between silver paste and Si. However, for this comparative study, this additional contribution can be ignored. It is worth mentioning that since nitrogen atoms are not accelerated by DC bias, they cannot penetrate Si lattice and act as dopant. On the other hand, oxygen atoms are accelerated by DC bias and hence can reside in a shallow surface layer (1~2 nm) and act as dopant [73].

3.4.4 Influence on Interface Morphology

The post-bonding annealing can change interface morphology and hence the bonding quality. To clarify the influence of annealing on the morphology of the bonded interface, high resolution transmission electron microscopy (HRTEM) of the bonded specimens was performed. Four 2×2 mm^2 specimens were used. The first specimen did not go through any annealing steps. The three remaining specimens were each heated at an annealing temperature of 200°C, followed by the two remaining specimens at 400°C and the last remaining at 600°C. At all three temperatures the specimens were annealed for 4 hours in air with a ramping rate of 200°C per hour. With each point of temperature increase, one new specimen was removed for observation. For the sequential activation, the wafer surfaces were processed using the parameters utilized for the experiments as shown in figure 3.16. Figure 3.17 shows the HRTEM images of *p*-Si/*p*-Si sequential

plasma activated bonded interfaces. The HRTEM images show the presence of an intermediate amorphous layer at the bonded interface. The specimen which did not undergo annealing has an interface amorphous layer thickness of ~4.8 nm. The HRTEM images show that the amorphous layer thickness remains constant at ~4.8 nm after annealing at 200 and 400°C. However, the specimen annealed at 600°C has an amorphous layer of ~13 nm thickness. While the amorphous layer remained constant up to 400°C, the interface current density significantly reduced (figure 3.16 a) after annealing at 200°C. Then the current density increased at 400°C and 600°C, but the amorphous layers thickness increased at 600°C. Therefore, no relationship was found between the amorphous layer thickness and the *I-V* characteristics (figure 3.16 a) of the bonded interfaces at different annealing temperatures.

The abrupt change in the amorphous layer at 600°C can be correlated with the abrupt change in void density after annealing at 600°C as shown in figure 3.14. At 600°C, two concurrent phenomena: (1) The breaking of SiO_xN_y and (2) viscous flow of H_2 gas generated from adsorbed H_2O from bulk Si, are responsible for the sudden increase in amorphous layer thickness. The following two reactions occur at 600°C that increase the interfacial Si oxide layers:

$$SiO_xN_y \rightarrow SiO_x + N_y \quad (3.3)$$

$$Si + 2H_2O \rightarrow SiO_2 + 2H_2 \quad (3.4)$$

These reactions produce nitrogen and hydrogen gases at the bonded interface. Since the amount of nitrogen was reported to be negligible on the sequentially treated

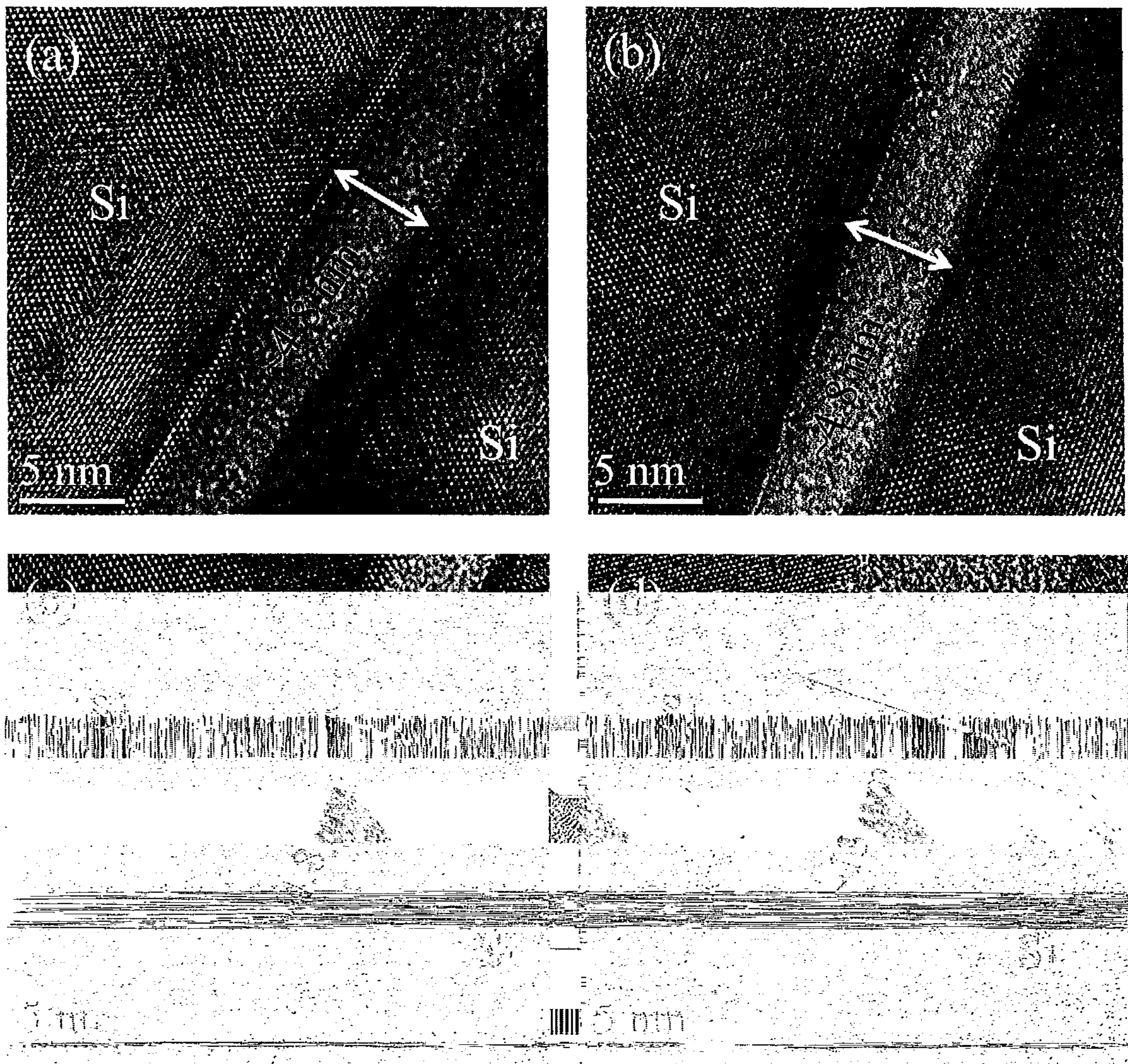

Figure 3.17: High resolution TEM images of the bonded Si/Si interfaces (a) before annealing, and after annealing at (b) 200°C, (c) 400°C, and (d) 600°C

surface [40], viscous flow of hydrogen gas may have had a dominant role on the increased thickness of the amorphous layers. Additional contribution to the increased thickness can be attributed to the diffusion of oxygen interstitials from bulk Si to the interface because of high concentration of oxygen interstitials in CZ Si [74].

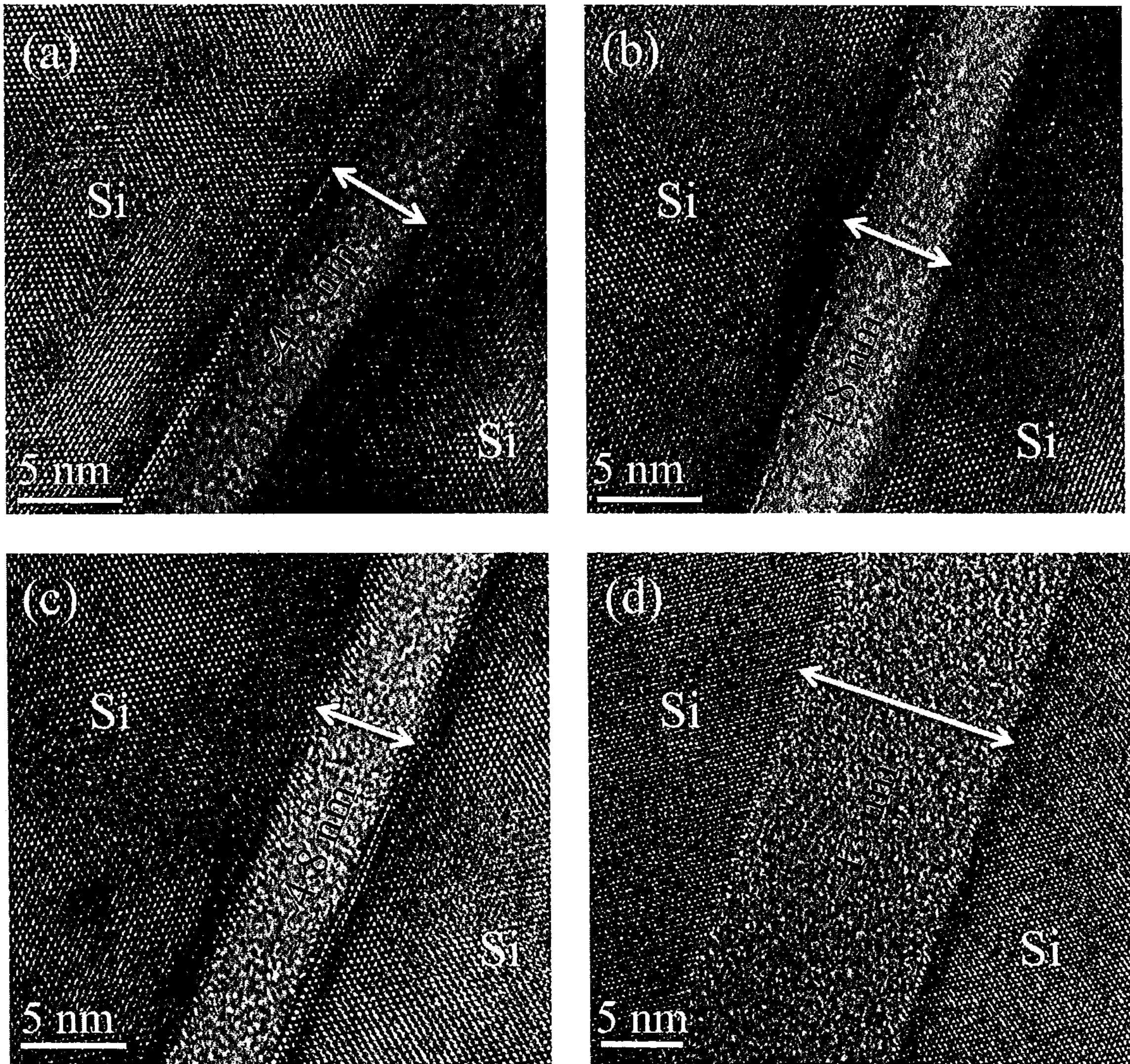

Figure 3.17: High resolution TEM images of bonded Si/Si interfaces (a) before annealing, and after annealing at (b) 200°C, (c) 400°C, and (d) 600°C.

surface [40], viscous flow of hydrogen gas may have had a dominant role on the increased thickness of the amorphous layers. Additional contribution to the increased thickness can be attributed to the diffusion of oxygen interstitials from bulk Si to the interface because of high concentration of oxygen interstitials in CZ Si [74].

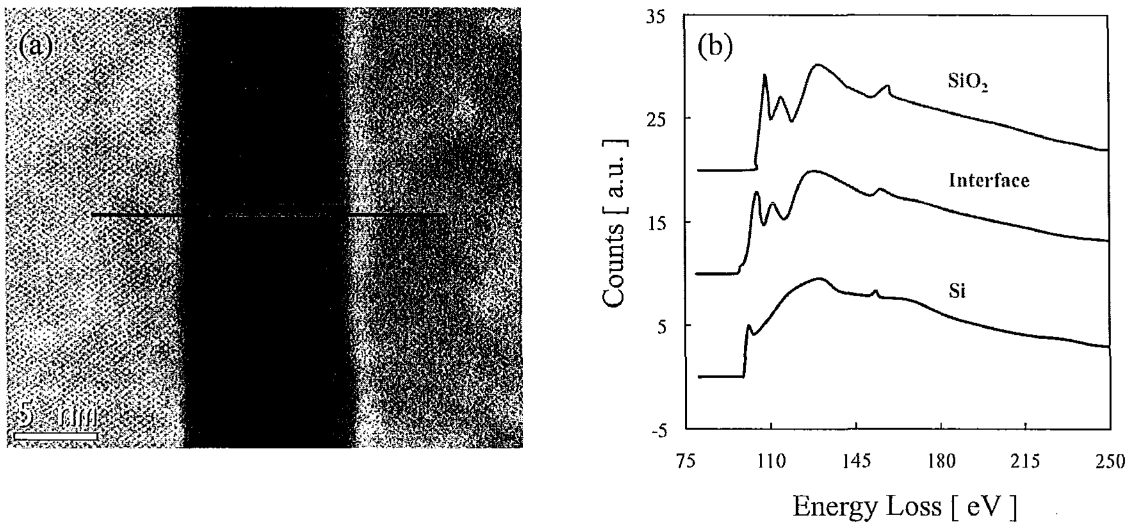

Figure 3.18: (a) Scanning TEM image of the bonded interface of specimen shown in Fig.3.17 (d), (b) compositional distribution along the red line shown in (a) by the EELS analysis.

The Si/Si bonded interface has been investigated through electron energy loss spectroscopy (EELS) to determine the nano-interface compositions after annealing. Figure 3.18 shows (a) Scanning TEM image of the bonded interface of the specimen shown in figure 3.17 (d), (b) the EELS for detection of elements at the interface. The STEM image shows ~13 nm interfacial amorphous layer at the bonded interface. From the EELS spectra, no nitrogen was detected at the bonded interface. Both the Si-$L_{2,3}$ edges at 125-175 eV and the O-K edges at 540-560 eV were observed at amorphous oxide layer of the interface. A further analysis of the Si-$L_{2,3}$ of amorphous oxide compared with Si and SiO_2 provides the characteristic behavior of amorphous layer at the interface. Fig 3.18 (b) shows the Si-$L_{2,3}$ edges from the interfacial amorphous oxide layer compared with the standard Si and SiO_2. The Si-$L_{2,3}$ edges from the amorphous layer

were identical to those of the standard SiO_2 at the bonded interface. This implies SiO_2 is present at the interface. This is because of the annealing of specimen at 200, 400 and 600°C for 4 hours at each step in air.

3.5 SPAB Mechanism

Based on the results presented in this chapter, the SPAB mechanism is summarized and schematically presented in figure 3.19. The SPAB mechanism is fundamentally similar to the hydrophilic bonding mechanism. In the hydrophilic bonding, at room temperature the wafer surfaces adhere each other through weak hydrogen bonds of hydroxyl groups (OH^-). High temperature annealing is required to remove interfacial water; which results in strong covalent bond. In contrast, in case of SPAB, strong covalent bonding was achieved at room temperature after storage for 24 hours. This strong bonding in SPAB at room temperature can be explained as follows. The O_2 RIE plasma activation removes native oxides, contaminations and leads to a smooth surface, as observed in section 3.2. This results in a large number of OH^- groups on the activated surfaces (see figure 3.19 c). The presence of OH^- groups resulted in low contact angle after O_2 RIE activation. Further, as shown in figure 3.6, the physical sputtering of RIE plasma creates a porous surface. Subsequent activation with MW N_2 radicals (i.e. sequentially activated surface) enhanced the surface reactivity through replacing the OH^- groups by oxinitride (O_xN_y) sites (see figure 3.19 d). The enhanced reactivity of the sequentially activated surface was proved by the lowest contact angle, as shown in figure 3.2.

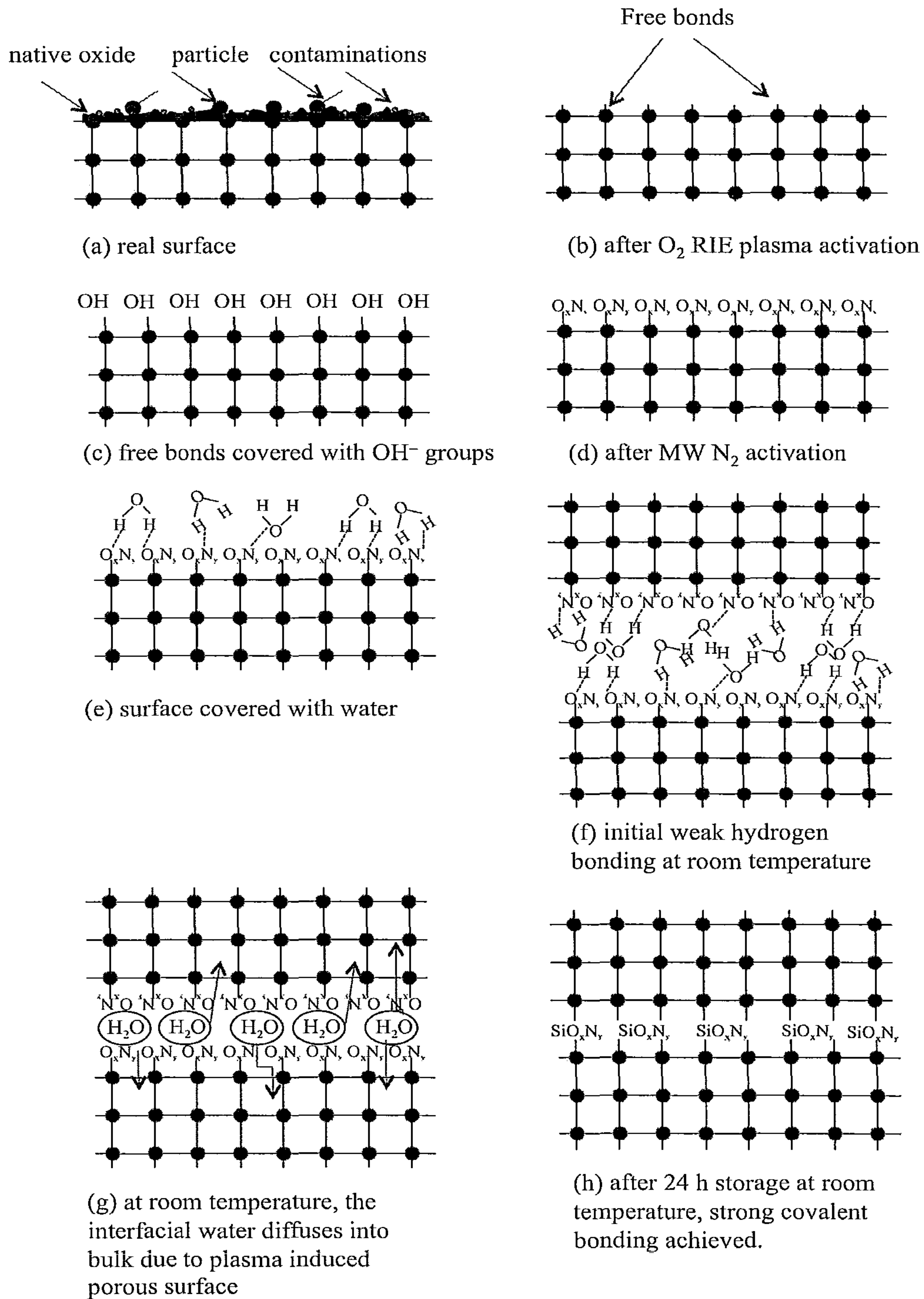

Figure 3.19: Schematic of SPAB mechanism.

In clean room ambient, the highly reactive surface (terminated by O_xN_y) is further terminated by OH^- groups and acts as precursor to initiate the spontaneous bonding, as shown in figure 3.19 (e). When two activated surfaces are brought into contact, they adhere each other through weak hydrogen bonds between OH^- groups, as shown in figure 3.19 (f). The condensation of OH^- results in water (H_2O) at the interface, as shown in figure 3.19 (g). Due to the surface porosity, after storage for 24 hours at room temperature, the interfacial water diffuses into the bulk silicon. The role of reactivity induced by N_2 radicals was to make faster reactions between the mated surfaces for strong bonding. Hence, strong covalent Si-O_xN_y-Si bonding was achieved at room temperature.

However, when the bonded pair underwent post-bonding annealing steps, the nucleation of voids started. The interfacial voids were due to the plasma induced defects (Fig. 3.7) and hydrogen gas produced due to the reaction at the bonded interface (Equation 3.4). The interfacial reaction at high annealing temperature resulted thick amorphous Si oxide layer, as shown in figure 3.17 (d). Due to the nucleation of interfacial voids and brittle oxide layer at the interface the bonding strength decreased after high temperature annealing, as shown in figure 3.15.

3.6 Applications of SPAB for Nano-integration

Recently, wafer bonding has gained remarkable attention to create nano-scale devices such as carbon nanotube (CNT) based MEMS (i.e., microcoolers) [75] and ordered templates to realize self-assembly of molecules, nanowires (NWs) or quantum

dots (QDs) [2, 76]. To bond these nanostructures (i.e., CNTs, NWs, QDs), current wafer bonding methods utilize wet chemical processes, high temperature annealing steps and external forces to achieve high bonding strength. A number of researches on integration of nanostructures have been reported using diffusion, adhesive, chemical, ultrasonic vibrational force, thermo-compression and electro-thermal bonding methods [59, 75-80]. The issues in these methods are: (1) high bonding temperature and external force may not be suitable for bonding nanostructures due to their delicate nature, (2) adhesive bonding results in reduced current transport and reduced mechanical stability (3) the wet chemical processes before bonding may not be applicable towards bonding chemically sensitive delicate materials with substrates that contain metals.

In contrast to the prevalent bonding, the SPAB allows spontaneous bonding at room temperature and it does not require any wet chemicals, intermediate adhesives, external forces and annealing steps to achieve high bonding strength. At room temperature, the bonding strength in SPAB is higher than the bonding strength in hydrophilic bonding after annealing at 1000°C. Hence, the SPAB can open up opportunities for room temperature spontaneous integration of nanostructures on the wafer scale.

3.7 Conclusions

A sequentially plasma activated bonding (SPAB) of Si wafers has been studied to facilitate the spontaneous bonding required for nanostructure integration on wafer scale.

The O_2 RIE and MW N_2 offered the highest hydrophilic surface and lowest surface roughness and hence this combination was chosen for sequential plasma activation.

The IR transmission images showed plasma induced voids at the bonded interface. The O_2 RIE plasma power had dominant role on the formation of voids compared to O_2 RIE time. The plasma induced defect sites such as nano-pores and craters were responsible for nucleation of voids for the specimens treated relatively with high power (i.e., 400 W).

The *I-V* measurements showed that the current transport across the nano-bonded interface could be improved by decreasing the O_2 RIE activation time. A strong relationship between bonding strength and voids was observed after annealing. The nucleation of thermal voids for all specimens regardless of O_2 RIE time and power occurred at 600°C except for the specimen treated with 400 W O_2 RIE which was appeared at 800°C. Thermal void nucleation was preferentially at the plasma induced defect sites. The abrupt increase in void density at 600°C is correlated to the abrupt increase in interfacial amorphous layer thickness at 600°C.

HRTEM images confirmed the nanometer scale bonding of the mating wafers with an interface amorphous layer thickness of ~4.8 nm. EELS results revealed the presence of SiO_2 at the nano-bonded interface. Our investigations show that the proper choice of plasma parameters can offer highly reactive surface associated with improved current transport which is required for spontaneous integration of nanostructures at room temperature.

CHAPTER 4. SEQUENTIALLY PLASMA ACTIVATED BONDING OF SILICON/GLASS AND GERMANIUM/GLASS

4.1 Introduction

Currently micro/nano-scale lab-on-a-chip devices have found potential applications in separation, sensing and analysis of chemicals (i.e. hydrocarbons, pesticides) and biological species (i.e., DNA, enzymes) [81-83]. One of the requirements for these devices is to utilize excellent physical and chemical properties of silicon and glass. Silicon (Si) is the most researched material in electronics, which has high thermal conductivity (~130 $Wm^{-1}{}^{\circ}C^{-1}$) with improved on-chip heat dissipation and high mechanical stability [84]. On the other hand, glass is a low cost material with high biocompatibility, optical transparency, hydrophilicity, good dielectric property in a wide range of frequency, high chemical and heat resistivity, and high mechanical strength [85-86]. Combining Si with glass through direct bonding allows creating a Si platform required for the integration of future micro/nano-scale electronic or optical sensing devices. One of the approaches for combining Si with glass is the anodic bonding technique. However, the high temperature and high voltage requirement of anodic bonding hinders its applicability for the integration of micro/nano-scale delicate structures. Hence, a low temperature bonding technique for Si/glass is needed for the integration of micro/nano-scale sensing devices.

On the other hand, germanium (Ge) has recently drawn considerable interest for the fabrication of photodetectors for long distance optical communication systems

operating in 1300–1550 nm wavelength range. This is because of large absorption coefficient of Ge at near infrared frequency range [87]. Furthermore, being a group-IV material, Ge is compatible with Si technology and offers high carrier mobility. Therefore, Ge on Si (GOS) technology is competing with III-V on Si technology [88]. The GOS technology has been implemented for photodetector fabrication by epitaxial growth of Ge on Si at temperatures in the range of 700-900°C [89]. However, epitaxial growth of Ge is not preferable because of the incompatibility of high temperature with microelectronics. Also, this process is expensive and creates high concentration of misfit and threading dislocations in the deposited Ge film due to large lattice mismatch (4.2 %) between Ge and Si. The dislocations create large dark current and reduce the detector sensitivity [90-92]. In contrast, wafer direct bonding and layer splitting process allow thin film of Ge with bulk properties on a variety of substrates. For example, direct bonding of Ge and glass can find application in fiber optic receivers, where Ge photodetector bonds with fiber end. Recently, Ge-on-glass photodetector has been realized using wafer bonding [88, 93]. However, moderate temperature (~400°C), chemical, and prolonged annealing (~8 hours) were needed. In fact, prolonged annealing at moderate temperature creates thermal stress, interfacial voids and hence not preferable for delicate structures and materials with large difference in thermal expansion coefficient [94]. Chemical sensitivity of Ge hinders the applicability of these bonding techniques [95]. Furthermore, prolonged annealing reduces device throughput. Hence, a low temperature, chemical free, void-free, robust and fast bonding technique for improved bonding quality of Ge and glass is needed for practical applications.

In order to reduce the high temperature requirements and to achieve void-free and strong bonding, a novel bonding technique has been developed by modifying sequentially plasma activated bonding (SPAB). The SPAB has been combined with anodic bonding process and termed as hybrid plasma bonding (HPB) technique. This chapter discusses the results of Si/glass and Ge/glass bonding using HPB technique. The surface properties of Si, Ge and glass have been revealed using drop shape analysis and atomic force microscopy (AFM). The bonding qualities have been explored using tensile pulling test and IR observation. Further, the nano-bonded interface has been investigated using high resolution transmission electron microscopy (HRTEM) and energy dispersive X-ray analysis (EDX).

Note that the results presented in this chapter are published in two peer reviewed journal articles [96-97]. The published results are a part of the motivations of the thesis, and hence the write-up sequence of the thesis is different from the published articles. For both articles in Ref: [96], [97], I was primarily responsible for literature search, for writing the manuscript and partially for the experiments.

4.2 Hybrid Plasma Bonding (HPB) of Silicon/Glass

Anodic bonding has been used for bonding Si and glass since mid ’60s. In anodic bonding, the Si and glass wafers are contacted and then heated in the temperature range of ~800°C. At these temperatures, the alkaline cations in glass become mobile. Then an external DC voltage of 400-1000 V is applied keeping glass at the cathode and Si at the anode side (see Fig. 2.2) [98]. The mobile cations transport toward the cathode and a

depletion layer is formed near the bonded interface. The transportation of cations results in a high electrostatic force which pulls Si and glass wafers. Thus a high bonding strength is achieved due to high electrostatic force. Major challenges in the Si/glass bonding using the anodic bonding techniques are the presence of voids and low bonding strength of the interface at low temperature (i.e., 150-200°C). These challenges pose difficulty to fabricate Si and glass based micro/nano-scale devices with micro/nano-fluidic channels for single cell analysis, and separation of DNA molecules [99].

Recently, anodic bonding requires heating the contacted wafers at moderate temperature (300~500°C) in order to achieve void-free interface with high bonding strength (i.e., 10-15 MPa) [98]. In addition to the temperature requirement, other approaches, such as adhesive, laser, induction heating, fusion, glass frit, eutectic and solder bonding require chemicals, and high external force for bonding [100-101]. The high temperature hinders bonding of nanostructures (i.e., nanofluidic channel with integrated nanotubes [102]) due to wafer bow caused by thermal stress [103] and poses design constraints for devices with aluminum or copper integrated circuits [98]. In order to reduce the bonding temperature with improvement of bonding strength, Si and glass surfaces were treated with plasma followed by anodic bonding. The bonding strength achieved through this process was very low (~3.3 MPa) [104], which need to be improved for practical applications. Furthermore, surface roughness controls bonding strength as well as nucleates voids at the interface [105]. Rough surface reduces optical transparence of glass (i.e., at extreme ultraviolet wavelength) [106], which is crucial in applications where transmitted and reflected optical signals are used for the analysis of

chemical or biological species [83, 107]. These issues have not been yet addressed for the realization of the micro/nano-scale lab-on-a-chip devices.

To address the above mentioned issues caused by high temperature bonding, the HPB technique is developed. The HPB consists of three steps: (1) surface activation by O_2 RIE plasma, followed by (2) surface activation by MW N_2 radicals and (3) then contacting the activated wafers followed by anodic bonding in air. The anodic bonding temperature was kept as low as 200°C with 1 KV applied voltage. The surface properties of Si and glass have been investigated to understand the role of plasma activation on these surfaces.

4.2.1 Surface Hydrophilicity

To understand the role of plasma activation in the hybrid plasma bonding, the contact angles of water on plasma treated Si and glass surfaces were studied. Figure 4.1 shows the contact angle of both Si and glass wafers before and after plasma activation. Contact angles of both Si and glass surfaces significantly decreased after RIE and sequential plasma activation. This implies an increase in surface energy and improvement in bonding strength. When these reactive surfaces were brought in contact, the OH^- groups of the mating surfaces attracted each other forming a high bonding strength at room temperature. Plasma activation not only changes surface hydrophilicity, but also changes surface roughness of Si and glass. The influence of plasma activation on Si and glass surface roughness has been investigated and discussed in the following section.

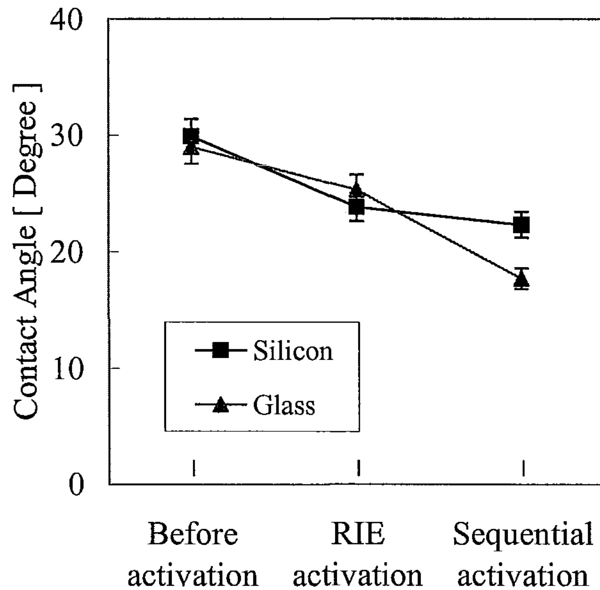

Figure 4.1: Contact angle of water on Si and glass before and after plasma activation.

4.2.2 Surface Roughness

Surface roughness of Si and glass was measured before and after plasma activation to explore the role of plasma activation. Figure 4.2 shows AFM images of Si (a) before plasma activation, (b) after RIE plasma activation (c) after sequential plasma activation and AFM images of glass (d) before plasma activation, (e) after RIE plasma activation (f) after sequential plasma activation. The RMS value of surface roughness was measured at three locations for each specimen and the average value was estimated. Table 4.1 shows the RMS surface roughness of Si and glass before and after plasma activation.

Table: 4.1 The RMS surface roughnesses of Si and glass wafers.

Specimen	RMS Surface Roughness [nm]		
	Before plasma activation	After RIE plasma activation	After sequential plasma activation
Si	0.15	0.19	0.18
Glass	0.52	0.48	0.46

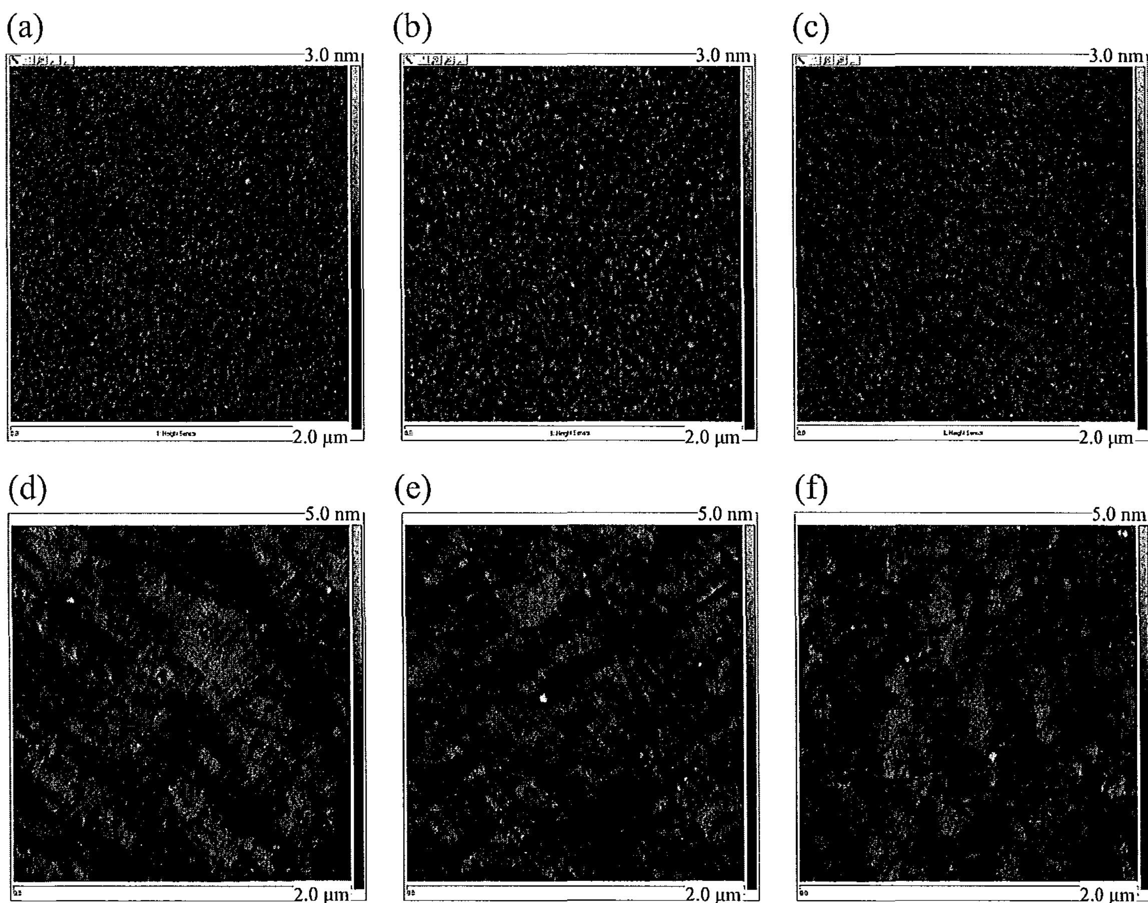

Figure 4.2: AFM images of Si (a) before plasma activation, (b) after RIE activation, (c) after sequential plasma activation, and of glass (d) before plasma activation, (e) after RIE activation, and (f) after sequential plasma activation.

Although the surface roughness of Si was increased after plasma activation, the surface roughness of glass was reduced. This is presumably due to the discrepant etching behavior of Si and glass by the RIE plasma. In contrast to Si, Pyrex glass surface had ~3-5 nm size pits. This surface defects were similar to the plasma induced defects such as nanopores and craters on Si surface which induced voids at the Si/Si interface (Fig. 3.6).

To compare the results of HPB with those of anodic bonding, the Si and glass wafers were first anodically bonded at different bonding temperatures. The following section discusses the role of anodic bonding temperature on the interfacial voids.

4.2.3 Role of Anodic Bonding Temperature on Interfacial Voids

To understand the role of anodic bonding temperature on interfacial voids, Si and glass wafers were first bonded using anodic bonding technique. Figure 4.3 shows the optical images of Si/glass specimens anodically bonded at (a) 100 (b) 150 and (c) 200°C. Voids were present at the interfaces regardless of the bonding temperature. The sizes of the voids were decreased, but their numbers were increased with the increase in the bonding temperature. The anodic bonding currents were zero, 0.01 and 2.9 mA at 100, 150 and 200°C, respectively with an applied voltage of 1 KV. At 200°C, the current was decreased to zero after 10 min. These results indicate that the anodic bonding alone does not provide void-free interface at low temperature. This result is in agreement with the behavior of temperature dependent voids at the Si/glass interface [108]. In general, the interfacial voids are attributed to (i) hydrogen gas (H_2) from Si oxidation reaction ($Si+H_2O \rightarrow SiO_2+H_2$) by the adsorbed water (H_2O) on Si and glass wafers or by the water

produced at the interface when silanol bonds (Si-OH) are condensed to form siloxane bonds (Si-O-Si), (ii) the entrapment of gas between various bond fronts [98], (iii) the presence of particles at the interface and (iv) surface defects. The decrease in voids' size

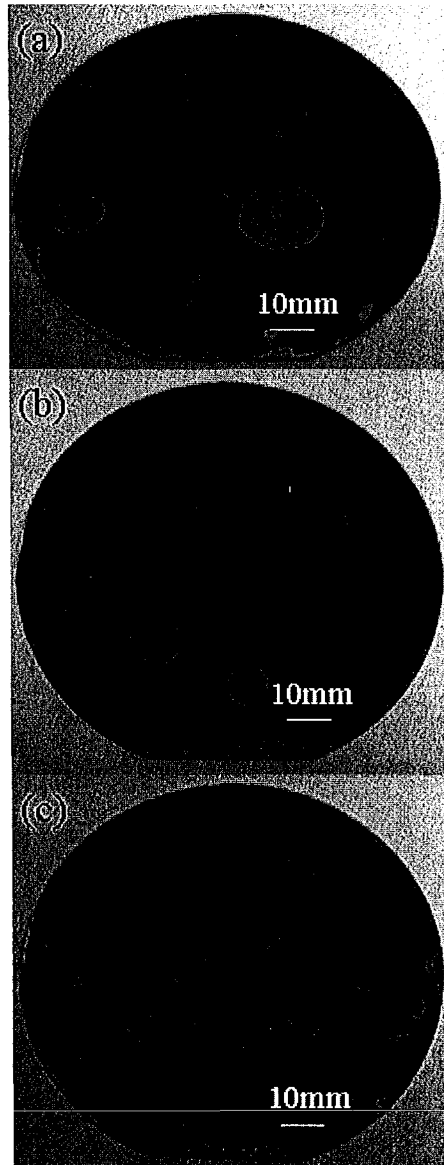

Figure 4.3 Optical images of Si/glass wafers anodically bonded at temperature of (a) 100, (b) 150, and (c) 200°C.

and density, as shown in figure 4.3 (c), is due to the presence of carbon contaminants, and H_2 caused by temperature enhanced oxidation reaction. The reduction of the voids' size with the increase in the temperature is presumably due to the lack of coalescence of voids caused by increase in bonding strength. To achieve void-free interface of Si/glass at low temperature, different combinations between plasma activation and anodic bonding have been systematically investigated. The following section discusses the role of plasma activation on interfacial voids.

4.2.4 Role of Plasma Activation on Interfacial Voids

Figure 4.4 shows the optical images of the Si/glass wafers bonded using (a) (i) the RIE plasma activated bonding at room temperature, (ii) the RIE plasma activated anodic bonding at 200°C, (b) (i) the SPAB at room temperature, (ii) the sequential plasma activation followed by anodic bonding (i.e., HPB) at 200°C. A comparison of the bonded interfaces in the RIE plasma activated bonding (Fig. 4.4 a (i)), and RIE plasma activated anodic bonding at 200°C (Fig. 4.4 a (ii)) showed fewer voids at latter interface. After the SPAB (Fig. 4.4 b (i)), the voids were reduced compared to that of the RIE plasma activated bonding. However, void-free interface was achieved at 200°C in the HPB, as shown in figure 4.4 b (ii). Note that the anodic voltage was 1 KV. To compare the bonding strengths of hybrid plasma bonded Si/glass interface with those of anodic bonding, RIE plasma activated bonding, RIE plasma activated anodic bonding and SPAB methods, tensile pulling test was performed for all type of specimens. The following section discusses the role of plasma activation on the bonding strength.

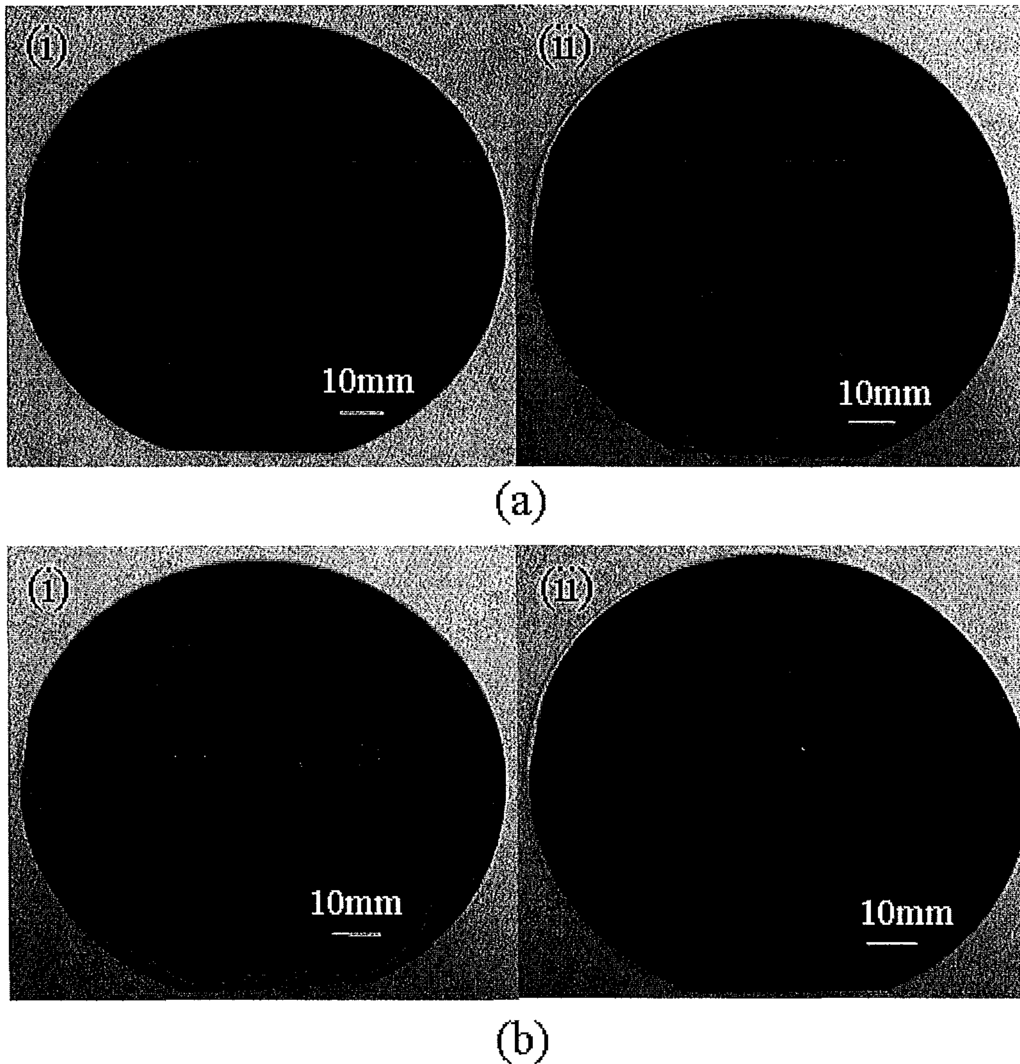

Figure 4.4: Optical images of Si/glass wafers bonded through (a) (i) RIE plasma activated bonding, (ii) RIE plasma activated anodic bonding at 200°C, and (b) (i) SPAB, (ii) HPB at 200°C.

4.2.5 Role of Plasma Activation on Bonding Strength

Figure 4.5 shows a comparative study of bonding strength of Si/glass in the HPB, anodic bonding, RIE plasma activated bonding, RIE plasma activated anodic bonding,

and SPAB methods. In the RIE plasma activated bonding and SPAB methods, the specimens were not heated. In the anodic bonding, while the bonding strength was significantly improved from 100 to 150°C, it was not considerably changed from 150 to 200°C. The bonding strength of the specimens in the RIE plasma activated anodic bonding at 200°C was 15 MPa, which was higher than that of the anodic bonding. On the

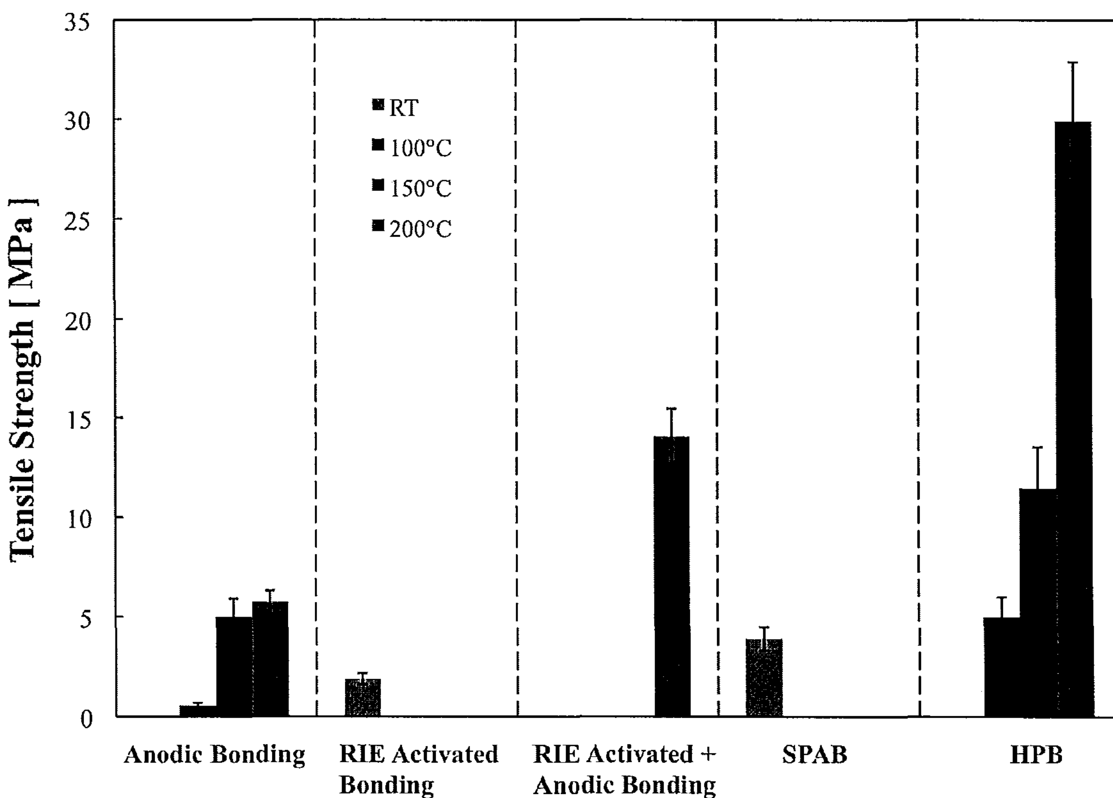

Figure 4.5: Bonding strength as a function of different bonding conditions.

other hand, the bonding strength in the HPB at 100°C was comparable to that of the anodic bonding at 150 and 200°C, but lower than that of the RIE plasma activated anodic bonding at 200°C. With the increase of the bonding temperature in the HPB, the bonding strength was drastically increased. This increase in the bonding strength is in contrast to

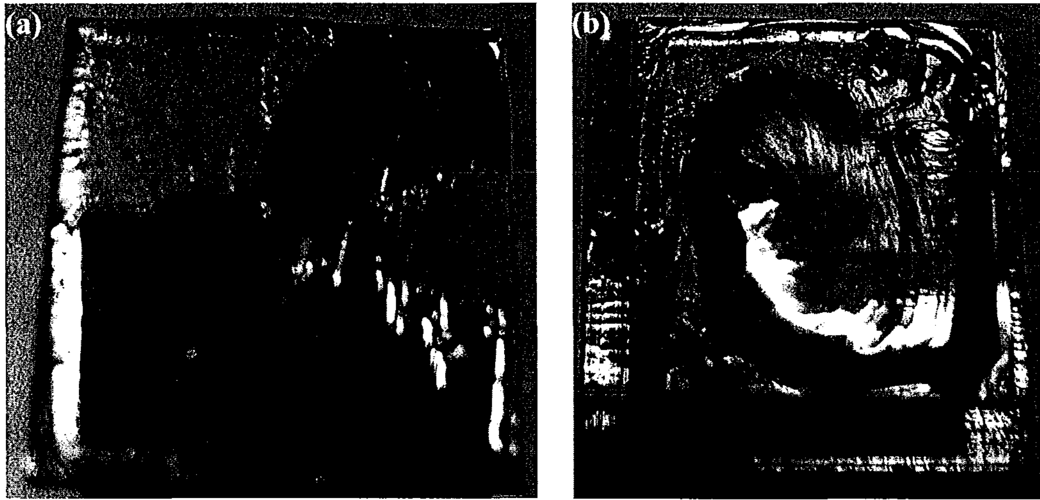

Figure 4.6: Fracture images of Si/glass bonded using (a) the RIE plasma activated anodic bonding at 200°C, and (b) the HPB at 200°C.

the increase of the bonding strength in the anodic bonding after plasma activation [104]. At 200°C, the bonding strength in the HPB was 30 MPa, which was highest compared to that of the anodic, and individual plasma activated bonding and the RIE plasma activated anodic bonding. To the best of my knowledge, the bonding strength was the highest (~30 MPa) number compared to the reported values achieved through the conventional anodic bonding. Figure 4.6 shows the fracture images of Si/glass bonded using (a) the RIE plasma activated anodic bonding at 200°C and (b) the HPB at 200°C. The fracture images showed a partial fracture and a complete fracture of glass in the RIE plasma activated anodic bonding and the HPB, respectively, as shown in figure 4.6 (a) and 4.6 (b). It also showed that the fractured glass was remained on Si wafer after the bonding test. On the other hand, in case of anodic bonding, no bulk fracture was observed (not shown). Anodic bonding at all three temperatures (i.e., 100, 150 and 200°C) resulted in debonding

from the interface after tensile pulling test. In case of HPB, bulk fracture of glass occurred at 150°C (not shown) and 200°C (4.6 b) because of high bonding strength of the interface. This indicates that the bonding temperature has strong impact on the bonding strength. In this study, the impact of the applied voltage on the bonding strength was not investigated. This is because the earlier simulation results showed that the bonding temperature has higher impact over applied voltage on electrostatic force in the anodic bonding. While an increase in applied voltage from 0.2 KV to 1 KV increased the electrostatic force by thirty times, an increase in bonding temperature from 300 to 400°C increased the electrostatic force by six orders [109]. This implies strong bonding is due to temperature dependent high electrostatic force. In contrast to the high bonding strength (10-15 MPa) in the temperature range of 400-500°C [98], a higher bonding strength (~30 MPa) was achieved in this study at a reduced temperature (i.e., 200°C). The applied voltage was 1 KV. This enhancement of the bonding strength is caused by the sequential plasma activation. The sequential plasma activation removes contaminations and native oxides that resulted in high electrostatic force under the application of voltage at low temperature. Further, the high bonding strength in HPB is attributed to the increase in hydrophilicity of Si and glass surface, as observed in figure 4.1.

To find insights into the HPB mechanism, the interface of the hybrid plasma bonded Si/glass has been investigated using HRTEM. The results are discussed in the following section.

4.2.6 Nanointerface Observation

In order to observe the combined effect of plasma activation and electrostatic force, the hybrid plasma bonded Si/glass interface has been investigated using a HRTEM.

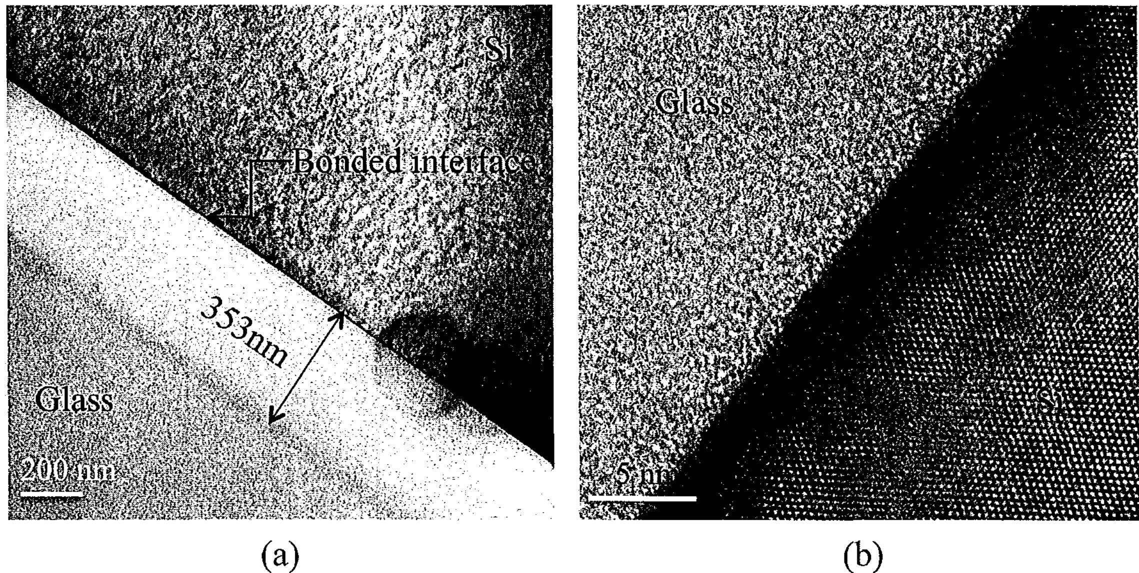

Figure 4.7: HRTEM images with (a) low, and (b) high magnifications. A ~353 nm thick bright depletion layer in the glass and an indistinct dark edge of Si near the interface are observed.

Figure 4.7 shows the HRTEM images of hybrid plasma bonded (200°C) Si/glass interface with (a) low magnification, (b) high magnification. From the low magnification image, a ~353 nm thick layer was identified in glass. This layer was brighter than bulk glass and Si, which was identified as sodium depletion region using EDX spectra [110]. The higher brightness was attributed to the smaller mean atomic number of the depletion region compared to that of the bulk glass, caused by the migration of sodium and potassium cations [98]. The width of this sodium depletion layer in this study was less

compared to the most published results [110]. This can be attributed to the low bonding temperature (200°C) in this study compared to ~350-500°C used in previous studies [98]. The dark band at the edge of depletion region in glass was due to the accumulation of less mobile potassium cations [98]. From the high magnification image (Fig. 4.7 b), a ~2-3 nm thick indistinct layer was observed at the bonded interface. This is because of the charging of the glass wafer during TEM specimen preparation.

4.3 HPB of Germanium/Glass

Hybrid plasma bonding has been used for bonding Ge/glass at low temperature. High bonding strength at low temperature is essential in Ge layer transfer to glass through back end thinning process. While Ge bonding with Si and glass has been implemented in the fabrication of optical devices [88, 91-93] and it has tremendous need in emerging applications such as optical biosensing system [83], low temperature bonding of Ge and glass has not been yet investigated. The following subsection reports a chemical free, strong and fast HPB of Ge and glass at 200°C. The plasma parameters used here are same as those used for bonding of Si and glass.

4.3.1 Surface Hydrophilicity

To explore the hydrophilicity of Ge and glass, contact angle measurements were performed after each step of plasma activation. Table 4.2 shows the contact angle of a

drop of DI water droplet (10μL) on Ge surface before plasma activation, after the RIE plasma activation and after the sequential plasma activation.

Table: 4.2 The contact angle of DI water on Ge wafer.

Specimen	Contact angle [°]		
	Before plasma activation	After RIE plasma activation	After sequential plasma activation
Ge	68	<2	<2

Before activation the water contact angle on Ge surface was 68 degrees and it was below the detection limit of the instrument after the RIE and the sequential plasma activation. This result is consistent with recently reported results on Ge surface hydrophilicity [41]. On the other hand, the contact angle on glass surface was 29, 25.3 and 17.7 degrees before activation, after the RIE plasma activation and after the sequential plasma activation, respectively as shown in figure 4.1. From the Young's equation in equilibrium [41], the lower the contact angle, the higher the surface energy. This implies that the high bonding strength of Ge/glass interface in hybrid plasma bonding is due to the increase in surface energy after sequentially plasma activation.

4.3.2 Surface Roughness

The characteristic behavior of surface controls the bonding performance. For practical applications such as optical biosensing system [111], the surface roughness of glass needs to be kept as low as possible in order to achieve high reflectivity of the

surface [112]. Figure 4.8 shows the AFM images of Ge before plasma activation, after RIE plasma activation and after sequential plasma activation. Table 4.3 summarizes the RMS surface roughness of Ge.

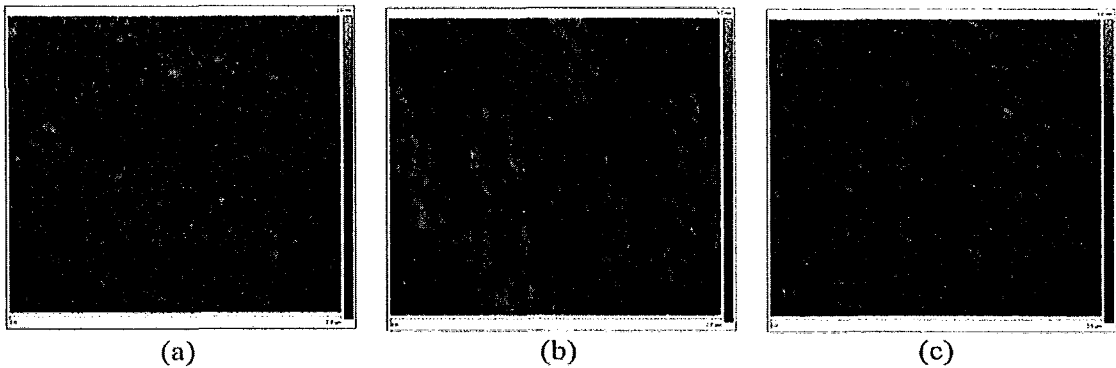

(a) (b) (c)

Figure 4.8: AFM images of Ge (a) before plasma activation, (b) after RIE plasma activation, and (c) after sequential plasma activation

Table: 4.3: The RMS surface roughness of Ge wafer.

Specimen	RMS Surface Roughness [nm]		
	Before plasma activation	After RIE plasma activation	After sequential plasma activation
Ge	0.24	0.25	0.20

The surface roughness of glass (Table: 4.1) was relatively higher than that of Ge (Table: 4.3). This was due to the sensitivity discrepancy between the alkaline and silicate elements of glass to CMP. This results in nanodefects on glass surface in contrast to Si [113]. These nanodefects cause voids at the bonded interface. In fact, the surface roughness of the sequential plasma activated Ge and glass was remarkably reduced. The decrease in surface roughness improved the surface energy and the bonding strength

[110, 114]. This reduction is attributed to removing surface contaminations, and native oxides. The improved surface roughness indicates that the HPB of Ge/glass can be used for the level-free detection of biological species using optical biosensing system.

4.3.3 Interfacial Voids and Bonding Strength

Figure 4.9 (a) shows the optical image of the hybrid plasma bonded Ge/glass wafers. Although voids were observed at the interface in the SPAB before the anodic treatment, a nearly void-free interface was achieved in the HPB. This is attributed to absorption of voids in the interfacial oxide. The voids remained were presumably due to the presence of particle on the activated surface and entrapment of air at the interface due to plasma induced surface defects. The bonding strength of Ge/glass interface was investigated by tensile pulling test. The bonding strength was 9.1 MPa. Figure 4.9 (b) shows the fracture image of bonded Ge/glass interface after tensile pulling test. The images show a partial fracture in the bulk of Ge. It also shows that the fractured Ge was remained on glass wafer after the tensile pulling test. The bulk fracture of Ge is due to the higher strength of the bonded interface than Ge bulk. This high bonding strength of the interface is due to the highly hydrophilic and smooth surfaces of Ge and glass after sequential activation as shown in Table 4.2 and Table 4.3. The lower bonding strength of the Ge/glass (~9.1 MPa) interface than the Si/glass (~30 MPa) interface is attributed to the lower bulk fracture strength of Ge than Si and glass. This high bonding strength (robust) is very important in layer transfer process. In layer transfer process, either the

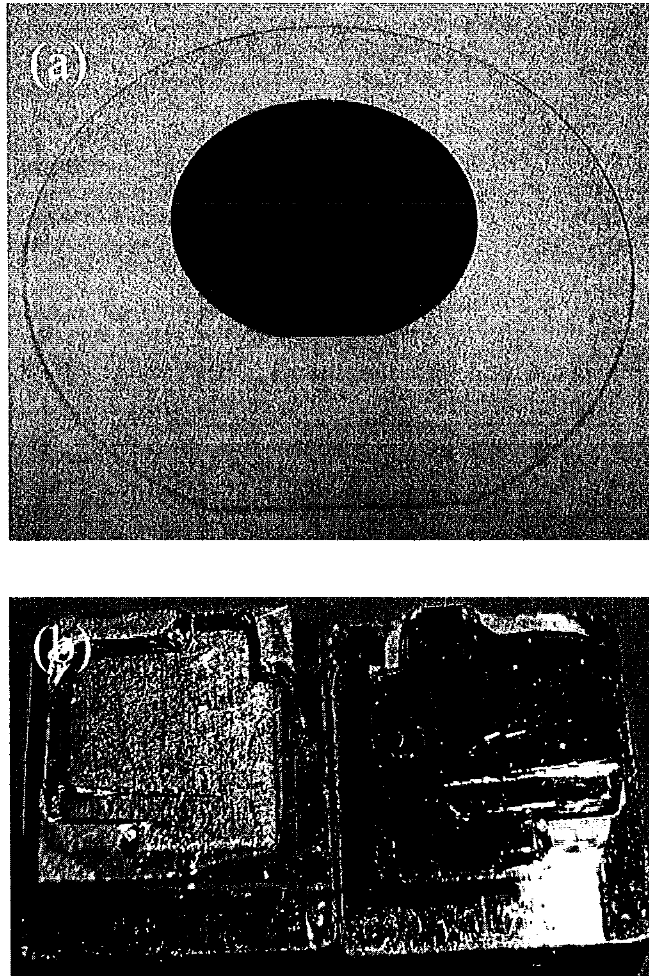

Figure 4.9: (a) Optical image of hybrid plasma bonded Ge/glass, and (b) fracture image of bonded Ge/glass after tensile pulling test.

bulk or the exfoliated surfaces (which are rough) from the bonded wafers need to be thin down or smoothening by CMP. This CMP process requires strong bonding strength of the interface. It has been reported that after surface smoothening process the performance of photo detector significantly improved [93].

4.3.4 Nanointerface Observation

Figure 4.10 shows a HRTEM image of bonded Ge/glass interface. A ~1 μm thick brighter layer than Ge and glass was observed in glass near the bonded interface. This layer looks similar to a depletion layer at the interface of Si and Pyrex glass observed in

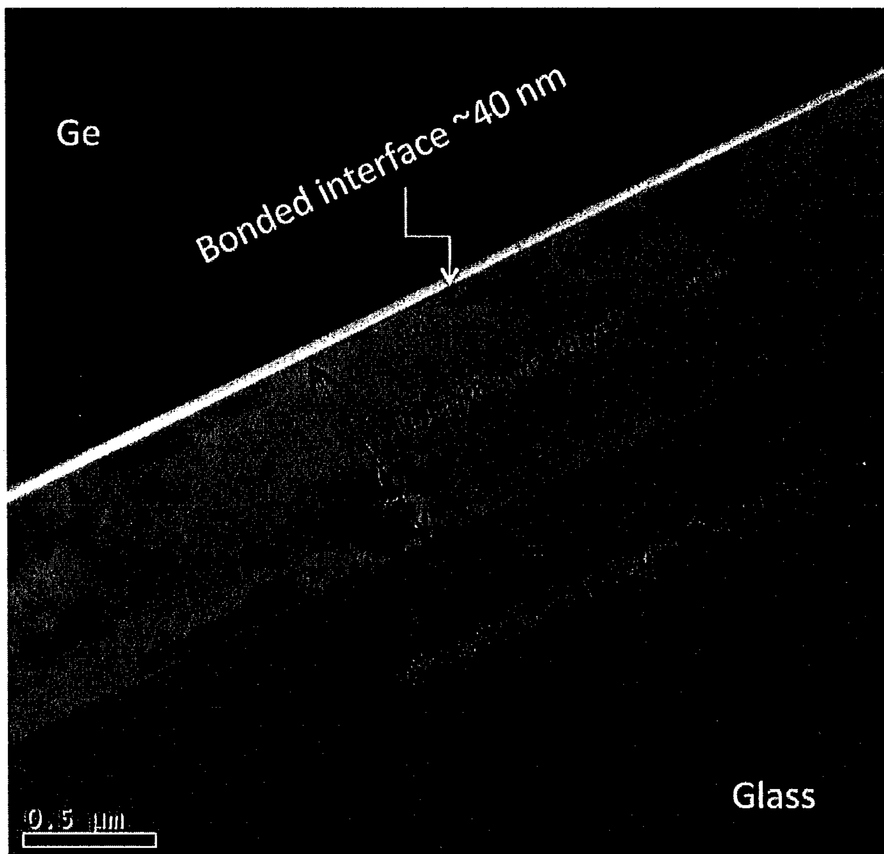

Figure 4.10: High resolution TEM image of hybrid plasma bonded Ge/glass interface.

anodic bonding [98] and hybrid bonding (Fig. 4.7). The observed depletion layer in glass was due to the migration of alkaline cations from the region near the interface toward the bulk. In addition to the depletion layer, a ~250 nm thick second layer in glass was

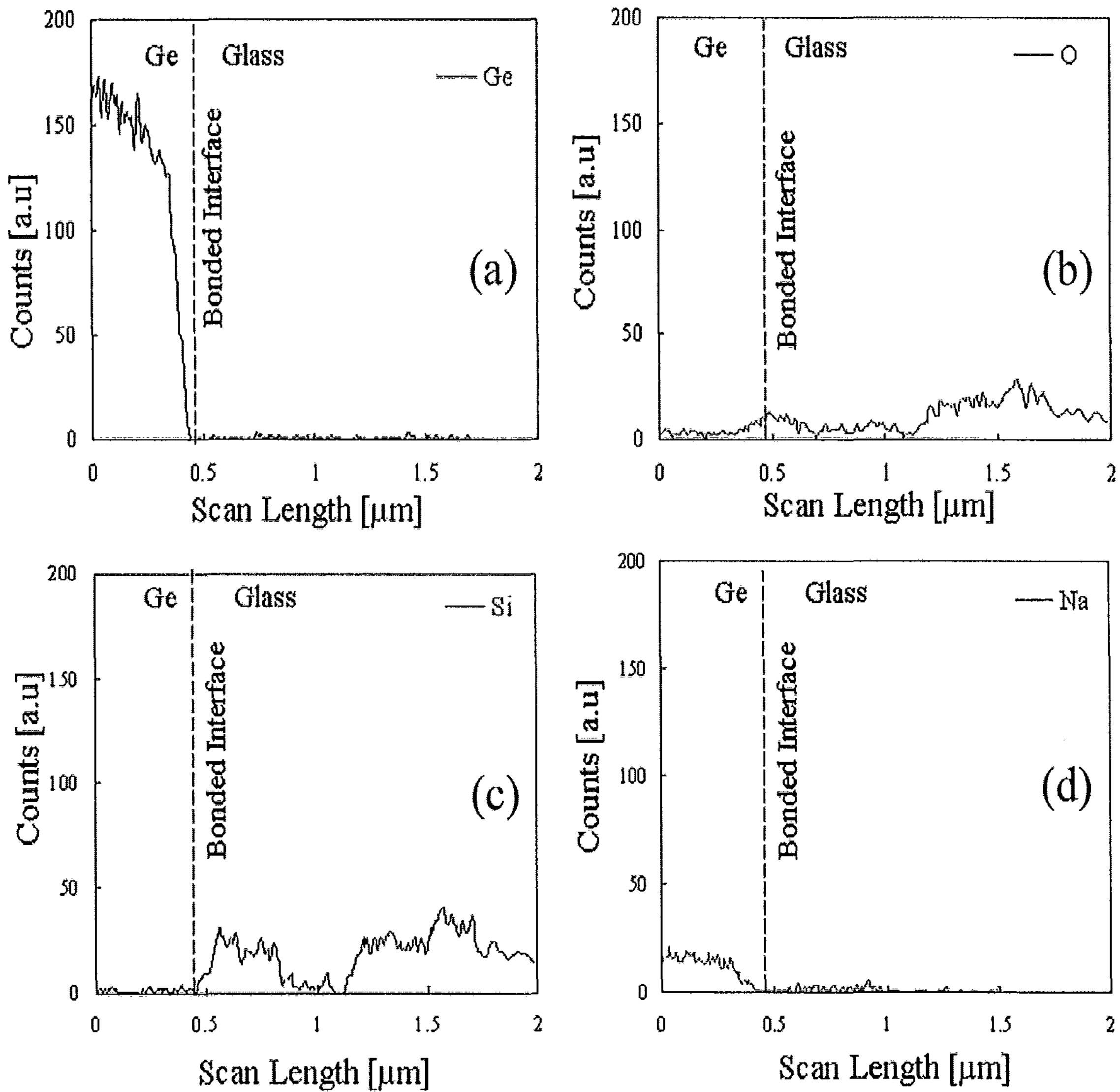

Figure 4.11: EDX spectra of (a) Ge, (b) O, (c) Si, and (d) Na at and around the interface of hybrid plasma bonded Ge/glass.

observed near the Ge/glass interface. This is due to accumulation of alkaline cations [115]. Furthermore, a thin layer (~40 nm) relatively with higher contrast than that of the depletion layer was observed at the bonded interface. This brighter layer is thicker than that of the Si/Si interface in the SPAB as shown in figure 3.17. The interfacial Si/Si layer

in the SPAB has been identified as SiO_2 as shown in figure 3.18. Similarly, Ge oxide can be formed at the Ge/glass interface in the SPAB. Further enlargement of the Ge oxide can be attributed to the anodic bonding after the SPAB (i.e., HPB). Therefore, the increased thickness of the brighter layer is due to the growth of Ge oxide caused by the opposite migration of oxygen anions to that of the alkaline cations.

To investigate the elemental distribution at the interface, EDX analysis was performed. Figure 4.11 shows the distribution of Ge and three main elements of Pyrex glass at and around the interface. From figure 4.11 (a), it is evident that Ge did not diffuse into glass. From figure 4.11 (b) and 4.11 (c), the presence of oxygen and Si was evident in the depletion layer. A considerable amount of oxygen was observed across the interface, which enlarged the thickness of Ge oxide. Diffusion of oxygen in Ge was not found at the interface. Figure 4.11 (d) shows the presence of sodium (Na) in Ge, the reason for this is not clear from this study. Na and boron (B) were not observed in the depletion region. In fact, EDX does not detect B [111]. Therefore the HRTEM results could not be explained using the EDX study. Further study is required to explore the findings.

4.4 HPB Mechanism

In order to explain the hybrid plasma bonding mechanism, it is indispensable to review the current understanding in the anodic bonding [98, 108, 115, 116]. In the anodic bonding, when two polished wafers of Si and glass are brought into intimate contact under DC high voltage (400-1000 V) and moderate temperature (300-500°C), the

electrostatic force between the materials' surfaces provides permanent chemical bond. The Si and glass are biased by placing on anode and cathode, respectively. The Pyrex glass, being used for anodic bonding, has a coefficient of thermal expansion (CTE) close to Si (i.e., CTE mismatch $<1\times10^{-6}$ K^{-1}) and contains a high concentration of alkali oxides (i.e., Na_2O and K_2O). The glass is negatively charged with respect to the Si. The glass polarizes under these conditions. The alkali oxides dissociate into cations (mainly Na^+) and anions (O^-), then the alkali cations are transported toward cathode resulting in a depletion region in glass, and a thin region of oxygen-rich layer is formed in the vicinity of the interface. Almost the entire applied voltage is shared between the depleted region and the small gap between the two wafers due to surface roughness, and thus the applied voltage generates a high electrostatic force which pulls the mating wafers into intimate contact. Si and glass are thus bonded together due to the high electrostatic force at high voltage and high temperature. The electrostatic force at these conditions is not sufficient to remove the interfacial voids due to the presence of carbon contaminations and native oxides at the interface.

As previously mentioned, the applied voltage has lower impact on the electrostatic force than the temperature. At 100°C a low electrostatic force resulted in a low bonding strength (0.56 MPa) (Fig. 4.5), which allowed the interface gas to move around and coalesce to form larger voids as shown in figure 4.3 (a). With increase in temperature, bonding strength improved significantly (5 MPa at 150°C and 5.73 MPa at 200°C as in Fig. 4.5). With increase in temperature, more cations (mainly Na^+) dissociate from Na_2O and K_2O in glass and their mobility increases, resulting in a higher bonding

current [117]. The higher current at higher temperature leads to higher electrostatic force and hence improved bonding strength as shown in figure 4.5. The higher bonding strength at higher temperature (i.e., ~200°C) hindered the movement of entrapped gas at the interface, resulting in smaller void size with increased density, as seen in figure.4.3 (c).

On the other hand, void-free interface with high bonding strength was achieved in the HPB. The improvement of the bonding quality in the HPB is due to the surface cleaning, and the augmentation of surface energy of the Si, Ge and glass using sequential plasma activation prior to the anodic bonding. In the sequential plasma activation, first, the RIE plasma removes native oxides and surface contaminations, as well as induces an oxide layer (~3-6 nm) on the treated surface [37, 56]. Then, the MW N_2 radicals produce reactive surface with high surface energy. The significant enhancement of the surface energy of Ge, Si and glass in the sequential plasma activation was confirmed by using the contact angle measurements. In the HPB, the SPAB was performed prior to the anodic bonding. Since the SPAB was done in the air outside the plasma activation chamber, the sequentially treated surfaces were highly hydrophilic due to adsorption of OH^- molecules from the ambient air. This implies that the number of OH^- molecules for bonding remarkably increased after sequential plasma activation resulting in strong adhesion between the surfaces. These OH^- groups form initial contact through hydrogen bonds and finally produce permanent covalent siloxane bonds (Si-O-Si).

When the SPAB specimen went through the anodic bonding, a thick layer of depleted alkaline ions was generated due to the flow of alkali cations toward the cathode,

and a thin oxide layer was formed due to reverse flow of oxide anions near the interface. This diffused oxide anions enhance further oxidation of Si under the applied voltage and temperature [118]. The oxidation of Si produces amorphous SiO_2 layer across the interface [115], which absorbs the reaction by-product (H_2) and thus eliminates interfacial voids [56]. Similarly, Ge-oxide at the interface is attributed to the void-free strong bonding of Ge/glass. In addition, the smooth clean surfaces after the sequential plasma activation were responsible for the void-free interface. Therefore, the void-free high bonding strength in the HPB is due to the combined effect of the adhesion between the large numbers of OH^- groups on the activated surfaces and the electrostatic force produced during the anodic bonding.

4.6 Conclusions

A novel hybrid plasma bonding (HPB) process has been developed to achieve void-free strong bonding of Si/glass and Ge/glass interface at 200°C. Void-free strong bonded interface cannot be realized at low temperature individually in the anodic and plasma activated bonding due to the presence of surface contaminations and absence of bonding sites (OH^-), and the absence of electrostatic force, respectively. In HPB, the electrostatic force in anodic bonding has been combined with high adhesion between the hydrophilic surfaces resulted from the sequential plasma activation to achieve void-free strong bonded interface at low temperature. The improved quality of the bonded interface in the HPB is due to increased bonding sites and smooth surfaces. The highly reactive and clean surfaces enhance the mobility of alkaline cations toward the cathode and the

reverse transportation of anions. This transportation resulted in a ~353 nm thick alkaline depletion layer in the glass and enlarged the amorphous SiO_2 across the interface. In case of Ge/glass, three layers were observed: a ~1 micrometer thick depletion layer, a ~250 nm thick alkaline accumulation layer and a ~40 nm thick Ge oxide layer across the interface. The HPB bonding mechanism is attributed to the reactions of OH^- molecules between the highly reactive surfaces in the SPAB, and the opposite migration of cations and anions during anodic treatment. This method can be used in optical biosensing system for level-free detection of biological species due to improved surface roughness of glass and robust interface of Si/glass and Ge/glass.

CHAPTER 5. CONCLUSIONS AND FUTURE WORKS

5.1 Conclusions

A room temperature, chemical free and spontaneous bonding technique is highly desirable for the integration of emerging micro/nano-scale devices. Hence, a room temperature and chemical free direct bonding technique called sequentially plasma activated bonding (SPAB) has been studied here. Sequential plasma activation provides clean, smooth, hydrophilic and reactive surfaces, which is required for spontaneous integration of nanoscale devices.

The contact angle and surface roughness measurements show that surface activation using O_2 RIE plasma followed by MW N_2 radicals is the best combination to achieve highly hydrophilic, smooth and reactive surfaces. Whilst a low power and short duration plasma activation cleans and smoothens the surfaces, high power and prolonged plasma creates defect sites such as nanopores and craters. These porous surfaces allow easy removal of interfacial wafers and achieve strong covalent bonding at room temperature. The current transport across the nano-bonded interface is controlled by the plasma activation parameters. The interfacial voids are nucleated at the surface defects. Annealing of bonded pair leads to nucleation of voids preferentially at the plasma induced defect sites. The abrupt increase in void density after annealing at 600°C is correlated with the abrupt increase in interfacial amorphous layer thickness at 600°C. A strong relationship between bonding strength and voids is observed after annealing.

The SPAB has been modified in which the SPAB undergoes through the anodic bonding process and termed as hybrid plasma bonding system (HPB). The HPB offers void-free strong bonding of silicon/glass and Ge/glass at 200°C. The bonding strength of the silicon/glass and germanium/glass in the HPB at 200°C is 30 MPa and 9.1 MPa, respectively. The sequential plasma activation significantly improves hydrophilicity and smoothens the Ge and glass surfaces. Therefore, in HPB, the electrostatic force in anodic bonding combines with high adhesion between the hydrophilic and smooth surfaces resulted from the sequential plasma activation. The improved quality of the bonded interface in the HPB is due to increased bonding sites and smooth surfaces. The chemical free strong bonding of Si/Si in the SPAB at room temperature and void-free strong bonding of silicon/glass and germanium/glass in HPB at low temperature will open up opportunities for spontaneous integration of nanodevices on the wafer scale.

5.2 Future Works

The future work focuses on the followings:

1. Finding the optimum plasma parameters (power, pressure and activation time) to achieve void-free strong bonding of Si/Si at room temperature.
2. Investigation on the cause of the reduction in bonding strength in SPAB at high annealing temperature to expand the applicability of SPAB for harsh annealing environments. In addition, it is indispensable to understand the reliability of SPAB in chemicals, high pressure, and high vacuum environments.

3. Investigation on the anomalous surface morphology of silicon wafers after Ar RIE plasma activation.
4. Fabrication of nanostructures using advanced lithography techniques and integration of the nanostructures using the SPAB and HPB on the wafer scale.
5. Implementation of HPB for Si/glass based lab-on-a-chip devices. For this application, the bonded interface will expose to fluids. Therefore, the reliability of HPB needs to be investigated in such environments.
6. Implementation of HPB for Germanium/glass based photodetectors.

REFERENCES

[1] A. Plossl, G. Krauter, "Wafer direct bonding: tailoring adhesion between brittle materials", *Materials Sci. & Eng.*, R25 (1999) 1.

[2] S. H. Christiansen, R. Singh and U. Gösele, "Wafer direct bonding: from advanced substrate engineering to future applications in micro/nanoelectronics", *Proc. IEEE,* 94 (2006) 2060.

[3] G. Galilei, Discorsi E Dimostrazioni Matematiche. Mailand: Le Opere, 2 (1938) 1638, reprinted.

[4] L. Rayleigh, "A study of glass surfaces in optical contact", *Proc. Phys. Soc. A*, 156 (1936) 326.

[5] G. Wallis, D. I. Pomerantz, "Field assisted glass-metal sealing", *J. Appl. Phys.*, 40 (1969) 3946

[6] G. Wallis, "Field assisted glass sealing," *Electrocomp. Sci. Technol.*, 2 (1975) 45.

[7] M. Shimbo, K. Furukawa, K. Fukuda, K. Tanzawa, "Silicon-to-silicon direct bonding method", *J. Appl. Phys.*, 60 (1986) 2987.

[8] G. Antypas, J. Edgecomb, "Glass-sealed GaAs-AlGaAs transmission photocathode", *Appl. Phys. Lett.*, 26 (1974) 371.

[9] Z. L. Liau, D. Mull, "Wafer fusion: a novel technique for optoelectronic device fabrication and monolithic integration", *Appl. Phys. Lett.*, 56 (1990) 737.

[10] J. B. Lasky, "Waver bonding for silicon-on-insulator technologies", *Appl. Phys. Lett.*, 48 (1986) 78.

[11] K. Petersen, P. W. Barth, J. Poydock, J. Brown, J. Mallon, J. Bryzek, "Silicon fusion bonding for pressure sensors", *Proc. IEEE Sol. Stat. Sens. Actuators Workshop*, (1988) 144.

[12] J. Haisma, "Direct bonding in patent literature", *Philips J. Res.*, 49 (1995) 165.

[13] Q.-Y. Tong, U. Gösele, "Semiconductor wafer bonding: Science and Technology", *New York: Wiley,* 1999.

[14] S. S. Lyer, A. J. Auberton-Herve, "Silicon wafer bonding technology for VLSI and MEMS Applications*", London, INSPEC,* 2002.

[15] J. B. McKitterick, A. Caviglia, G. Goetz, W. P. Maszara, "Total dose radiation hardness of bonded SOI wafers", *Proc. IEEE Int. SOI Confer.,* (1992) 38.

[16] C.-T. Ko, K.-N. Chen, "Wafer-level bonding/stacking technology for 3D integration", *Microelectronics Reliability*, 50 (2010) 481.

[17] T. Suni, K. Henttinen, A. Lipsanen, J. Dekker, H. Luoto, M. Kulawski, "Wafer scale packaging of MEMS by using plasma-activated wafer bonding", *J. Electrochem. Soc.*, 153 (2006) G78.

[18] M. Esashi, "Wafer level packaging of MEMS", *J. Micromech. Microeng.*, 18 (2008) 073001.

[19] N. Miki, "Wafer bonding techniques for MEMS", *Sensor Lett.,* 3 (2005) 1.

[20] J. Haisma, B. Spearings, U. Biermann, A. van Gorkum, "Diversity and feasibility of direct bonding: A survey of a dedicated optical technology", *Appl. Opt.*, 33 (1994) 1154.

[21] H. Kawanami, "Heteroepitaxial technologies of III-V on Si", *Sol. Ener. Mater. Sol. Cells,* 66 (2001) 479.

[22] L. D. Cioccio, E. Jalaguier, F. Letertre, "III-V layer transfer onto silicon and applications", *Physi. Stat. Sol. A*, 202 (2005) 509.

[23] Y. Xiong, Y. Zhou, Z. H. Zhu, Y.-H, Lo, C. Ji, S. A. Basher, A. A. Allerman, T. Hargett, R. Sieg, K. D. Choquettee, "Oxide-defined GaAs vertical-cavity surface-emitting lasers on Si substrates", *IEEE Photon. Technol. Lett.*, 12 (2000) 110.

[24] T. W. Ang, G. T. Reed, A. Vonsovici, A. G. R. Evans, P. R. Routley, M. R. Josey, "Effects of grating heights on highly efficient unibond SOI waveguide grating couplers", *IEEE Photonics Technol. Lett.*, 12 (2000) 59.

[25] T. Suni, "Direct wafer bonding for MEMS and microelectronics", *PhD Dissertation, VTT Technical Research Centre of Finland*, 2006.

[26] D. Pasquariello, K. Hjort, "Plasma-assisted InP-to-Si low temperature wafer bonding", *IEEE J. Select. Top. Quan. Electron.*, 8 (2002) 118.

[27] D. Pasquariello, "Plasma assisted low temperature semiconductor wafer bonding", *PhD Dissertation, Uppasala University*, 2001.

[28] P. Amirfeiz, S. Bengtsson, M. Bergh, E. Zanghellini, L. Borjesson, "Formation of silicon structures by plasma-activated wafer bonding", *J. Electrochem. Soc.*, 147 (2000) 2693.

[29] S. N. Farrens, J. R. Dekker, J. K. Smith, B. E. Roberds, "Chemical free room temperature wafer to wafer direct bonding", *J. Electrochem. Soc.*, 142 (1995) 3949.

[30] D. Pasquariello, M. Lindeberg, C. Hedlund, K. Hjort, "Surface energy as a function of self-bias voltage in oxygen plasma wafer bonding", *Sens. Actuators A*, 82 (2000) 239.

[31] H. Moriceau, F. Rieutord, C. Morales, S. Sartori, A. M. Charvet, "Semiconductor Wafer Bonding: Science, Technology and Applications VIII", *The Electrochem. Soc.,* (2005) 34.

[32] A. Weinert, P. Amirfeiz, S. Bengtsson, "Plasma assisted room temperature bonding for MST", *Sens. Actuators A,* 2978 (2001) 1.

[33] J. Arokiaraj, S. Tripathy, S. Vicknesh, S. J. Chua, "Si layer transfer to InP substrate using low-temperature wafer bonding", *Appl. Surf. Sci.,* 253 (2006) 1243.

[34] T. H. Kim, "Sequential activation process for wafer direct bonding at room temperature", *PhD Dissertation, The University of Tokyo*, 2004.

[35] T. H. Kim, M. M. R. Howlader, T. Itoh, T. Suga, "Room temperature Cu–Cu direct bonding using surface activated bonding method", *J. Vac. Sci. Tech. A,* 21 (2003) 449.

[36] M. M. R. Howlader, S. Suehara, H. Takagi, T. H. Kim, R. Maeda, T. Suga, "Room-temperature microfluidics packaging using sequential plasma activation process", *IEEE Trans. Adv. Packag.,* 29 (2006) 446.

[37] M. M. R. Howlader, T. Suga, H. Itoh, T. H. Lee, M. J. Kim, "Role of heating on plasma-activated silicon wafers bonding", *J. Electrochem. Soc.,* 156 (2009) H846.

[38] M. M. R. Howlader, S. Suehara, T. Suga, "Room temperature wafer level glass/glass bonding", *Sens. Actuators A,* 127 (2006) 31.

[39] H. Sugai, I. Ghanashev, M. Nagatsu, "High-density flat plasma production based on surface waves", *Plasma Sources Sci. and Tech.*, 7 (1998) 192.

[40] M. R. R. Howlader, H. Itoh, T. Suga, M. Kim, "Sequential plasma activated process for silicon direct bonding", *ECS Trans.*, 3 (2006) 191.

[41] X. Ma, C. Chen, W. Liu, X. Liu, X. Du, Z. Song, C. Lin, "Study of the Ge wafer surface hydrophilicity after low-temperature plasma activation", *J. Electrochem. Soc.*, 156 (2009) H307.

[42] T. Young, *Phil. Trans. R. Soc. London,* 9 (1805) 255.

[43] Scanning Probe Microscopy Training Notebook from Veeco, 2010.

[44] I. Kanno, M. Yamashita, S. Nomiya and H. Onabe, "Interface resistivity of directly bonded Si wafers", *Jpn. J. Appl. Phys.*, 45 (2006) 7938.

[45] Transmission Electron Microscopy: A Textbook for Materials Science, David B. Williams and C. Barry Carter. New York: Plenum Press, 1996.

[46] M. Baram, W. D. Kaplan, "Quantitative HRTEM analysis of FIB prepared specimens", *J. Micros.*, 232 (2008) 395.

[47] R. F. Egerton, "Electron energy-loss spectroscopy in the TEM", *Rep. Prog. Phys.*, 72 (2009) 016502.

[48] M. G. Kibria, F. Zhang, T. H. Lee, M. J. Kim, M. M. R. Howlader, "Comprehensive investigation of sequential plasma activated Si/Si bonded interface for nano-integration on the wafer scale", *Nanotechnol.*, 21 (2010) 134011.

[49] M. M. R. Howlader, F. Zhang, M. G. Kibria, "Voids nucleation at sequentially plasma activated Silicon/Silicon bonded interface", *J. Micromech. Microeng.*, 20 (2010) 065012.

[50] T. Suga, T. H. Kim, M. M. R. Howlader, "Combined process for wafer direct bonding by means of the surface activation method", *54th Electron. Comp. Tech. Conf.*, 1 (2004) 484.

[51] R. J. Good, "Contact angle, wetting, and adhesion: a critical review", *J. Adhes. Sci. Technol.*, 6 (1992) 1269.

[52] G. J. Wan, R. K. Y. Fu, P. Yang, J. P. Y. Ho, X. Xie, N. Huang, P. K. Chu, "Surface wettabiliy of nitrogen plasma-implanted silicon", *Nucl. Instrum. Methods Phys. Res.* B, 242 (2006) 296.

[53] C. Wang, E. Higurashi, T. Suga, "Void-free room-temperature silicon wafer direct bonding using sequential plasma activation", *Jpn. J. Appl. Phys.*, 47 (2008) 2526.

[54] S. Bengtsson, P. Amirfeiz, "Room temperature wafer bonding of silicon, oxidized silicon, and crystalline quartz", *J. Electron. Mater.*, 29 (2000) 909.

[55] V. Dragoi, G. Mittendorfer, C. Thanner, P. Lindner, "Wafer-level plasma activated bonding: new technology for MEMS fabrication", *Microsyst. Technol.*, 14 (2008) 509.

[56] X. X. Zhang, J-P. Raskin, "Low-temperature wafer bonding: a study of void formation and influence on bonding strength", *J. Microelectromech. Sys.*, 14 (2005) 368.

[57] N. Miki, S. M. Spearing, "Effect of nanoscale surface roughness on the bonding energy of direct-bonded silicon wafers", *J. Appl. Phys.*, 94 (2003) 6800.

[58] A. Sanz-Vealsco, P. Amirfeiz, S. Bengtsson, C. Colinge, Room temperature wafer bonding using oxygen plasma treatment in reactive ion etchers with and without inductively coupled plasma, *J. Electrochem. Soc.*, 150 (2003) G155.

[59] S. V. Aradhya, S. V. Garimella, T. S. Fisher, "Electrothermal bonding of carbon nanotubes to glass", *J. Electrochem. Soc.*, 155 (2008) 161–5.

[60] Y. C. Zhou, Z. H. Zhu, D. Crouse, Y. H. Lo, "Electrical properties of wafer-bonded GaAs/Si heterojunctions", *Appl. Phys. Lett.*, 73 (1998) 2337.

[61] D. Pasquariello, C. Hedlund, K. Hjort, "Oxidation and induced damage in oxygen plasma in-situ wafer bonding", *J. Electrochem. Soc.*, 147 (2000) 2699.

[62] S. Bengtsson, O. Engstrom, "Electrical methods for characterizing directly bonded silicon/silicon interfaces", *Jpn. J. Appl. Phys.*, 30 (1991) 356.

[63] K. S. Henriksen, M. M. V. Taklo, A. Hanneborg, G. U. Jensen, "Oxide charges induced by plasma activation for wafer bonding", *Sens. Actuators A* , 102 (2002) 99.

[64] S. M. Sze, "Physics of semiconductor devices", *2nd Edn, New York: Wiley,* 1981.

[65] M. C. Wagener, R. H. Zhang, G. A. Rozgonyi, M. Seacrist, M. Ries, "Current transport characteristics across shallow hybrid-orientation silicon bonded interfaces", *Appl. Phys. Lett.*, 90 (2007) 112101.

[66] J. Bos, M. Hendriks, "Plasma - induced fixed oxide charge", *J. Appl. Phys.*, 66 (1989) 1244.

[67] S. Bengtsson, O. Engstrom, "Interface charge control of directly bonded silicon structures", *J. Appl. Phys.*, 66 (1989) 1231.

[68] M. Bruel, "Application of hydrogen ion beams to silicon on insulator material technology", *Nucl. Instrum. Methods Phys. Res.*, B 108 (1996) 313.

[69] G. Horn, M. Gabriel, J. Lesniak, T. J. Mackin, "Detection of interfacial gas bubbles in wafer bonded silicon with different surface treatments", *J. Electrochem. Soc.*, 156 (2009) 27.

[70] E. Toyoda, A. Sakai, H. Isogai, T. Senda, K. Izunome, O. Nakatsuka, M. Ogawa, S. Zaima, "Mechanical properties and chemical reactions at the directly bonded Si–Si interface", *Jpn. J. Appl. Phys.*, 48 (2009) 011202.

[71] K. Mitani, U. M. Gosele, "Formation of interface bubbles in bonded silicon wafers: A thermodynamic model", *Appl. Phys.* A, 54 (1992) 543–52.

[72] M. M. R. Howlader, G. Kagami, T. H. Lee, J. G. Wang, M. J. Kim, A. Yamauchi, "Sequential plasma activated bonding mechanism of silicon/silicon wafers", *J. Microelectromech. Syst.*, 99 (2010) 1.

[73] T. Suni, K. Henttinen, I. Suni, J. Makinen, "Effects of plasma activation on hydrophilic bonding of Si and SiO_2", *J. Electrochem. Soc.*, 149 (2002) G348.

[74] K.-Y. Ahn, R. Stengl, T. Y. Tan, U. Gosele, "Stability of interfacial oxide layers during silicon wafer bonding", *J. Appl. Phys.*, 65 (1989) 561.

[75] J. E. Morris, "Nanopackaging, nanotechnology and electronics packaging". *Berlin: Springer*, 2008.

[76] S. Lu, Y. Liu, N. Shao, B. Panchapakesan, "Nanotube micro-opto-mechanical systems", *Nanotechnol.*, 18 (2007) 065501.

[77] Z. Gu, H. Ye, A. Bernfeld, K. J. T. Livi, D. H. Gracias, "Three-dimensional electrically interconnected nanowire networks formed by diffusion bonding", *Langmuir,* 23 (2007) 979.

[78] Z. Gu, H. Ye, D. H. Gracias, D. Gracias, "The bonding of nanowire assemblies using adhesive and solder", *J. Miner. Metals Mater. Soc.*, 57 (2005) 60.

[79] C. Chen, L.Yan, S-W. Kong, Y. Zhang, "Ultrasonic nanowelding of carbon nanotubes to metal electrodes", *Nanotechnol.*, 17 (2006) 2192.

[80] R. D. Johnson, D. F. Bahr, C. D. Richards, R.F. Richards, D. McClain, J. Green, J. Jiao, "Thermocompression bonding of vertically aligned carbon nanotube turfs to metalized substrates", *Nanotechnol.*, 20 (2009) 065703.

[81] J. Han, H.G. Craighead, "Separation of long DNA molecules in a microfabricated entropic trap array", *Science*, 288 (2000) 1026.

[82] V. Senez, E. Lennon, S. Ostrovidov, T. Yamamoto, H. Fujita, Y. Sakai, T. Fujii, "Integrated 3-D silicon electrodes for electrochemical sensing in microfluidic environments: application to single-cell characterization", *IEEE Sens. J.*, 8 (2008) 548.

[83] L. D. Stefano, K. Malecki, A. M. Rossi, L. Rotiroti, F. G. D. Corte, L. Moretti, I. Rendina, "Integrated silicon-glass opto-chemical sensors for lab-on-chip applications", *Sens. Actuators B*, 114 (2006) 625.

[84] D. P. Poenar, C. Iliescu, M. Carp, A. J. Pang, K.J. Leck, "Glass-based microfluidic device fabricated by parylene wafer-to-wafer bonding for impedance spectroscopy", *Sens. Actuators A*, 139 (2007)162.

[85] R. Hull, "Properties of crystalline silicon", *INSPEC, London,* 1999.

[86] C. Iliescu, J. Miao, F. E. H. Tay, "Stress control in masking layers for deep wet micromachining of pyrex glass", *Sens. Actuators. A*, 117 (2005) 286.

[87] O. I. Dosunmu, D. D. Cannon, M. K. Emsley, B. Ghyselen, L. Jifeng, L. C. Kimerling, M. S. Unlu, "Resonant cavity enhanced Ge photodetectors for 1550 nm operation on reflecting Si substrates", *IEEE J Select Top Quan. Electron*, 10 (2004) 694.

[88] L. Colace, V. Sorianello, A. D. Iacovo, D. Fulgoni, L. Nash, G. Assanto, "Germanium-on-glass near-infrared detectors", *Electron Lett.*, 45 (2009) 994.

[89] S. Fama, L. Colace, G. Masini, G. Assanto, "High performance germanium-on-silicon detectors for optical communications", *Appl. Phys. Lett.*, 81 (2002) 586.

[90] L. Colace, P. Ferrara, G. Assanto, D. Fulgoni, L. Nash, "Low dark-current germanium-on-silicon near-infrared detectors", *IEEE Photon Tech Lett.*, 19 (2007)1813.

[91] L. Chen, P. Dong, M. Lipson, "High performance germanium photodetectors integrated on submicron silicon waveguides by low temperature wafer bonding", *Optics Express*, 16 (2008) 11513.

[92] L. Chen, M. Lipson, "Ultra-low capacitance and high speed germanium photodetectors on silicon", *Optics Express*, 17 (2009) 7901.

[93] C.-H. Lin, Y.-T. Chiang, C.-C. Hsu, C.-H. Lee, C.-F. Huang, C.-H. Lai, T.-H. Cheng, C. W. Liu, "Ge-on-glass detectors", *Appl Phys Lett.*, 91 (2007) 041105.

[94] H. Kanbe, M. Miyaji, T. Ito, "Ge/Si heterojunction photodiodes fabricated by low temperature wafer bonding", *Appl. Phys. Exp.*, 1 (2008) 072301.

[95] Y.-L. Chao, Q.-Y. Tong, T.-H. Lee, M. Reiche, R. Scholz, J. C. S. Woo, U. Gosele, "Ammonium hydroxide effect on low-temperature wafer bonding energy enhancement", *Electrochem. Soli-Stat., Lett.*, 8 (2005) G74.

[96] M. M. R. Howlader, M. G. Kibria, F. Zhang, M. J. Kim, "Hybrid plasma bonding for void-free strong bonded interface of Si/Glass at 200°C", *Talanta*, 82 (2010) 508.

[97] M. M. R. Howlader, M. G. Kibria, F. Zhang, "Hybrid plasma bonding of germanium and glass wafers", *Mater. Lett.*, 64 (2010) 1532.

[98] K. M. Knowles, A. T. J. van Helvoort, "Anodic bonding", *Interl. Mater. Revi.,* 51 (2006) 273.

[99] P. Mao, J. Han, "Fabrication and characterization of 20 nm planar nanofluidic channels by glass-glass and glass-silicon bonding", *Lab. Chip*, 5 (2005) 837.

[100] M. Chen, L. Yuan, S. Liu, "Research on low-temperature anodic bonding using induction heating", *Sens. Actuators. A,* 133 (2007) 266.

[101] S. C. Jakeway, A. J. de Mello, E. L. Russell, "Miniaturized total analysis systems for biological analysis", *Fresenius' J. Analy. Chem.*, 366 (2000) 525.

[102] K. B. Mogensen, L. Gangloff, P. Boggild, K. B. K. Teo, W. I. Milne, J. P. Kutter, "Carbon nanotubes integrated in electrically insulated channels for lab-on-a-chip applications", *Nanotechnol.*, 20 (2009) 095503.

[103] C. C. Wong, A. Agarwal, N. Balasubramanian, D. L. Kwong, "Fabrication of self-sealed circular nano/microfluidic channels in glass substrates", *Nanotechnol.*, 18 (2007) 135304.

[104] S.-W. Choi, W.-B. Choi, Y.-H. Lee, B.-K. Ju, M.-Y. Sung, B.-H. Kim, "The analysis of oxygen plasma pretreatment for improving anodic bonding", *J. Electrochem. Soc.,* 149 (2002) G8.

[105] M. R. Howlader, "MEMS/microfluidics packaging without heating", *Proc. SPIE*, 7592 (2010) 75920H.

[106] S. Miyagaki, H. Yamanashi, A. Yamaguchi, I. Nishiyama, "Influence of glass substrate surface roughness on extreme ultraviolet reflectivity of Mo/Si multilayer", *J. Vac. Sci. Technol. B,* 22 (2004) 3063.

[107] A. Datta, S. Gangopadhyaya, H. Temkin, Q. Pu, Shaorong Liu, "Nanofluidic channels by anodic bonding of amorphous silicon to glass to study ion-accumulation and ion-depletion effect", *Talanta*, 68 (2006) 659.

[108] J. Wei, S. M. L. Nai, C. K. S. Wong, Z. Sun, L. C. Lee, "Low temperature glass-to-glass wafer bonding", *IEEE Trans. Adv. Packag.*, 26 (2003) 289.

[109] G. Y. Li, L. Wang, "Influence of bonding parameters on electrostatic force in anodic wafer bonding", *Thin Sol. Film.*, 462–463 (2004) 334.

[110] A. T. J. van Helvoort, K. M. Knowles, J. A. Fernie, "Characterization of cation depletion in pyrex during electrostatic bonding", *J. Electrochem. Soc.*, 150 (2003) G624.

[111] J. C. Rawers, R. A. McCune, A. Adams, "Crystallization of amorphous $Fe_{78}B_{13}Si_9$", *J. Mater Sci Lett*, 7 (1988) 958.

[112] L. Chen, G. Luo, K. Liu, J. Ma, B. Yao, Y. Yan, Y. Wang, "Bonding of glass-based microfluidic chips at low or room-temperature in routine laboratory", *Sens. Actuators. B*, 119 (2006) 335.

[113] H.-S. Min, Y.-C. Joo, O.-S. Song, "Effects of wafer cleaning and annealing on glass/silicon wafer direct bonding", *Trans. ASME. J. Electron. Packag.*, 126 (2004)120.

[114] M. M. R. Howlader, J. G. Wang, M. J. Kim, "Influence of nitrogen microwave radicals on sequential plasma activated bonding", *Mater Lett.*, 64 (2010) 445.

[115] A. T. J. van Helvoort, K. M. Knowles, R. Holmestad, J. A. Fernie, "Anodic oxidation during electrostatic bonding", *Philosoph. Mag.*, 84 (2004) 505.

[116] Q. F. Xing, M. Yoshida, G. Sasaki, "TEM study of the interface of anodic-bonded Si/glass", *Script. Materi.,* 47 (2002) 577.

[117] T. Noma, T. Sugiura, K. Ishii, Y. Ohki, Y. Hama, "Structural stabilization induced by oxygen plasma post-exposure of films deposited from tetraethoxysilane", *J. Phys. D,* 30 (1997) 937.

[118] C. Tudryn, S. Schweizer, R. Hopkins, L. Hobbs, A. J. Garratt-Reed, "Characterization of Si and CVD SiC to glass anodic bonding using TEM and STEM analysis", *J. Electrochem. Soc.,* 152 (2005) E131.